Government of Canada
Fisheries and Oceans

Gouvernement du Canada
Pêches et Océans

MANUSCRIPT REPORT SERIES No. 14

MEASUREMENT AND MODELLING OF FRESHWATER PLUMES UNDER AN ICE COVER

NELSON G. S. FREEMAN

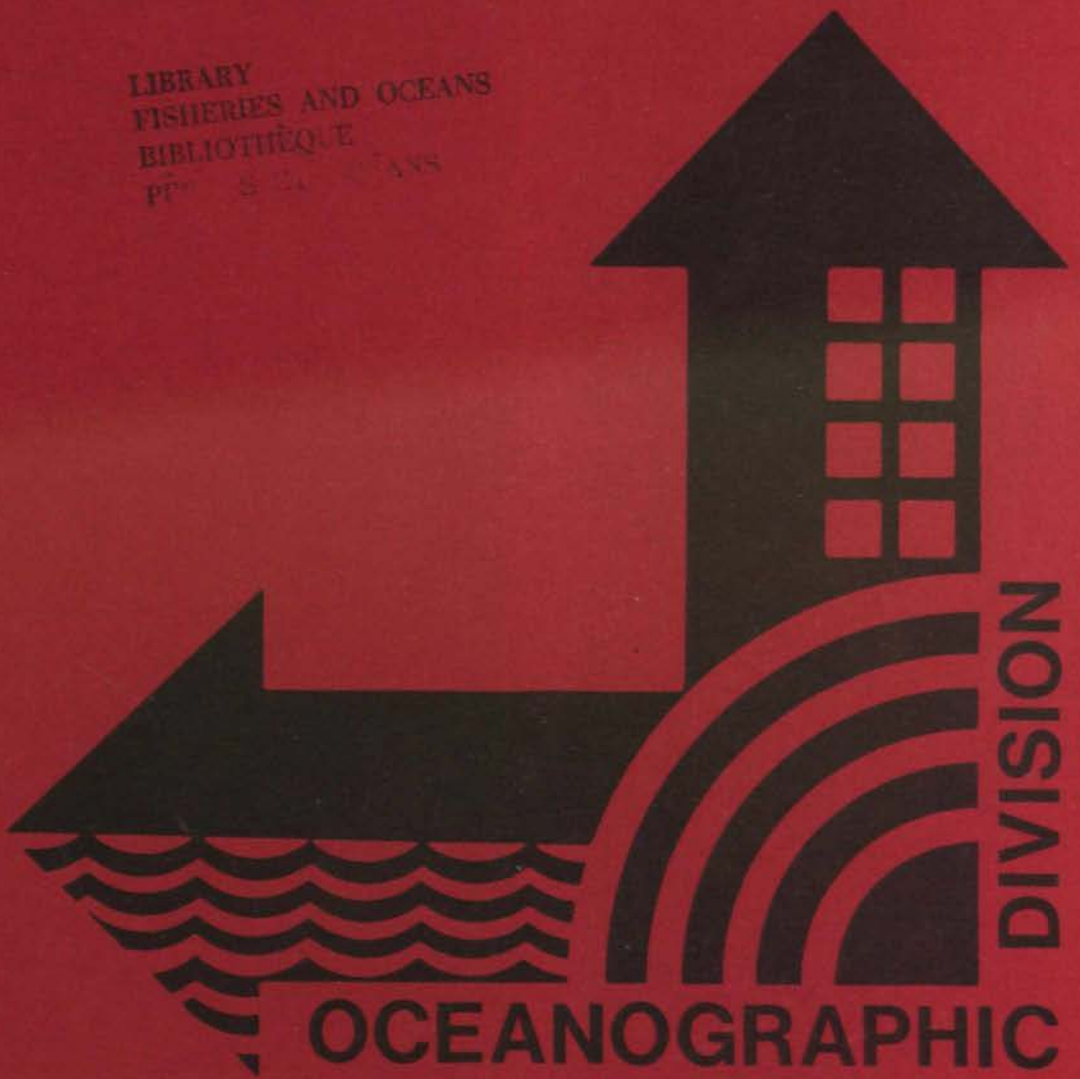

OCEAN SCIENCE AND SURVEYS
BAYFIELD LABORATORY FOR
MARINE SCIENCE AND SURVEYS
BURLINGTON, ONTARIO

MEASUREMENT AND MODELLING OF FRESHWATER PLUMES UNDER AN ICE COVER

by

NELSON G.S. FREEMAN

A thesis
presented to the University of Waterloo
in partial fulfillment of the
requirements for the degree of
Doctor of Philosophy
in
Mechanical Engineering

Waterloo, Ontario, 1982

ABSTRACT

An extensive data base has been obtained on the flow and salt concentration fields for three different under-ice freshwater plumes. An in-depth analysis of this data has provided insight into the role of tidal kientic energy and water column stability on the mixing of fresh and salt water, when the ice cover decouples wind-induced mixing. Four separate data bases (including Peck-1976), each representing different discharge and/or background tidal turbulence levels, enabled mixing relationships to be correlated with estuarine Richardson number. In addition, they provided independent data sets for calibration and validation of models of plume dispersion.

A two-layer numerical model was developed to simulate the flow and motion field of the La Grande River plume under two different discharge conditions. The predicted areal extent, horizontal salinity distributions and flow fields are in good agreement with observations for both the higher (dependent) and lower (independent) discharge simulations. The use of the two-layer model for the testing of different Richardson number dependent mixing relationships will be the next stage of this model development.

ACKNOWLEDGEMENTS

I would like to express my appreciation to my PhD supervisor Dr. George Raithby for his immeasurable encouragement and guidance throughout the course of this undertaking. His talents as a lecturer, researcher and advisor are second to none. I would also like to thank Dr. Maurice Danard for acting as co-supervisor in the early stages of my PhD program.

Part of the work was carried out while I was on educational leave from the federal Department of Fisheries and Oceans. I would like to take this opportunity to acknowledge the financial support of the Department, and the constant support of my work supervisor Mr. Tom McCulloch. I would also like to extend my appreciation to staff of the Oceanographic Division, in particular Dr. Simon Prinsenberg and Mr. Ed Lewis who ably filled in during my absence, Mr. Doug Brooks who oversaw the field program, Mrs. Jean Fiddes for the proofing of the manuscript, and Mr. Bill Haras who helped me to draft the final figures. Ms. Wendy Booth of Prestige Office Services and Mrs. Dianne Crabtree of Dianne's Word Processing Service worked many long hours on the typing of the manuscript.

Last but not least I would like to thank my wife Torchy, and family for their patience and understanding over the five-year period of my PhD studies.

TABLE OF CONTENTS

TABLE OF CONTENTS (Continued)

TABLE OF CONTENTS (Continued)

LIST OF TABLES

LIST OF FIGURES

LIST OF FIGURES (Continued)

LIST OF FIGURES (Continued)

LIST OF FIGURES (Continued)

NOMENCLATURE LIST

A_H	horizontal eddy viscosity coefficient
A_V	vertical eddy viscosity coefficient
$\bar{b}$	mean width of the surface plume
b	plume width for Integral model
b_R	width of plume at river mouth for Integral model
b_S	width of plume at source for Analytical model
C_{h0P} C_{h0W} C_{h0E} C_{h0S} C_{h0N}	five-point operator coefficients for h'_o Poisson equation
C_{U1P} C_{U1E} C_{U1W} C_{U1N} C_{U1S}	five-point operator coefficients for the U1 momentum equation
E	time step multiple
E_y	lateral entrainment coefficient
E_z	vertical entrainment coefficient
EXN_{U1} FXN_{U1}	finite-difference boundary condition coefficients on U_1-velocity
f	Coriolis parameter
F_i	interfacial Froude number
F_P	plume densimetric Froude number
F_1	upper layer densimetric Froude number
g	gravitational acceleration
h	layer depth for Integral model
H	bottom depth for Integral model
h_R	depth of plume at river mouth for Integral model

h_S	depth of plume at river source for Analytical model
h_0	height of free surface above reference level: two-layer model
h_1	height of interface above reference level: two-layer model
h_2	height of bottom above reference level: two-layer model
h_{01}	upper layer thickness: two-layer model
h_{12}	lower layer thickness: two-layer model
h_{02}	total depth of water column
h_0^*	free surface elevation from previous iteration: two-layer model
h_0'	free surface elevation correction from solution of Poisson equation: two-layer model
k_i	ice friction coefficient
k_I	interface friction coefficient
k_b	bottom friction coefficient
k_S	salt diffusion coefficient at the interface
K_e	entrainment coefficient
K_H	horizontal eddy diffusivity coefficient for salt
K_V	vertical eddy diffusivity coefficient for salt
L,H	horizontal and vertical length scales
P_a	atmospheric pressure
P_1	pressure in upper layer: two-layer model
P_2	pressure in lower layer: two-layer model
P^*	nondimensionalized pressure variable
P	pressure variable
Q_0	river discharge
Ri_E	estuarine Richardson Number
Ri_f	flux Richardson Number
Ri_g	gradient Richardson Number

Ri^*	interfacial Richardson Number
s	salinity
S_1	vertically-averaged salinity in upper layer
S_2	vertically-averaged salinity in lower layer
SUBSCRIPTS	
P,W,E,S,N NE,EE	used to denote location of variables in deriving finite-difference operators (see Fig. 25)
$S^{.M}_{U1P}$	free surface gradient and Coriolis source term in U_1 momentum equation
$S^{.L}_{U1P}$	density gradient & friction source term in U_1 momentum equation
$\dot{S}_{hOP}$	mass conservation source term for Poisson equation
t	time coordinate
T	tidal period (12.42 hour for M_2 constituent)
u	horizontal velocity component (positive northward): Two-layer model
v	horizontal velocity component (positive westward): two-layer model
w	vertical velocity component (positive upward): two-layer model
$u_1 \rightarrow u$; $u_2 \rightarrow v$; $u_3 \rightarrow w$	
u*,v*,w*	nondimensionalized velocity components
u**	local friction velocity
U,W	horizontal and vertical velocity scales
U_R	river velocity for Integral model
U_S	uniform flow field for Analytical model
U_{MEAN}	tidally-averaged mean value of eastward component of current from 25-hour station data
U_{TIDE}	tidal amplitude of eastward component of current from 25-hour station data

V_{MEAN} tidally-averaged mean value of northward component of current from 25-hour station data

V_{TIDE} tidal amplitude of northward component of current from 25-hour station data

U_1 vertically-averaged u velocity in upper layer

U_2 vertically-averaged u velocity in lower layer

U_{1P} x-directed mass conserved velocity in upper layer

U_{1P}^* x-directed velocity computed from U_1-momentum equation

V_1 vertically-averaged v velocity in upper layer

V_2 vertically-averaged v velocity in lower layer

V_{1P} y-directed mass conserved velocity in upper layer

V_{1P}^* y-directed velocity computed from V_1 momentum equation

x horizontal coordinate (positive northward): two-layer model

y horizontal coordinate (positive westward): two-layer model

z vertical coordinate (positive upward): two-layer model

$x_1 \rightarrow x$; $x_2 \rightarrow y$; $x_3 \rightarrow z$

x*, y*, z* nondimensional coordinates

α	relaxation parameter
α_i	linearized ice friction coefficient (cm sec^{-1})
α_I	linearized interface friction coefficient (cm sec^{-1})
α_b	linearized bottom friction coefficient (cm sec^{-1})
β	weighting coefficient on finite-difference representation of advection terms.
γ	exponent on interfacial Richardson number in entrainment velocity representation.
ϵ_{ijk}	third order isotropic Cartesian tensor
$\Delta\rho$	top-to-bottom density difference and in the two-layer model represents $(\rho_2-\rho_1)$.
δ_{i3}	second-order isotropic Cartesian tensor
δx	x-directed grid interval in finite-difference scheme
δy	y-directed grid interval in finite-difference scheme
η	free surface elevation
κ	linearized vertical diffusion coefficient
ν	kinematic viscosity
ρ_∞	bottom density in the far-field
ρ_1	vertically-averaged density of upper layer
ρ_2	vertically-averaged density of lower layer
τ_{xb}	lateral shear stress in Integral model
τ_{xz}	layer shear stress for Integral model
υ_{12}	the relative root-mean-square current speed between the upper and lower layer
υ_1	the upper layer root-mean-square current speed
υ_2	the lower layer root-mean-square current speed
ϕ	represents the total variable
$\bar{\phi}$	represents the long-term mean

$\tilde{\phi}$	represents the tidal amplitude
ϕ'	represents the turbulent component
ω_{01}	entrainment velocity across free surface: positive upwards
ω_{12}	entrainment velocity across interface between upper and lower layer: positive upwards
ω_{12}^{+}	equals ω_{12} if sign of ω_{12} is positive, otherwise zero.
ω_{12}^{-}	equals ω_{12} if sign of ω_{12} is negative, otherwise zero.

1. INTRODUCTION

1.1 BACKGROUND OF THE PROBLEM

1.1.1 Historical Overview

The historical interest in the oceanography of Hudson Bay and James Bay has been related principally to the development of its natural resources. In order to assess the viability of a commercial marine fishery in this sub-arctic region, expeditions in the mid-thirties and more recently in the mid-fifties to early sixties provided the first comprehensive data on the summer circulation and distribution of physical and biological parameters. However, the conclusions of the fisheries scientists that, "low productivity due to low temperatures, apparent lack of complete and regular mixing of surface and bottom waters, long periods of ice cover, inhibited light supply, and short growing season" did little to encourage further oceanographic study of this area. Hudson Bay, with an estimated secondary productivity of 100 mg m^{-3}, appears more biologically similar to the Arctic Basin (<25 mg m^{-3}) than the North Atlantic (500 mg m^{-3}) - Hunter (1965).

Motivated by commercial interest in the possibility of oil deposits in the Paleozoic sediments that lie under the waters of Hudson Bay, a major oceanographic and geophysical survey was undertaken in 1965. The new oceanographic research vessel CSS Hudson, the support ship M/V Theron, launches, a helicopter and fixed-wing aircraft carried out a massive sampling of some 800 stations over most of Hudson Bay. From this expedition our first real knowledge of the marine geology, palaeontology, bathymetry, sedimentology, geomagnetism and gravity of the Bay was acquired.

However, it was not until the Quebec government's decision in the early seventies to dam a number of the rivers flowing into Hudson Bay and James Bay for the purpose of hydro-electric development that the most comprehensive physical and biological studies were carried out. It was also during this period that the first winter (February, March, April) oceanographic measurements of James Bay, some of which will be

reported in this dissertation, were made. Complex La Grande, the first of a number of such developments (see Fig. 1), provided the unique opportunity to study the pre- and post-project effects of spatial and seasonal changes in freshwater discharge on the marine environment. The most significant alteration in river runoff has taken place in the winter when an order of magnitude increase in the natural winter flow will substantially alter the under-ice water column stability over a large section of north-eastern James Bay. It is the measurement and modelling of this freshwater plume under an ice-cover that forms the basis of this research dissertation.

Unfortunately, with the termination of the James Bay Environmental Agreement and the settling of Inuit and Cree native claims in the mid-seventies, the support for oceanographic research on Hudson/James Bay is waning. Perhaps the recent announcement by the Ontario government, to re-establish offshore drilling for oil and natural gas in Hudson Bay, will provide a new stimulus for the history of development-led research on this unique sub-arctic system. Wouldn't it be far-sighted if oceanographic research could be carried out in this area not only in response to development pressures but as a prototype of less well-bounded and well-understood Arctic systems?

1.1.2 Changes Related to Hydroelectric Developments

The La Grande Complex, when it is fully on stream in the mid-eighties, will generate 10,000 megawatts of hydroelectric power. Data on the four power generating stations that make up the complex are given in Table I. By far the largest installed capacity is that of LG-2 which began partial operation in November, 1979.

TABLE I - LA GRANDE COMPLEX

POWER STATIONS	LG-1	LG-2	LG-3	LG-4
INSTALLED CAPACITIES (megawatts)	910.	5,328.	1,920.	2,032.
DISTANCE FROM RIVER MOUTH (km)	71.	117.	238.	463.
GROSS HEADS (m)	23.5	141.7	76.2	119.5
RESERVOIR CAPACITY (km^2)	20.7	2,834.8	2,459.4	750.8

The La Grande River watershed, which formerly covered an area of 98,000 km^2 will be increased to 177,000 km^2 through the diversion of 87% of the Eastmain and Opinaca Rivers flowing into James Bay and the diversion of 28% of the Koksoak River flowing into Ungava Bay. The need to maintain a relatively uniform head and regulated water flow necessitated the creation of six immense reservoirs with a total area of 11,558 km^2, representing 7% of the post-project La Grande watershed.

As a result of the river diversions the mean annual discharge of the La Grande River will increase from 1,865 m^3 sec^{-1} to approximately 3,400 m^3 sec^{-1} (Fig. 2a), an increase of 91% (Peck, 1976). If it is assumed that the post-project flow for the La Grande River is kept constant at this elevated mean annual discharge, the greatest change in river flow will occur in the winter months, when more than a 500% increase will take place between January and April. If, as is likely to happen, the power demand in the winter becomes substantially greater than at other times in the year, then the winter outflow will be of the order of 4,260 m^3 sec^{-1}. Further, if approval is received for increased installed capacities at LG-2 and LG-1 then the La Grande River discharge might conceivably peak at 6,456 m^3 sec^{-1} for about 75 days in the winter (Peck, personal communication). These two winter conditions would then subject the marine system off La Grande to above-natural freshwater inputs of between 700% to 1,100%, during a time when a close-packed to solid ice-cover largely eliminates wind-induced mixing of the water column. The Eastmain estuary will experience the opposite effect as the river discharge in winter will be reduced to a mere 28 m^3 sec^{-1}.

The effect of this regulated discharge on the freshwater input rates to James Bay as a whole, however, will be somewhat less severe than in the immediate vicinity of the La Grande and Eastmain Rivers. As can be seen in Fig. 2b, (which has been modified from Prinsenberg (1980) to include only the La Grande Complex effect) a constant discharge of 3,400 m^3 sec^{-1} will represent a net gain of about 100% in freshwater input in the winter months and a net loss of about 10% during the spring freshette. The winter freshwater input would be augmented by a further

100% if the predicted maximum power demand is realized; however, the freshwater input for the remainder of the year would undergo a corresponding decrease as no increased reservoir capacity is planned to satisfy this additional use of stored capacity. Thus the largest increase in freshwater addition to James Bay, as a whole, will also occur during the ice-covered winter months.

Complex La Grande is not the only hydroelectric development, operating or proposed, for the Hudson and James Bay watershed. Prinsenberg (1980) has estimated the magnitudes of man-made changes in freshwater input rates resulting from the following developments: 1) Nelson-Churchill River Project (Hudson Bay); 2) La Grande Complex (James Bay); 3) Nottaway-Broadback-Rupert Project (James Bay); 4) Great Whale-Little Whale Project (Hudson Bay). In conclusion, he found that a conservative estimate of the net effect of all the projects would be to increase the average winter runoff rate to the Hudson/James system by 52%, due largely to the La Grande Complex, while decreasing the summer runoff rate by only 6%. Thus it can be expected that the cumulative effects on the marine environment of the combined hydro electric developments in Quebec, Manitoba and Ontario will be most significant during the winter months.

1.1.3 Effects of Freshwater Runoff Regulation

W.H. Sutcliffe Jr. (1972) was the first to show that a direct correlation existed between increase in St. Lawrence River discharge and halibut, haddock, lobster and clam catch statistics for the Gulf of St. Lawrence. Based upon classical density-driven estuarine circulation theory, he linked changes in freshwater runoff to the vertical recirculation of regenerated materials. Hans Neu (1976) found a direct correlation between seasonal variations in freshwater discharge from the St. Lawrence River and surface salinity values as far away as Cabot Strait on the Gulf of St. Lawrence.

Although not addressed directly in this study, the most immediate effect of the freshwater regulation brought about by the La Grande

Complex will be in those river estuaries for which the flow is substantially reduced. The Eastmain River discharge will be decreased permanently by almost 90%. The La Grande River flow was cut off temporarily from the 28th of November, 1978 until June 20, 1979 in order to fill the LG-2 reservoir. In the latter case, observations were made on behalf of the Societé d'Energie de Baie James of the pre- and post-cut-off conditions in the river estuary (Dominique Roy - personal communication). Prior to cut-off, the underlying saltwater seldom intruded into the La Grande River estuary even under the low winter discharges of 450 m^3 sec^{-1}. When the flow was cut off however, a brackish water gradient developed in the river, with depth-averaged salinities stabilizing at 20°/oo at mile 2.4 (3.8 km), 8 to 9°/oo at mile 12 (19.2 km), and <1°/oo at mile 17 (27.2 km) close to the first rapids. The freshwater fish moved upstream to the lower salinity water; however, catch per unit effort for all species declined by upwards of 70%. Thus a dramatic but relatively predictable change occurred in the ecology of the La Grande River estuary.

Less predictable, however, is the effect of altered freshwater discharge on the coastal environment of James Bay and on the water mass coupling of James Bay with Hudson Bay. Barber (1967) pointed out that strong tidal mixing in Hudson Strait diluted the inflowing relatively warm and saline Atlantic water with less saline outflowing Hudson Bay water. This recycling of Hudson Bay water thus tends to decouple the Hudson/James Bay system from the North Atlantic, and limits the probable effect of freshwater regulation no further downstream than the western entrance to Hudson Strait. Barber et al. (1972), suggested that the coupling between James and Hudson Bays, on the other hand, would be affected by changes in runoff, particularly because of the breadth of the connection and the greater vertical stratification of the water column.

Prinsenberg (1978), by applying the similarity solutions developed by Hansen and Rattray (1965) for estuarine circulation, found that during the fall and winter both diffusion and advection are important

contributions to the salt flux in James Bay. Prinsenberg also determined that the direct contribution of river flow (river-discharge mode) was small ($U_f = 2.35 \times 10^{-2}$ cm sec) in James Bay. Thus when the winter discharge was doubled, simulating a post-project discharge, both the outflowing surface and inflowing bottom velocities at the entrance to James Bay were similarly increased, due almost exclusively to a doubling of gravitational-convection mode.

The possible biological consequences of regulated freshwater discharge in James Bay have not been investigated in great detail. To a large extent, changes in biology depend on the alterations to the physical processes of circulation and mixing. Grainger and McSween (1976) found that James Bay supports a diverse euryhaline fauna which appears to be isolated from the more saline waters of Hudson Bay and to be fully dependent upon the persistence of a large brackish-water estuary. The authors conclude that the proposed increase in freshwater discharge will likely augment the range of the brackish-and-freshwater populations of zooplankton but not permanently affect their ability to survive. However, the three-to four-fold increase in the areal extent of the surface plume could trap a large portion of strictly freshwater organisms in a more brackish surface layer once ice breakup facilitates wind-induced mixing.

Grainger and McSween (1976) also concluded that the La Grande River contributes very little to the nitrate and phosphate levels in James Bay and this is likely to be unaffected by freshwater regulation. Freeman, et al. (1981), confirmed the low riverine source of nutrients in the winter time, but showed that, in a region seaward of the stabilizing surface plume, intense vertical mixing substantially increased the concentration of nutrients in the upper water column. This upwelling brought them into contact with the underside of the ice where an ice flora community was well-developed as early as mid-February. Therefore, an increase in freshwater discharge in the winter could result in less recycling of nutrients over a large portion of northeastern James Bay and a corresponding reduction in the spring phytoplankton bloom in

this area. However, the extent of the change depends on how significantly mixing and entrainment in the coastal waters of James Bay are affected by altered freshwater discharge.

Recently the Department of Fisheries and Oceans set up a Task Force to study the effect of freshwater runoff on the marine environment, using the Gulf of St. Lawrence as the case study, Budgen, et al. (1981). One of their principal recommendations was that, "The nature of the relationship between runoff and entrainment in various areas of the Gulf should be investigated and that a modelling approach aimed at evaluating the relative importance of the factors controlling vertical transport of salt and nutrients be adopted."

1.1.4 Scientific Opportunities

The measurement and modelling of the La Grande River winter plume provides some unique scientific opportunities not obtainable under open water conditions. The winter ice cover eliminates wind-induced mixing, thus enabling the study of mixing from tidally-generated turbulence only. It also removes the non-synoptic effect of wind mixing on the parameter fields. The shore-fast ice provides a stable platform from which to take field observations. It also appears to inhibit tidal movements of the plume, thus permitting sampling of water mass characteristics to take place over weeks instead of hours. The only additional complication posed by the ice cover is the need to determine an ice-water friction coefficient.

The gradual implementation of regulated river flow on the La Grande River enabled measurements to be made for three distinctly different discharge rates, and thus the effect of flow rate to be examined. Some insight was also possible on the competing roles of tidal energy and stratification in enhancing or limiting the mixing and entrainment of brackish water in the vertical.

The results of the La Grande River winter plume measurements and modelling could be applied to the study of other river plumes in the Arctic - such as the Mackenzie River outflow in winter. In a somewhat

more speculative application of the work, the question raised by Barber (1977), that this type of freshwater layer may have been responsible for the dispersion of certain freshwater species in the Arctic sometime during the most recent period of glaciation, could be examined.

1.1.5 Scope of the Present Research

In order to assess the principal effects of freshwater regulation brought about by the La Grande Complex a two-phase research program was undertaken. The first consisted of two years of field measurements to obtain a better understanding of momentum and mass transfer in freshwater plumes beneath an ice cover; during this time three different discharge conditions were observed. The second phase was devoted to the development of a two-layer numerical model which can be used to predict the future extent of the surface plume and its effect upon circulation.

Field measurements of such under-ice plumes by previous workers (Peck 1976, Prinsenberg 1978, Ingram 1981) were largely limited to the delineation of their vertical and lateral structure. In order to study the plume dynamics an unmanned current-conductivity-temperature-depth profiling system was developed. This system permitted measurements to be taken at up to sixteen depths for two or more semi-diurnal tidal cycles. In-line vane Aanderaa current meters rigidly suspended from the surface of the shore-fast ice permitted the temporal and spatial distributions of flow properties to be measured. Continuous conductivity and temperature profiles over depth, measured with a Guildline Mark IV CTD probe on a 6 km grid spacing, furnished detailed information on the lateral and vertical structure of the plume.

This field program was undertaken in the winters of 1979 and 1980. During January 1979, a small survey was conducted off the La Grande River to observe changes in salinity during filling of the LG-2 reservoir and to establish background salinity and cross-flow conditions in the absence of a river discharge. In February of the same year, the survey was moved to the Great Whale River estuary where five current profiling stations provided information for a first look at plume

dynamics. In February and March 1980, a two-month observational program, which included sampling for nutrient and seston concentration distributions, produced fairly detailed information on mixing parameters and nutrient upwelling at the leading edge of the plume. These data sets were also used to compare with computations from the numerical model.

In the second phase, a steady-state two-layer numerical model was developed to simulate plume dispersion and to study various entrainment models. The equations were written in a vertically integrated form, such that more realistic parameter profiles as given by Hansen and Rattray (1965) or Rattray (1967) could be introduced at a later date. The model employs a velocity-pressure coupling through the solution of a Poisson equation, and which is unique to geophysical problems. Both vertical entrainment and diffusion are tested in the model and the sensitivity of the solution to various friction formulations is investigated. Calibration of the model is carried out using the extensive data base collected off La Grande in 1980 and verification is made on the 1976 La Grande lower discharge data.

1.2 BACKGROUND OCEANOGRAPHY OF THE HUDSON BAY SYSTEM

Hudson Bay is the largest semi-enclosed body of water in Canada, measuring some 900 km on each side, yet it is as shallow as most of the Great Lakes; its deepest sounding is approximately 260 m. It is located 1,700 km north of Toronto, and is accessible by sea through Hudson Strait for only three months of the year. The Bay is a coastal plain estuary with surface salinity varying in summer from 23°/oo near shore to 30°/oo offshore, and bottom salinity decreasing only slightly from 33°/oo at the deep oceanic inflow of Hudson Strait to 32°/oo at the mouth of James Bay. The long-term circulation and thus distribution of such parameters as salinity, temperature, dissolved oxygen, phytoplankton and nutrients is regulated by the freshwater inflow from the forty-two rivers emptying into Hudson Bay and James Bay. The Hudson Bay watershed drains one-third of the surface area of continental Canada,

and discharges three times the amount of freshwater of either the Mackenzie or St. Lawrence Rivers. The general circulation in this system is anti-clockwise, with the earth's rotation setting up more intense flows along the coasts. Surface plumes of brackish water (26 to 28°/oo) are observable off the mouths of most of the major river estuaries, for example off Chesterfield Inlet (Fig. 1), and are advected along by the mean anti-clockwise current.

1.2.1 Circulation in James Bay

James Bay is only one-twentieth the size of Hudson Bay, but contributes 45% of the yearly averaged runoff to the total system, and is thus fresher than Hudson Bay. The rivers on the Quebec side contribute about 50% more water than those on the Ontario side, and because of the general anti-clockwise circulation in the Bay the east side is much fresher than the west. In the winter the Bay is nearly homogeneous from top to bottom except in the vicinity of the plumes, where vertical gradients of 20°/oo can occur over two metres depth. In summer a seasonal stratification exists at approximately 20 to 25 m depth, with top to bottom salinity differences of 2 to 6°/oo. As is characteristic of a coastal plain estuary, density is principally determined by salinity, not temperature. Because of an order of magnitude decrease in river inflow from summer to winter, the average salinity of James Bay rises about 2 to 3°/oo in the winter.

The 1975-76 bay-wide salinity data given in Peck (1976) permit an indirect examination of the winter circulation in James Bay. Very little vertical stratification exists, except in the vicinity of the river plumes. The greatest salinity gradient is from east to west, indicating that the more saline Hudson Bay water is entering on the west side of the bay over the entire water column, and the fresher James Bay water is exiting along the east coast in the upper layer. The salinity data also shows that to the south of the La Grande estuary there is no evidence of the Eastmain River plume.

El Sabh et al. (1977) computed geostrophic currents for the summer, using the condition of zero salt flux across the entrance to James Bay. They found that a narrow coastal current, with surface velocities on the order of 15 cm sec^{-1} out of the Bay, is balanced by a broad, deep, and much slower inflow, with velocities less than 5 cm sec^{-1}. A similar geostrophic calculation was not made for winter conditions, since the presence of an ice layer added a further frictional boundary layer, thus precluding the usefulness of inviscid geostrophic balances. Prinsenberg (1978), using Hansen and Rattray's similarity theory for a one-dimensional partially-mixed estuary, computed cross-sectionally averaged outflow currents of 1 to 2 cm sec^{-1} in the winter. Current meter data collected in the winter of 1980 (Table II) indicate that monthly mean flows were generally to the northwest with speeds ranging from 2 to 5 cm sec^{-1}.

1.2.2 River Plumes

Brackish water plumes are observed off the La Grande and Eastmain River mouths, both in the summer and the winter. The plumes remain coherent up to 70 km from their source and obtain widths of 20 to 30 km. The existence of an ice cover approximately between November 15 to June 15 (seven months) inhibits wind-induced mixing. This allows the plumes in winter to spread out further than under ice-free conditions before mixing with the underlying salt water. Even though the winter discharge is an order of magnitude less than in the summer, the plumes in March (Fig. 1) appear to have twice the surface area of the summer plumes, due principally to the decoupling of wind-induced turbulence by the ice cover. Both in the summer and the winter the plumes diffuse laterally and vertically relative to the ambient fluid, thus providing the density gradients to drive the gravitational circulation in the Bay.

1.2.3 The Tides of Hudson Bay-James Bay

The principal tidal component in Hudson Bay is the semi-diurnal constituent (12.42 hrs), forced at the entrance by the incoming Atlantic

tide. The M_2 tide progresses from Hudson Strait and propagates as a Kelvin wave in an anti-clockwise direction around Hudson Bay. It dips down into James Bay and proceeds north along the east coast of Hudson Bay, joining the incoming tide near the mouth. It rotates about two major amphidromic points located in east and central Hudson Bay, and which are connected by a nodal line of zero amplitude. Maximum 'M_2' tidal amplitudes of 150 cm are observed on the west coast with amplitudes decreasing to 10 cm near the degenerate node just south of the La Grande River in northeastern James Bay. The diurnal and other harmonics are more than an order of magnitude smaller than the M_2. Tidal currents as computed from a two-dimensional numerical model (Freeman et al. 1976) range from 110 cm sec^{-1} at the Hudson Strait entrance to a few cm sec^{-1} just south of the Belcher Islands. Tidal currents measured in the summer (Prinsenberg, 1978) in northeastern James Bay range from 15 to 30 cm sec^{-1}, while in winter (Table II) they are less, ranging from 4 to 20 cm sec^{-1}.

1.3 PREVIOUS WORK ON RIVER PLUMES

The modelling of buoyant plumes resulting from freshwater spreading out over salt water has received only a limited treatment in the literature, while there exists a considerable body of knowledge on thermal plumes discharging from nuclear power plants. Dunn et al. (1975) from the Argonne National Laboratory and Jirka et al. (1975) from the Ralph M. Parsons Laboratory, M.I.T., present extensive evaluations of the thermal plume modelling efforts to mid-1975. While the latter report concentrates on the integral model approach, which as it turns out has more direct application to freshwater plumes, the Argonne study is comprehensive and appears to be more objective.

An extensive literature also exists on the modelling of circulation and mixing in river estuaries where the lateral dimension, while not necessarily constant, is at least known a priori. Bowden (1967) provides an overview of the roles of mixing versus entrainment in the full spectrum of estuarine types, while more recent work of

Fischer (1976) compares both field and laboratory observations of mixing and dispersion in partially stratified and well-mixed estuaries. Of more direct application to the present work is Robert Long's 1975 study of circulation and density distribution in a deep, strongly stratified, two-layer estuary. The principal differences are that in the present study, the turbulence generation takes place in the lower layer due to tidal action (rather than in the upper layer as a result of wind mixing), and the width of the upper layer is determined by the spreading dynamics (rather than by the width of the estuary).

1.3.1 Field Measurements of River Plumes

Probably the most comprehensive set of measurements of the density and flow fields in and below river plumes are those of Garvine (1974a and 1977) and Garvine and Monk (1974) in the Connecticut River plume. Through the extensive use of drogues, Garvine was able to show that a pronounced cross-stream surface flow existed, that moved water from the plume axis to a frontal region where strong surface convergence was observed. Despite large vertical velocity shears across the plume, the flow within the plume appeared stable and the motion of the ambient water did little to influence the motion of the plume water. Wright and Coleman (1971) studied the effluent expansion and interfacial mixing in the presence of a salt wedge in the Mississippi River delta, and concluded that flow deceleration and effluent deconcentration are primarily the result of vertical rather than lateral mixing.

Stronach (1977) also used salinity and drogue measurements, and established that the brackish water plume from the Fraser River becomes saltier and thinner as one proceeds away from the river mouth. River momentum decreases in this direction and within 6 to 8 km the plume acquires the velocity of the tidal flows. The pycnocline is less sharply defined than in the La Grande winter plume, with the bottom of the plume undergoing extensive mixing with the deeper Strait of Georgia water. An added complication to the synoptic measurement of the Fraser River plume dynamics is the tidal modulation of the river flow; on each

ebbing tide bursts of fresh water advance into and are incorporated in the existing plume. In addition, tidal flows in the Strait change the location of the plume axis by as much as 10 km every tidal cycle. No comprehensive estimates of mixing or entrainment into the plume are made from the data set, however.

Previous observations on river plumes in James Bay and Hudson Bay delineate only the lateral and vertical extent of the salinity structure, with little data on the plume dynamics. Peck (1976) provided the first data on the under-ice salinity distribution in James Bay and observed that there was a "Horizontal increase of fresh water spread from the Eastmain and La Grande Rivers due to the absence of wind mixing under the solid ice cover." Ingram (1981) presented observations of the motion field and dilution effects of the Great Whale River plume in both summer and winter. While the winter observations in the spring of 1977 and 1978 consisted of only three salinity profiles and one current meter mooring, Ingram was able to conclude that the winter plume was much thicker and larger in areal extent than the summer plume, in spite of the reduced freshwater inflow in winter. An attempt was made to estimate entrainment rates into the plume both for summer (6×10^{-3}) and winter (10^{-3}); but, these rates are unrealistically high compared to those calculated by Cordes et al. (1980) for the Fraser River plume.

1.3.2 Modelling of River Plumes

In a series of three papers in the Journal of the Oceanographic Society of Japan, Takano (1954a, 1954b, 1955) presented an analytical model of the spreading of a river plume discharging into an unbounded ocean. Basically it represented a balance of Coriolis force, hydrostatic pressure gradient and horizontal eddy viscosity, neglecting completely vertical shearing stresses. When Bowman (1978) applied this model to the spreading and mixing of the Hudson River plume, a horizontal eddy viscosity coefficient (10^{8} cm^{2} sec^{-1}) two orders of magnitude larger than normal oceanic values was required to correlate the prediction of the model with observations.

Garvine (1974b) developed an integral model of the small scale ocean fronts, and more recently extended it to large scale ocean fronts where the Coriolis force becomes important (Garvine 1979a and 1979b). Garvine showed that, for a steady state to exist, interfacial friction and/or upward mass entrainment is required to balance the net pressure gradient produced by the sloping sea surface and frontal interface in the light water pool. Another contribution was the delineation of a two-layer circulation within the plume, which for downward entrainment drives a strong surface convergence toward the front. The principal limitation of the model, as applied to the river plume dispersion, is the need to supply the horizontal density field, a priori, and the lack of prediction of the size of the parent pool under different discharge conditions. Kao et al. (1977) developed a horizontally averaged model of buoyant surface discharge into an ambient body of water. Using a Richardson number dependent turbulence model based on the Munk and Anderson (1948) eddy viscosity model, the numerical model predicts a surface density current with strong surface convergence and downwelling near the front. However, the lack of horizontal spreading precludes its direct application to the under-ice river plume dispersion.

More directly applicable is the thin upper layer numerical model developed by Stronach (1977) for the Fraser River plume. The concept of depletion (downward or negative entrainment) was first introduced and the use of a zero gradient in outflow Froude number flux ($\partial^2 F^2/\partial n^2=0$) facilitated the handling of open outflow boundaries in a non-linear flow. Drogue tracks predicted by the model compared quite favorably with observed drogue movements in the Fraser River plume. However, this upper layer model has some limitations that make it unsuitable for application to the La Grande winter plume. The model solves the time-dependent equations out to steady-state or quasi-steady state (tidal variations only) and this requires thousands of time steps (small time steps are required to ensure computational stability). Depletion is introduced without either a physical derivation or an attempt at field measurement. Surfacing isopycnals, a requirement for adequately

treating frontal dynamics, is not handled by the present model. Finally, the lack of a lower layer model prevents the investigation of the effects of the surface plume on the underlying circulation.

Some three-dimensional models of river plumes have been reported in the literature. Paul and Lick (1973 and 1974) introduced a rigid lid condition that eliminates the need to calculate the free surface elevation, and thus the generation of free-surface gravity waves. This apparently reduces the computational time to reach steady state by two orders of magnitude (see also Simons 1980); however, the surface pressure had to be computed by solving a rather lengthy Poisson equation, derived by vertically integrating the 'u' and 'v' momentum equations and taking the horizontal divergence of these two equations. In the second paper Paul introduced a modified vertical coordinate to account for topographic effects, much the same way as the sigma equations approach to Great Lakes hydrodynamics of Freeman et al. (1972). There was no provision in either of these models for including density effects on mixing. As is common in three-dimensional time-dependent models, only a few comparisons with field data were possible because of the cost of the lengthy computer runs to steady-state (e.g., three hours CPU time for the Point Beach comparisons); there was also a dearth of synoptic data. Unrealistically large values of diffusion coefficients used in the model produced abnormally rapid spreading rates.

The only three-dimensional numerical model to be applied to the freshwater outflow problem - the South Pass of the Mississippi River - was developed by Waldrop and Farmer (1974). The generalized conservation equations of momentum, energy, and salt were solved explicitly while the continuity equation was used to back out vertical velocity. One unique feature was the incorporation of a coordinate stretching transformation, which permitted finer grid resolution in the near-field and a coarser grid in the far-field. Since there was no provision for the inclusion of density effects on mixing, the axial decay of temperature, amongst other things, was poorly predicted.

1.3.3 Conclusions Based on the Literature Review

From a review of the literature it is concluded that, on the experimental side, there is a lack of synoptic velocity and density data and mixing relationships that correlate with Richardson number effects. On the modelling side, the vertically two-dimensional models do not provide information on lateral plume dispersion, while the time-dependent three-dimensional models require extensive computer runs to reach steady-state for comparison with actual plume observations. Thus it appears that the most economical and physically quantifiable approach to modelling of fresh water plumes under an ice cover is to develop a two-layer numerical model which is closely tied to observations of the plume under different discharge and tidal conditions; this represents the approach taken in this dissertation.

1.4 THESIS OUTLINE

The preceding parts of Chapter 1 provide background information on the changes in river discharge brought about by the La Grande Complex, potential effects of regulated river flow on the marine environment, some unique scientific opportunities of the La Grande River plume study, and the scope of the present research. The general circulation and tidal propagation in Hudson and James Bay are reviewed for both the open water and ice-covered period and some basic characteristics of the La Grande river plumes in summer and winter are presented. Previous measurements and modelling efforts on river plumes are reviewed and the conclusion reached that synoptic measurements of mixing correlated with a bulk Richardson number are required. It was also concluded that a two-layer numerical model would permit the greatest economy and flexibility in the investigation and prediction of freshwater dispersion under an ice-cover.

In Chapter 2 the results of field measurement programs in the winters of 1979 and 1980 are discussed. The along plume and cross plume distributions of salinity, temperature, nutrients, and seston are plotted. Distributions of tidal and mean kinetic energy are also plotted

and correlated by use of interfacial Froude number with vertical mixing of salt and nutrients in the water column. Comparisons are made based on three different river plumes, each with differing discharge and background tidal conditions. Finally, it is shown that plume mixing correlates with estuarine Richardson number.

Modelling considerations are addressed in Chapter 3. First, a scale analysis of the governing equations for the near and far-field is performed, then the role of tidally-generated turbulence as it affects the Richarson number is investigated. A detailed analysis of entrainment versus diffusion is presented and formulations of each are derived for later incorporation into the numerical model. A far-field integral model is then derived and the factors controlling interface slope examined. An advection-diffusion model is also formulated to obtain estimates of the horizontal salt diffusion coefficients and to examine the Munk-Anderson model for vertical diffusion.

In Chapter 4 the continuity, momentum and salt balance equations are integrated vertically over the two layers of uniform but different properties. The finite difference equations are derived including a pressure-velocity coupling scheme unique to geophysical fluid models. Boundary conditions are specified and the numerical model solution algorithm is presented.

The model results are discussed in the remainder of Chapter 4. Firstly, runs are made for the problem of two-layer flow through an open channel to test mass conservation and geostrophic aspects of the model. Runs are then made on the river discharge problem with various cross-flows specified. Sensitivity to friction, entrainment and diffusion parameters is also evaluated. Finally model results for two plume configurations are compared with actual observations.

In the final chapter (5) a summary of the work is presented.

2. FIELD MEASUREMENTS

2.1 OVERVIEW OF THE LA GRANDE WINTER PLUME

The runoff from the La Grande River, in winter, flows out under the ice as a buoyant plume varying in thickness from 2 to 5 m. Under natural winter discharge conditions, no appreciable salt water intrusion is observed upstream of the 2 m sill at the river mouth. The freshwater plume spreads laterally about 20 km, and is pulled northward by the underlying circulation to a distance of 40 to 50 km; it acquires salt as it moves away from the river mouth. The winter plume is similar in shape and thickness from year to year as can be seen in Peck's (1976b) surface salinity distributions for the winters of 1975 and 1976.

As a result of frictional stress at the ice surface the plume is not as significantly moved around by the underlying tidal flow, as is the Fraser River plume. Maximum tidal velocities within the plume are less than 10 cm sec^{-1}, as can be seen in the inserts of Fig. 3. This semi-diurnal velocity translates the plume horizontally only 1.5 km, making the measurement of salinity relatively insensitive to time of observation. The plume velocity at the river mouth under the 1980 mid-project discharge condition of 1,500 m^3 sec^{-1} was about 43 cm sec^{-1} and through flow divergence dropped to an average of 12 cm sec^{-1} within 3½ km. By the time the flow in the plume reaches the frontal region it has decreased on the average to 3 to 5 cm sec^{-1}. The flushing time for the surface plume (defined as the area contained by the region where horizontal density gradients reach a maximum) is on the order of twelve days.

As can be seen in Fig. 3, the horizontal and vertical density and velocity structure of the water column changes as one proceeds away from the river mouth. For the first 40 km north and 20 km west a very stable, fully stratified region (Ippen, 1966) is present, where the top to bottom density differences are on the order of 0.20 gm cm^{-3}. In this region little exchange with the bottom layer is taking place, and the fresh water spreads out due to buoyancy and advection over the

relatively slow moving deeper salt water layer. For the next 10 to 20 km a frontal region exists where the plume undergoes the maximum rate of exchange of salt. Garvine (1974) showed that in comparing frontal model dynamics with measurements in the Connecticut River plume a strong downward entrainment is most likely in this region, thus acting as a sink for a significant portion of the water in the surface plume. It should be noted that complete vertical mixing does not occur in this region due to the stabilizing effect of the vertical density gradient although tidal kinetic energy underneath the plume (inserts on Fig. 3) has increased from the stable region. Seaward of the front a well-mixed region is evident, where a large increase in tidal kinetic energy and reduction in stratification through vertical exchanges in the frontal region coincide with substantial vertical mixing. In this area, evidence of a return flowing bottom current as predicted by the similarity theory of Hansen and Rattray (1965) can be seen (note the mean velocity profiles in the top insert of Fig. 3).

2.2. FIELD PROGRAM OBJECTIVES AND METHODS

Salinity and temperature versus depth observations collected off the La Grande River in the winters of 1975 and 1976 (Peck 1978) and off Great Whale River in the winter of 1977 (Prinsenberg and Collins 1979) provided a reasonably detailed picture of the lateral and vertical extent of river plumes under an ice cover, but little or no information on the dynamics of momentum and mass transfer taking place between the surface and bottom layers. Therefore, as part of the present study, a two-year field program was organized specifically to obtain flow measurements in and below the plume, and to investigate mixing of fresh and salt water across the plume interface.

The field program carried out in the winter of 1979 was basically a pilot study oriented toward testing new instrumentation and obtaining a first look at the flow field in the plume. Filling of the LG-2 reservoir, which reduced the natural discharge of the La Grande River to 30 m^3 sec^{-1} for almost three months, precluded the study of freshwater

plume dispersion off the La Grande River that year. Nevertheless a limited number of CTD (Conductivity, Temperature versus Depth) and current observations were made off La Grande to collect background salinity, tidal current and general circulation information in northeastern James Bay, in the absence of an under-ice river plume. As well, an important operational lesson was learned with regard to the manned twenty-five-hour current profiler. On January 27 and 28, 1979 a severe storm, with winds from the northeast reaching 80 to 100 km hr^{-1}, caused part of the shorefast ice to break off, setting adrift two fixed current meter moorings. While the current meters were eventually recovered attached to an ice pan only six metres in diameter, a tent, originally a short distance away, never was located. This experience resulted in the decision to develop an unmanned twenty-five-hour current profiler for the following year.

At the beginning of February, 1979, the complete survey was moved to Poste-de-la-Baleine (Great Whale) in order to make flow and mixing measurements for the first time in an under-ice river plume. In addition, the Great Whale River plume study provided a further independent data set, with river discharge and offshore tidal energies significantly lower than either the 1976 or 1980 La Grande plume situations. Also, the bathymetry off Great Whale is more uniform than off La Grande; the depth drops to greater than 50 m within a few kilometres of the river mouth. There are also far fewer islands within the survey area.

The principal field experiment was carried out the following year off the La Grande River. More than twice as many observations were taken than in the previous year, stretching the survey period to 2½ months. This year two helicopters were used to transport personnel to the shore-fast and pack-ice, and the number of operational staff grew to ten. Partial operation of the LG-2 complex resulted in river flows of three times the natural discharge rates (1600 m^3 sec^{-1} in 1980 versus 450 m^3 sec^{-1} in 1976). This additional discharge resulted in a third unique data set. Because it was both comprehensive and represented a median point between pre- and post-project discharge conditions, this

data set was used for the in-depth study of the plume dynamics and mixing as well as calibration of the two-layer model for plume dispersion. Also, since there were three distinct periods of relatively uniform but different levels of discharge over the two-month survey interval, ranging from 1,400 to 1,800 m^3 sec^{-1}, it was possible to use resurveyed CTD station data to assess the response of the plume to short-term changes in river discharge.

To summarize, four unique data sets were obtained to study plume dispersion: 1) the largely CTD data set collected off La Grande in the winter of 1976 under natural discharge conditions, by Peck (1978), 2) the sparse data set collected off the La Grande in the winter of 1979 and used only to assess the background conditions in the absence of a plume, 3) the more comprehensive data set collected off Great Whale for discharges even lower than the 1976 La Grande plume, and 4) the very comprehensive data set collected off La Grande in the winter of 1980 under above-normal discharge conditions.

2.2.1 Observational Network Winter 1979

The station locations for both the 1979 and 1980 La Grande surveys are given in Fig. 4. Between January 23 and February 4, 1979, there were 17 CTD profiles measured in northeastern James Bay, and a single twenty-five-hour current station off the La Grande River mouth. An L-shaped current meter station array was established during this period with two offshore stations located approximately 2 km from the edge of the shorefast ice. These latter two stations lasted only a few days because this section of the shorefast ice broke off as a result of a storm on January 27-28, 1979. Only the current meter station 9 km off the river mouth survived the storm and these results will be presented in section (2.3).

On February 7, 1979, a detailed survey of the Great Whale River plume began. The station locations are given in Fig. 5. Over the course of the three-week survey period, some 150 CTD profiles were measured on a 5 km grid spacing with a Guildline Mark IV system. Five

twenty-five-hour current stations were established along the north-easterly axis of the plume. Water samples for bio-chemical analysis were taken at 17 stations at depths of 2, 3 and 7 m. Unlike the region off the La Grande, the background flow off the Great Whale River was slower (≈2-3 cm sec^{-1}) and directed southwesterly. No significant storms occurred during the period of this survey and only small variations in the background flow were observed. Thus the ice cover remained land-locked and no open water hampered the measurement program.

2.2.2 Observational Network Winter 1980

The survey stations for this two-month field program are given in Fig. 4, along with those for the 1979 La Grande survey. Using the Guildline Mark IV profiler a total of 368 CTD profiles were obtained at 148 stations spaced approximately 6 km apart. About three weeks were required for a survey of the entire CTD station network, which was carried out approximately 2½ times between January 31, and March 31, 1980. Details of the field operations are given in Brooks (1980).

Using previously collected CTD data, 21 twenty-five-hour current profile stations were located on landfast ice along the plume and cross plume axes. In the extreme north a lack of shore-fast ice necessitated a 2 to 5 km shoreward shift in the last three stations; however, these inshore stations exhibited similar salinity characteristics to their offshore counterparts. In order to assess temporal variability throughout the two-month measurement program, some 35 Aanderaa current meters with in-line vanes were rigidly suspended from the fixed ice surface.

To investigate relationships between the physical processes and bio-chemical distributions, water samples were collected at twelve of the along plume and three of the cross plume stations. Two surveys were carried out: one in late February and the other in early March, 1980. Only results from the more detailed second survey, in which samples were taken at five depths (2, 5, 10, 20, 30 m), are presented here.

2.2.3 Field Operations

All current observations were referenced to the ice surface and thus had to be taken from shorefast ice. The outer edge of the land-locked ice as recorded during the 1979 and 1980 La Grande winter surveys is delineated in Fig. 4 and appears to be more dependent on topographic features (islands providing anchoring points) than on inter-annual meteorological or freshwater variations. Storms during the survey period were less severe in 1980 than in 1979, and a major increase in river discharge did take place in 1980, yet the outer edge of the land-locked ice was about the same for the two years.

Seaward of this region, the ice is dynamic with a lead (maximum width 10 km) opening and closing, depending on the direction and intensity of the over-ice wind field. While the open lead increases the possibility of plume mixing due to direct momentum transfer, evaporation and cooling, it does not appear to have a significant effect on vertical mixing for the following reasons: 1) it was refrozen for at least half of the 1980 survey and no substantial difference was observed in the CTD data from the three periods of the survey; 2) the temperatures in the water column are at, or close to, the freezing point for local salinity values and thus the water column can not be cooled much further without the production of ice; 3) while evaporation might be an important source of convective mixing, all measurements of density taken from the floe ice in the lead indicated a very stable density structure, thus precluding convective overturning; and 4) momentum transfer from the wind is minimal as the open fetch distance for wave build-up was small.

Offshore in the pack ice some CTD station locations had to be changed from their assigned position due to open water and pressure ridging in the flow ice, but their eventual position was accurately recorded using a Motorola MR III miniranger. Within the 25 km range of the miniranger, station position could be determined with an accuracy of ±100 m. Inshore, numerous shoals also necessitated some exploratory depth sounding to locate regions of significant depth (>15 m) and relatively smooth surface ice (radius >1 km) to place the twenty-five-hour

current profiling stations. Islands and shoals off the La Grande River (see Fig. 4) not only hampered the operational work, but to a lesser degree the interpretation of background flow patterns.

Throughout the survey period a helicopter was dedicated to the systematic measurement of CTD profiles. At each station a 23 cm diameter hole was drilled in the ice, the ice thickness measured, a depth sounding taken, and the Guildline Mark IV probe lowered slowly down the hole to within 1 m of the bottom. Sampling was carried out at each station in a given line starting from the shore and moving seaward before measurements along the next line to the north were begun. On good flying days, upwards of 15 CTD stations could be visited. However, daily sampling was not always possible as white-out conditions on some days prevented the helicopters from flying. Sampling of previous years' stations ensured that year-to-year comparisons could be made, and interlining between them guaranteed that good spatial resolution was possible. The second helicopter was used to deploy the fixed current meter moorings, the twenty-five-hour current stations, the miniranger transponders, and to obtain water samples for bio-chemical analyses.

Six-litre water samples were collected using specially built PVC and polycarbonate Kemmerer bottles. Under the direction of Dr. J.C. Roff of the Department of Zoology at the University of Guelph, the following variables were measured (Pett, 1981): total phosphorous (TP), total dissolved phosphorous (TDP), total dissolved Kjeldahl nitrogen (TDKN), reactive nitrate plus nitrite (NO_3+NO_2), reactive silicate (SiO_2), adenosine triphosphate (ATP), particulate organic carbon (POC), particulate organic nitrogen (PON), chlorophyll _a_ and phaeopigments. Nutrient and seston variables were determined by methods detailed in Pett (1981), following procedures in Strickland and Parsons (1972), Environment Canada (1974) and MacKinnon (1976). ATP was converted to carbon equivalent (BIOC) by a conversion factor of 250:1 (Holm-Hansen, 1973). All filtrations used Whitman GF/C glass fibre filters.

Ice samples were taken in mid-March 1980 from the top 10 cm and bottom 20 cm of the ice cover at six stations along the plume axis.

River and sea ice samples were thawed and analyzed for salinity, TP, TDP, TDKN, NO_3+NO_2, chlorophyll *a* and phaeopigments, using procedures described above. Snow samples taken at the La Grande River station and two plume stations (132 and 115) were also analyzed for nutrients.

2.2.4 Physical Oceanographic Instrumentation

The principal survey instrument for the measurement of conductivity and temperature versus depth was the Guildline Mark IV CTD system, consisting of a 1.4 m × 15 cm diameter cylindrical in-water probe, a single conductor double armor cable, a lightweight arctic winch, a signal processing control unit and an audio cassette recorder. The sensor package consisted of: a pre-calibrated copper resistance thermometer with an accuracy of ±0.005 °C, a four-electrode cell conductivity sensor with a calibrated accuracy in equivalent salinity of ±0.005°/oo, a strain gauge pressure transducer which gives a depth accuracy ±0.25% full scale, i.e., ±0.25 m for 100 m depth range used in James Bay. The system was calibrated at 10 points over the full range of salinity and temperature values prior to going into the field, checked against bottle casts and autosal measurements during the field survey, and then recalibrated prior to the next year's survey in order to maintain the above quoted accuracies. Two complete systems were maintained in the field.

In order to measure current, conductivity and temperature at discrete depth intervals over the water column, the basic Aanderaa current meter underwent extensive redesign. First an in-line vane was added above the savonius rotor housing and this was magnetically coupled to a compass follower to give current direction relative to the instrument case (recorded on the pressure channel). The standard compass in the bottom of the meter provided the direction of the instrument case relative to magnetic north. A maximum estimated error for the complete direction measurement as determined by in-shop calibrations was ±5°. The standard Aanderaa temperature and conductivity sensors were calibrated to give accuracies better than ±0.02 °C (quadratic calibration

equation) and ±0.05 m Mho/cm (or ±0.04 °/oo salinity). The savonius rotor speed sensor was calibrated in the CCIW tow tank at ten points over the speed range 5 to 25 cm sec^{-1}; the maximum error in speed was ±1.3 cm sec^{-1}. Depth was determined by measuring the amount of cable payed out and was calibrated in the laboratory to achieve an accuracy of a quarter of a metre near the surface and a metre at the maximum depth of 30 m. Additional weight was placed on the bottom of the profiler to ensure that small wire angles were maintained in the flow. A microprocessor controlled winch automatically positioned the modified Aanderaa current meter sequentially at sixteen preselected depths each hour for 25 hours. At each depth, one minute was allowed for the instrument to settle to its new position, then the rotor count for current speed was started, and at the end of two minutes, readings were taken from all five sensors. The ice hole and profiling system were enclosed in a heated Case Existological Laboratories Ltd. (CELL) 2.44 m × 2.44 m × 1.83 m Arctic tent.

An intercomparison of the salinity and temperature data gathered from the Guildline Mark IV and the Aanderaa profiler is given in Fig. 6. The solid lines represent a number of continuous Mark IV profiles taken over the same one hour period required for the Aanderaa profiler to sample at sixteen discrete depths (values marked with an x). The first thing to note is the excellent agreement between the two sets of observations in the regions of relatively small changes in the parameters; that is, above and below the pycnocline. While temperature values agree well in the immediate vicinity of the pycnocline, salinity and thus sigma-t appear to be underestimated by the Mark IV probe. This is the result of a longer settling time associated with the discretely sampling Aanderaa profiler versus the slowly, but continuously, moving Mark IV CTD probe. The Mark IV conductivity cell must be moving in order for the cell to be flushed; the fact that it is moving slowly and mounted in-line rather than on the side, probably results in less than maximum rate of flushing through the four-electrode cell. This would reduce the response time of the Mark IV conductivity measurement below

the non-flushing resistance thermometer. Thus it should be remembered that the pycnocline may be even sharper than indicated by the Mark IV CTD data.

At the mooring stations, Aanderaa current meters (also modified with an in-line vane) were moored from the ice surface with 3 m lengths of 5 cm diameter aluminum poles. At each station every current meter was suspended from the ice surface with its own set of poles, and the near surface moorings included a thermal isolation link to prevent icing of the instrument in the freshwater layer. The sensors were similar to those used in the Aanderaa profiler, with equivalent levels of calibration and accuracy. The only difference was that case orientation was fixed at the surface by alignment of the rigid mooring poles. Thus one less channel of information was required at each 20-minute sampling interval. These current meters were left in for a minimum of thirty days in order to assess lunitidal variations in the current. It should be noted that an incorrect time-code generator used in all the fixed mooring current meters precluded the precise determination of phase in some of the records where missing observations occurred in the data.

2.2.5 Data Processing

A preliminary processing of the Guildline Mark IV CTD data and the Aanderaa current profiler data was carried out each evening in order to assess the validity of the data and to plan the next day's operation. The Guildline Mark IV scans 16 channels at a rate of 40 milliseconds per scan and thus the HP 9825A must sequentially sample this massive data set to pick values of conductivity and temperature at preselected depths. A program on the HP9825A calculates salinity values from conductivity ratio, temperature and pressure using Bennett's formula (Walker and Chapman 1973). The sigma-t values are computed using the modified Knudsen's equation as given by Swears (1970). The freezing point of seawater is calculated using the formulae given in Fujino et al. (1974) with the correct sign in their equation (5). Details of the CTD data processing system are given in Peck (1980).

Most of the computational and editing programs had to be developed for the Aanderaa current profiler. First the raw data in Aanderaa units were keyed into the HP 9825A, and converted to engineering units and a printer listing obtained. A number of profile and time-series plots were then produced to assist in the editing of the speed, direction, conductivity and temperature data each evening.

Because tidally-averaged values were important in the study, special programming was developed upon return from the field. To obtain the mean velocity components, salinity, temperature and sigma-t values, the twenty-five hourly observations at each depth were summed and divided by 25. The tidal velocity components were obtained by calculating the root mean square deviations of the 25 points and then multiplying by $\sqrt{2}$. These time-averaged values were then plotted as profiles and used in the kinetic energy and Richardson number calculations presented later.

The Aanderaa current meter records were processed upon return from the field on the Cyber 176 computer at CCIW. The 20-minute data record was first edited and then filtered using an A_3 A_4 A_4 moving average filter. Hourly values were then run under the tidal streams (harmonic) analysis program to obtain up to 36 tidal constituents, in ellipse form, following the method of Foreman (1978). From these constituents, current predictions were produced over the period of record and compared to hourly filtered values. In addition, these hourly data were run through a low-pass filter A_{24} A_{24} A_{25} to examine longer period variations in the background flow field.

2.3 RESULTS OF PHYSICAL MEASUREMENTS OF THE LA GRANDE RIVER PLUME

The data discussed in this and the following section (2.4) were principally collected during the winter of 1980, as no brackish water plume existed off the La Grande River during the winter of 1979. Some of the 1979 CTD data are presented later in Fig. 20 for comparison with the plume data collected in other years. This data shows that the water

column off La Grande in 1979 was well-mixed, with top-to-bottom salinity differences of less than 2°/oo.

Figure 7 presents some time-series observations from the winter of 1979. The current meter was suspended from the shorefast ice at a depth of 6 m. The station was located 9 km west of the La Grande River mouth. It is interesting to note that the salinity at this depth is slowly increasing over the period of observation, due probably to the reduced discharge at this time of year of the rivers flowing into James Bay. Tidal current amplitudes during spring tides reach 20 cm sec^{-1}, while the mean current is generally only a few cm sec^{-1} to the northeast. The mean current increases dramatically to values of the order of 10 to 15 cm sec^{-1} and switches direction to the northwest upon passage of a storm on January 27-28, 1979. This increase in mean flow doesn't die off until some 10 days after the storm has abated. Thus it appears that momentum, either through pressure gradient or surface stress, is transferred across the pack ice and contributes significantly to the forcing of the background circulation in James Bay, even in the presence of an ice cover.

In the remainder of this section data collected in the winter of 1980 will be discussed. Figure 8 gives the station locations and numbers for data plotted as vertical cross-sections. The horizontal contour plots, however, use all the CTD stations given in Fig. 4. It should be noted that the along plume axes for CTD and current profile observations diverge by 2 to 5 km northwest of station 126, due to the operational requirement for land-fast ice. Nevertheless, the sections are similar; a significant decrease in depth in the vicinity of station 122 is characteristic of both sections, and the salinity is well-mixed in this region.

2.3.1 Salinity-Temperature Distributions

Horizontal contours of the mean surface salinity (i.e., above the pycnocline) are also given in Fig. 8. These contours suggest that the river plume flows northwestward under the ice, parallel to the east

coast of James Bay. A sharp density front, a region of maximum horizontal rate of change of salinity, can be observed approximately 20 km offshore and a less intense front some 40 to 50 km northward from the river mouth. The relatively persistent northwesterly background flow is responsible for stretching of the northward front.

Salinity and temperature sections along the plume axis, and across the axis (see insert) are plotted in Fig. 9; these show a sharp halocline at about 3 to 4 m depth out to 40 km from the river mouth. Above the halocline the fresh or brackish water is vertically homogeneous, while below a more diffuse structure, that is indicative of vertical mixing, can be observed. This sub-pycnocline mixing of the freshwater into salt water increases in the seaward direction. Similar features are observed in the cross plume direction. The temperature pattern basically mirrors the salinity distribution and is generally at the freezing point for local salinity values.

A series of vertical salinity, temperature and sigma-t profiles computed from Guildline Mark IV CTD data are presented in Fig. 10. The profiles are obtained from stations along the main axis of the plume from the fully stratified region at the river mouth (upper right-hand corner) to the well-mixed region in the far-field (lower left-hand corner). The numbers in brackets indicate the distance from the river mouth along this axis and the station locations are given in Fig. 8. The sharpness of the pycnocline in the fully stratified region is well illustrated. Between stations 136 and 132 evidence of downward mixing can be observed in a zone of linearly changing density structure just below the pycnocline. At station 122 vertical diffusion seems to be very strong as no discernible pycnocline is evident. For the last two stations well-mixed conditions are observed.

Data at these same stations are also plotted on a T-S diagram in Fig. 11. The first point to note is that at the small range of temperatures in the water column at this time of year, density (sigma-t) is entirely a function of salinity and not of temperature. Also it can be seen that most of the temperature values, particularly in the lower

layer below the surface plume, are close to the freezing point of seawater. In the upper layer a greater spread in temperature values is observed due to the injection of warmer plume water, which has not had a chance to cool completely to the freezing point. The five or six apparently supercooled values are a result of the conductivity time response problem pointed out earlier; that is, on the downcast the measured salinity underestimates the true salinity at that depth and temperature.

A number of CTD stations were repeated over the 2½ month survey period. Surface salinity values from these stations are plotted in Fig. 12. From this analysis it is possible to assess the response of the plume to short-term changes in river discharge. For the first three weeks in February the La Grande River discharge was nearly uniform at 1,400 m^3 sec^{-1}, then it rapidly increased to 1,800 m^3 sec^{-1} for the next three weeks, and finally decreased to a uniform 1,500 m^3 sec^{-1} until the end of the survey. The mean surface salinities in the mid-plume region appear to be negatively correlated with increasing discharge; that is, as the freshwater discharge increases the mean surface salinity decreases. Beyond the density front of the plume, where horizontal gradients are less, very little change in surface salinity can be observed over the period of the survey.

2.3.2 Analysis of Currents

The tidally-averaged profile data from a representative twenty-five-hour station in the river plume is given in Fig. 13. Just under the plume a strong mean flow to the north-northwest can be observed along with a region of intense tidal activity. Above the pycnocline, however, the mean and tidal current amplitudes are much lower, with the mean flow switching direction to the west. The large interfacial density gradient seems to decouple motion in the plume from the underlying flow and a frictional boundary layer near the ice surface further reduces flow in the upper layer. The mean density and temperature profiles indicate the presence of a well-mixed region above the

pycnocline with a more diffuse region in the first few metres below. The dash-dot lines, typical of the tidal variability at most plume stations, indicate that a small displacement of the interface takes place over the tidal cycle.

The mean currents at the surface (i.e., within 1 m of the ice/water interface) are plotted in Fig. 14. At the river mouth (station 260) and in the channel (350) the mean flow is about 45 cm sec^{-1}. Just beyond the sill (stations 360, 150, 361) the flow spreads out and is reduced to an average of about 15 cm sec^{-1}. Why the flow in this region is to the west-southwest rather than the more expected west-northwest is uncertain. Further offshore the surface flow continues to diverge and within 15 km of the river mouth the flow has dropped to an average of about 2 cm sec^{-1}.

Analysis of tidal streams at three representative current meter stations is shown in Table II. Data from station 260, located in the river mouth, shows a mean flow to the west of about 50 cm sec^{-1}; this flow is modulated by tidal propagation up the river. Station 01A, located 10 km offshore and to the south of the plume, provides time-series information on the background flow. The mean flow is to the northwest at 5 cm sec^{-1} near the surface, and decreases to 2 cm sec^{-1} at 10 m depth. The M_2 tidal current, with its major axis oriented east-west, is four times as large as the mean flow. Current meters at station 238, located near the downstream frontal region, register mean flows of 5 cm sec^{-1} to the northwest at the plume interface, but these decrease to 3 cm sec^{-1} below it. At all stations the diurnal to semi-diurnal tidal current ratio suggests that there is little diurnal inequality in current meter data over the period of the survey. However, the fortnightly (S_2/M_2) and lunitidal (N_2/M_2) ratios show that a 50% modulation of the M_2 tidal flow can occur over the month and should not be ignored in intercomparing the non-concurrent twenty-five-hour stations. Therefore, in the mixing computations introduced later, the stations have been carefully selected such that the tidal range at

the time the observations were made is close to the RMS tidal range over the two-month survey period.

2.3.3 Kinetic Energy Distributions

The twenty-five-hour current profile data were used to compute kinetic energy distributions, which are plotted in Fig. 15 in along and cross plume vertical sections. The dashed line represents the pycnocline depth, defined as the location of the maximum vertical gradient in density. Northwestward of station 132 a well-mixed region exists, where top-to-bottom salinity differences are only a few parts-per-thousand and no definite pycnocline is evident. In this region the dashed line represents the depth of mean salinity of the water column.

As can be seen in Fig. 15 the kinetic energy of the mean flow is concentrated in the first 5 km of the river plume and decreases rapidly seaward as the plume spreads out laterally. The sharp decrease in the depth of the pycnocline would suggest that a degree of internal hydraulic control exists off the river mouth, as pointed out by Stommel and Farmer (1953). The mean flow kinetic energy is less than 25 cm^2 sec^{-2} in all the regions below the plume except at station 243, where a slight increase in the local background flow is observed. Tidal kinetic energy within the plume at the river mouth is less than the mean flow kinetic energy and appears to modulate river discharge rather than contribute to plume mixing. Seaward of the river mouth the tidal energy within the plume dies off rapidly, with very little tidal energy penetrating the plume interface from below. In the basin, between stations 252 and 132, a substantial increase in tidal kinetic energy can be observed just below the plume; it is in this area that sub-pycnocline mixing, as can be seen in the salinity section of Fig. 9, is initiated. However, in the vicinity of station 122 there is a substantial increase in tidal kinetic energy in the basin, which, together with reduced vertical stratification, contributes to the almost complete vertical mixing of the water column observed at station 126 in Fig. 9.

2.3.4 Interfacial Froude Number Computations

The potential for vertical mixing in a well-stratified water column can be quantified by the interfacial Froude number:

$$F_i = \frac{v_{12}}{\left(g \frac{\Delta\rho}{\rho_\infty} \cdot \frac{h_{01} h_{12}}{h_{02}}\right)^{\frac{1}{2}}}$$

where v_{12} is the relative root-mean-square current speed between the upper and lower layer and is always a positive number; h_{01} and h_{12} are the upper and lower layer thicknesses; h_{02} is the total depth (h_{01}+ h_{12}); $\Delta\rho$ is the top-to-bottom density difference; ρ_∞ is the bottom density in the far-field. As the kinetic energy increases or the stability of the water column decreases, the potential for increased mixing is reflected in higher absolute values of interfacial Froude numbers. In Fig. 15 a sign has been added to the calculated value of the Froude number to indicate the direction in which entrainment is likely to occur, with positive upward entrainment into the plume and negative downward into the basin. The sign is determined by subtracting the lower layer root-mean-square current speed from the upper layer RMS current speed.

Station values of interfacial Froude are given in the lower diagram of Fig. 15. The first point to note is that all values are subcritical; that is, less than one, and thus jet-like turbulent entrainment is not expected to occur even in the high flow area off the river mouth. While there is a reasonably large positive value in this region, it doesn't seem to correlate with a significant increase in salinity in the plume (Fig. 9). Thus, off the river mouth there must be a conversion of kinetic energy to potential energy (thinning of the plume) without significant dissipation through the production of turbulence at the relatively smooth ice surface. McClimans (1979) suggests that a phenomenon known as Bernoulli suction can lift the basin water without entraining it into the plume. For the next 25 km the sign is negative,

and the interfacial Froude number gradually increases in value to a maximum of 0.57 at station 132 in the frontal region of the plume (see Fig. 9). It would appear that over this entire distance, downward entrainment (i.e., evacuation of surface water out of the plume) is taking place (note: water in the plume has only a twelve-day residence time). At the same time, some lateral or vertical diffusion must be taking place to account for the seaward increase in salinity in the plume. Northwest of station 132, the sign changes to positive, suggesting the possibility of upward mixing. This region is indicative of the partially-mixed estuaries modelled by Hansen and Rattray (1965) in which turbulent mixing results primarily from tidal currents, and is largely uninhibited by vertical stratification.

2.4 CHEMICAL AND BIOLOGICAL CHARACTERISTICS OF LA GRANDE RIVER PLUME*

Correlations among physical and biological parameters are presented in Table III. The positive correlations of total and dissolved nutrients with salinity indicate a predominantly marine source for nutrients at this time of the year. Of all the dissolved nutrients, SiO_2 shows the lowest correlation coefficient and thus the greatest departure from a conservative substance. Seston values on the other hand are negatively correlated with salinity, indicating a predominantly riverine source of particulate and biological carbon.

2.4.1 Nutrient and Seston Distributions in the Water Column

Sections showing reactive silicate and nitrate plus nitrite are plotted in Fig. 16. The lowest values of SiO_2 (≈ 8 µg-at ℓ^{-1}) are found in the river, while the highest values ($SiO_2 > 20$ µg-at ℓ^{-1}) are observed below or seaward of the plume. The maximum concentration of SiO_2

* The material in this section on chemistry and biology was jointly prepared by Dr. J.C. Roff, Mr. R.J. Pett and myself for the paper Freeman et al. (1982) and is included for completeness of the discussion on processes in under-ice river plumes.

(33.5 µg-at ℓ^{-1}) occurs in the vicinity of strong tidal mixing (stations 0126 and 0132), suggesting that resuspension of bottom sediments takes place in this shoaling area.

Biological carbon and particulate organic carbon data are plotted on along plume and cross plume sections in Fig. 17. The highest BIOC (≈5 µg ℓ^{-1}) and POC (195 µg ℓ^{-1}) values are found near the river mouth, while background levels are less than 2 µg ℓ^{-1} and 50 µg ℓ^{-1}, respectively. Once again a region of higher biological carbon can be observed in the vicinity of the intense tidal mixing (stations 132 and 126), suggesting bottom resuspension of detritus.

PON concentrations (<2 µg ℓ^{-1}), are very low during the second survey (March 6-12) with C:N ratios all exceeding 14:1. Also, NO_3+NO_2 values and C:N ratios are higher both in marine waters and in the plume than during the first survey (February 19-26). River samples also show an increase in NO_3+NO_2 values and C:N ratios between the two surveys, see Pett (1981). Thus there is evidence of nitrogen remineralisation in both fresh and marine waters at this time of year, with almost complete remineralisation by the end of the second survey period. Chlorophyll a concentrations in the river, plume, and marine waters are very low (Fig. 18), and differed little between the two survey periods.

Nutrient values reported off the La Grande estuary in March 1974 by Grainger and McSween (1976) are similar to those found during this survey. Nutrient concentrations in Feb-March 1980 range from 0.2 to 1.11 for TDP, 1.0 to 3.9 for NO_3+NO_2 and 3.2 to 33.5 for SiO_2 (all values in µg-at ℓ^{-1}). Mean values for these variables from Grainger and McSween (1976) are approximately 0.6, 2.5, and 15 respectively, very close to our mean values at similar salinities. Two points may be made from this pre- and post-project comparison: (i) Grainger and McSween (1976) stated that the La Grande River provides minimal nutrient contributions to James Bay and the winter data in this study supports this view; (ii) the increased winter discharge appears to have had little effect on nutrient concentrations in the Bay.

2.4.2 Bio-Chemical Distributions in the Ice and Snow

Salinity in the ice increases offshore (Fig. 18), consistent with increasing brackish plume water. There appears to be a top-to-bottom salinity gradient within the ice; lower salinities are generally found at the bottom of the ice, much lower than in the underlying sea water - a consequence of the solute rejection during growth of the sea ice. The along plume distribution of nutrients (TDP, NO_3+NO_2) is more variable than salinity, and a weak seaward gradient at the bottom of the ice can be detected for NO_3+NO_2. NO_3+NO_2 concentrations in surface ice are generally a factor of two or three greater than those in the water immediately below the ice layer. Levels of NO_3+NO_2 in the snow cover are higher still (15 to 20 µg-at ℓ^{-1}), indicating that melting ice and snow cover may be an important nutrient source to James and Hudson Bays, at least temporarily, during the spring phytoplankton bloom.

Perhaps the most important feature of the ice cover is the marked development of the ice flora. High chlorophyll *a* concentrations (to 10 µg ℓ^{-1} and higher) are observed in a distinct 2 cm thick brown layer at the bottom of the ice at the three stations (126, 115, 621) where vertical mixing of the water column appears to be taking place. These concentrations are two to three orders of magnitude greater than found in underlying James Bay waters, the surface ice, or upstream in the river. There is no significant development of an ice flora in the plume area itself.

The distribution of phaeopigments parallels that of chlorophyll *a* with the highest value (4.3 µg-at ℓ^{-1}) in the brown ice layer and the lowest value inshore. High ratios of chlorophyll *a* to phaeopigments indicate that there is a reasonably healthy algal population growing under the ice seaward of the stabilizing river plume. This ice biota community is already well established by the end of February. High levels of POC (1 µg/ℓ) and PON (200 µg/ℓ) are also found in the bottom ice layer associated with high chlorophyll *a* levels. C:N ratios as low as 5.6:1 in these samples indicate an active uptake of labile nitrogen from ice or water.

The presence of a sea ice algal community in Arctic waters is now well documented, e.g., Hsiao (1980). Observations from Hudson Bay (Dunbar and Acreman 1980) and James Bay (Roff and Gerrath 1979 unpublished data) show that it is a widespread and well developed feature of these Bays. Unfortunately there are few estimates of the seasonal production of this ice biota. The estimates of Grainger (1979) and Alexander (1974), that the ice biota may contribute 10% of the annual primary production, are probably conservative. Clearly this important community and its relation to freshwater plumes requires closer study.

2.4.3 Flora and Fauna

The flora and fauna of the La Grande plume and ice layers have not yet been examined in detail; however, very different algal communities are found in the surface and bottom ice layers (see also Hsiao 1980), the plume, and in the surrounding marine waters. The plume itself contains several freshwater species and undoubtedly acts as a dissemination mechanism as suggested by Gerrath et al. (1980) and Barber and Murty (1977). Also, it would appear that the river plume acts to limit the supply of nutrients to the surface layer, thus restricting growth of algal communities under the ice to regions seaward of its stabilizing influence.

2.5 DISCUSSION OF PLUME MIXING

Thus far correlations of the biological and physical features of a single plume under one set of mixing conditions have been examined - the La Grande 1980 plume (discharge $\approx$1,600 m^3 sec^{-1}, kinetic energy $\approx$300 cm^2 sec^{-2}). CTD observations taken in 1976 off La Grande enable the study of mixing under a much-reduced discharge (discharge $\approx$500 m^3 sec^{-1}) but similar tidal mixing regime (kinetic energy $\approx$300 cm^2 sec^{-2}). Additional CTD and current profile observations made off Great Whale in 1979 permitted the effects of a further-reduced discharge (discharge $\approx$200 m^3 sec^{-1}) and an order of magnitude lower tidal energy (kinetic energy $\approx$25 cm^2 sec^{-2}) to be studied. Because vertical profiles of

currents are not available for the 1976 survey, the twenty-five-hour data collected in 1980 at the same 1976 CTD stations are used for the RMS velocity calculations. This is possible since the river plume is basically in isostatic equilibrium (Garvine 1974) and will not substantially affect tidal flow velocities and basin-wide circulation.

2.5.1 La Grande and Great Whale Plume Comparisons

Mean surface salinity contours and pycnocline depths for the three plume configurations are plotted in Fig. 19 at the same scale for ease of comparison. The shape of the Great Whale plume differs considerably from the La Grande plumes due to the fact that the prevailing background flow (alongshore to the south) is counter to the geostrophically-balanced flow in the plume (alongshore to the north). As a result, the northern portion of the plume is deflected offshore while the southern section is seen to hug the shoreline. The general steepening of the density front in the north and elongation in the south is a result of the interfacial shear stress caused by the southerly underlying flow. The concavity in the surface contours of the Great Whale plume may also be related to increased vertical mixing over shoals (20 m deep) located approximately 10 km off the river mouth. For the La Grande plumes, the prevailing background flow is alongshore to the north (see mean flow inclinations given in Table II). Since the geostrophically-balanced plume flow and the underlying coastal current are in the same direction, the La Grande plume stays close to the coast and is dragged northward by the underlying flow.

As can be seen in the top diagram in Fig. 19 the minimum pycnocline depth (1 m) for the Great Whale River plume coincides with the 25°/oo surface salinity contour. For the 1976 and 1980 La Grande plumes the minimum pycnocline depth lies along the 5°/oo and 15°/oo salinity contours, respectively. The pycnocline minimum (as seen in Fig. 15) appears to separate the downward entrainment region from the seaward tidal mixing region. The bottom salinity in winter at the mouth of James Bay and in the deep water off the Great Whale River, Hudson Bay

is about 30°/oo, and it is this value that is used as the base salinity in the freshwater content estimates. For ease of discussion the region contained within the minimum pycnocline depth is designated 'surface plume', and the region between the minimum pycnocline depth and the 25°/oo surface salinity contour is called the 'well-mixed' plume.

In comparing the two La Grande plumes, it can be seen that increased discharge moves the frontal regions further offshore as well as generally increasing the thickness of the plume. The minimum pycnocline depth (h_{min} = 2.5 m) also shifts offshore with increased discharge. It is interesting to note that under a low tidal energy regime (Great Whale 1979) and even in spite of low discharge, the area of the surface plume is much larger than in the high tidal energy regime (La Grande 1976 and 1980). When the discharge is increased under similar tidal energy conditions (comparing La Grande 1976 and 1980) the area of the surface plume is increased and the location of vertical mixing is shifted seaward; these effects were also found by Festa and Hansen (1976) in their two-dimensional numerical model of estuarine circulation.

In Fig. 20 the vertical salinity profiles at similar distances from the river mouth are plotted for the various background flow conditions discussed above. As can be seen, the low discharge of the La Grande River in 1979 completely eliminated the surface plume. Also it is interesting to note that the bottom salinities for the three La Grande plume cases do not change significantly with changes in river discharge. The higher discharge in 1980 causes the surface plume to deepen and to be observed at a much greater distance from the river mouth. In comparing the 1979 Great Whale plume and the 1980 La Grande plume it can be seen that even with a lower discharge the two layer fjordal structure of the Great Whale plume is more sharply defined for greater distances from the river mouth than the much higher discharge 1980 La Grande plume. One final observation is that the pycnocline depth gradually decreases in the axial direction away from the river mouth in each case where there is a surface plume.

2.5.2 Freshwater Content Estimates

Table IV gives the freshwater content estimates relative to a base salinity of 30°/oo computed by planimetering the area within salinity contours, and multiplying by the average salinity deficits and pycnocline depths. Resident times were then computed by dividing these freshwater content estimates by the river discharge. For the La Grande 1980 plume (March 1-9) an independent check on the freshwater content estimates was made by vertically integrating the freshwater deficit profiles at each of the CTD stations and then integrating these values horizontally. The values obtained in this manner agree within 10% of the more approximate method used for the plume intercomparisons. Two computations were made for each plume, the resident time in the surface plume ($\Delta t_{h_{min}}$) and in the well-mixed plume ($\Delta t_{25°/oo}$). River water appears to reside longer in the Great Whale surface plume (h_{min} = 1 m) than in either of the La Grande surface plumes, due principally to the low ambient tidal mixing. It is interesting to note that the residence time estimates for the 1976 and 1980 La Grande plumes are of similar magnitudes even though the discharge for the two years varies by more than three times. This would suggest that, because of the similar tidal and topographic conditions off La Grande, the volume of freshwater contained within the plume varies directly with the level of the river discharge, i.e., the buoyancy input.

2.5.3 Dimensionless Parameters

To examine further the mixing processes in river plumes a number of dimensionless parameters were computed following Fischer's (1972) approach to vertical mixing in a river estuary. The three dimensionless parameters are estuarine Richardson number, plume densimetric Froude number and non-dimensionalized friction velocity, defined respectively as follows:

$$Ri_E = \frac{g\Delta\rho/\rho_\infty \; Q_o/\bar{b}}{u_{12}^3}$$

$$F_p = \frac{\upsilon_1}{\sqrt{g\Delta\rho/\rho_\infty h_{01}}}$$

$$u' = \upsilon_{1,2} / u^*$$

where g is the gravitational acceleration; $\Delta\rho$ is top-to-bottom density difference; ρ_∞ is background density taken as 1.020; Q_o is river discharge; $\bar{b}$ is the mean width of the plume; υ_1 and υ_2 are the root-mean-square current speeds in the upper and lower layers respectively; h_{01} is the plume thickness; and u^* is the local friction velocity.

Since the velocity profiles are not sufficiently detailed near the under-ice or bottom boundaries to compute u^*, the results of the dimensionless analysis are only applicable to other ice-covered locations with similar ice and bottom roughness. Also, in order to apply the analysis to the horizontally two-dimensional plumes a width scale had to be found ($\bar{b}$) to replace the estuarine width. Since Q_o/b from Fischer (1972) represents the buoyancy flux per unit width, division by the layer thickness (h_{01}) gives a measure of the local freshwater discharge velocity. Then for the river plume a similar estimate of the local freshwater discharge velocity can be obtained by dividing by the average width of the plume and the mean layer thickness. The mean plume width $\bar{b}$ was obtained by averaging the distances normal to the shoreline out to the frontal region. A single value is used for each of the three plume configurations and any errors in the estimate of $\bar{b}$ only shift the estuarine Richardson number by a few percent.

The first dimensionless number is plotted in Figure 21 against inverse mixing parameter $\Delta s/\bar{s}$ proposed by Hansen and Rattray (1966); here Δs is the top-to-bottom salinity difference and $\bar{s}$ is the mean salinity of the water column. It should be noted that mixing decreases as $\Delta s/\bar{s}$ increases. In the main part of the figure, data for the three plume discharge conditions fall on, or close to, two asymptotic lines. Looking at the diagram from right to left (i.e., seaward), the shallow initial slope of the first line suggests that mixing is only weakly

dependent upon estuarine Richardson number, and that once a critical value is reached (around 1.0) a significantly increased dependence occurs. Measuring slopes from the diagram results in the following mixing relationships:

$$Ri_E > 1.0 \quad \frac{\bar{s}}{\Delta s} = 1.33\ Ri_E^{-1/6}$$

$$Ri_E < 1.0 \quad \frac{\bar{s}}{\Delta s} = 3.23\ Ri_E^{-3/4}$$

The first relationship, which basically applies to the surface plume, represents a slow entrainment across a well-stratified salt wedge type interface; the second relationship applies generally to the offshore region of the plume, where large tidal currents and shoaling bottom topography contribute to a more turbulent two-way exchange of salt, typical of partially-mixed estuaries. Ippen (1966) found a similar relationship for the correlation of the diffusivity coefficient under stratified and neutral conditions with the local stratification parameter for mixing experiments in a two-layer channel flow ($\alpha\ Ri_E^{-\frac{1}{4}}$). Kato and Phillips (1969) obtained a slightly larger power for the Richardson number dependence on the entrainment in a turbulent layer of a stratified fluid ($E = 2.5\ Ri^{*-1}$).

In the insert of Fig. 21 the plume densimetric Froude number is plotted against a more sensitive indicator of plume mixing at low salinities, the surface salinity. As can be seen, no correlation appears to exist. Within the first 5 km of the river mouth, the region where the plume Froude number was largest in 1980, the surface salinity is less than 0.1°/oo. This would suggest that even though the plume Froude number just off the river mouth is reasonably high (but still subcritical) there is not sufficient surface roughness on the underside of the ice or at the plume interface to generate the turbulence needed to mix the underlying salt water into the plume. Fischer (1972) also was

unable to find any systematic dependency of the mixing coefficient on the freshwater discharge densimetric Froude number.

2.6 CONCLUSIONS BASED ON THE FIELD OBSERVATIONS

The spreading and mixing of river plumes under a solid to close-packed ice cover in James and Hudson Bays appears to involve three different dynamical regions as the surface water moves progressively further away from the river mouth. Within the first 5 to 10 km (stns. 260 to 250) a large horizontal divergence of the river flow takes place, accompanied by a substantial reduction in average flow velocities within the plume, as well as a significant thinning of the interface. This internal hydraulic adjustment seems to occur without significant diffusion or entrainment of salt into the plume. For the next 25 to 30 km (stns. 252 to 132) downward entrainment, associated with an increase in tidal kinetic energy just under the plume and reflected in a growing negative interfacial Froude number, seems to evacuate water from the surface plume as the upper layer continues to thin out. While there appears to be a net mass flux of brackish water out of the plume, there must be a slow diffusion of salt into the plume, as is indicated by the minus one-fifth power dependence of mixing parameter ($\bar{s}/\Delta s$) on estuarine Richardson number. At the seaward end of this region, a frontal area exists where horizontal gradients in salinity are a maximum and where the interfacial Froude number indicates a greater potential for downward mixing than over the rest of the region. Seaward of the plume front, tidal currents substantially increase, primarily due to shoaling bathymetry, and vertical mixing of the water column appears to take place. In this third region the mixing rate is substantially increased with a minus three-quarters power dependence on estuarine Richardson number.

It is only in this latter well-mixed region that a large increase in dissolved labile nutrients is observed in the water column. Concentrations are higher near the under surface of the ice, where an ice flora community is well established by the end of February. In addition, the bio-chemical analyses support the view of an earlier study by

Grainger and McSween (1976) that the La Grande River provides minimal nutrient contributions to James Bay at least in the winter time, and that increased discharge is likely to have little effect on nutrient supply to the Bay. However, insofar as the areal extent of the surface plume seems to be strongly dependent on discharge rates as determined by freshwater content estimates, then it is expected that the post-project surface plume will be larger in area. This in turn will limit nutrient supply to the surface layer for a larger area of northeastern James Bay. This effect may be minimized somewhat in the northwest direction by the strong tidal mixing related to shoaling bottom topography.

3. PLUME MODELLING CONSIDERATIONS

3.1 BACKGROUND

The analysis of the field observations described in the previous chapter shows that river water spreads out under the ice cover as a distinct surface layer varying in thickness from 2 to 4m. Over most of this surface plume there exists a strong pycnocline, across which a decoupling of the flow field seems to occur. Near the river mouth, substantial horizontal gradients in the current are also observed as the river velocity rapidly diverges. The pycnocline in this near-field region represents a stable interface, with almost no entrainment of salt water across it. Further offshore, the surface plume is bounded laterally by a horizontal density front of the order of 2°/oo per km. Salt diffuses slowly in from the sides and bottom of the surface plume, while brackish water appears to be entrained downward. An analysis of salinity deficit versus estuarine Richardson number indicates that there are two distinctly different regions of plume mixing in the far-field. Landward of the frontal region a minus one-sixth power dependence on estuarine Richardson number suggests a slow diffusive process, indicative of a salt wedge estuary. Seaward of the frontal region, tidally generated turbulence increases the rate of mixing (minus three quarters power dependence on estuarine Richardson number) such that an almost complete mixing of the water column takes place. It is the former, more stratified region that will be modelled in the remainder of this study.

In this chapter some general concepts of mixing in stratified flows are presented, and two simple models of plume dispersion are discussed. First, however, a scale analysis of the general momentum equations for the near- and far-field of the plume and for the background basin flow is undertaken. The momentum and turbulent kinetic energy equations are then tidally-averaged to ascertain the effect of tidal current shear on momentum transfer and vertical mixing. The role of entrainment and diffusion in two-layer flow is discussed and appropriate formulations are proposed. A far-field integral model, which neglects

the Coriolis force, is derived and the role of a critical Froude number in the downstream termination of the plume is discussed. Finally, an analytical far-field model is solved for appropriate values of horizontal and vertical salt diffusion coefficients.

3.2. SCALE ANALYSIS OF THE GOVERNING EQUATIONS

A right-hand tangent plane coordinate system that rotates with the angular velocity of the earth is used in all equation derivations. The positive x-axis points in the easterly direction, the positive y-axis in the northerly direction (i.e., with respect to true north not magnetic north), and the z-axis points vertically upward. The u, v, w velocity components respectively point in the x,y and z directions. As is usual for geophysical fluid dynamics problems, the vertical Coriolis terms are neglected. Also a steady state solution for constant river discharge is sought, in keeping with the analysis of the previous chapter. The Boussinesq approximation is made a priori (see Simons 1980) and stipulates that variations of density can be neglected except in the buoyancy terms in the momentum equations. This approximation also reduces the continuity equation to a zero divergence constraint on velocity. In this initial analysis the eddy viscosity formulation of the turbulent Reynold's stress terms is employed.

To compare the magnitudes of various terms in the equations of motion, for both plume and basin flows, characteristic velocity and length scales can be introduced. Let U, W, L, and H represent the horizontal and vertical velocity and length scales, respectively. A pressure scale can also be introduced based on the barotropic pressure field $\rho_\infty g\eta$. Thus the nondimensional quantities become

$$x^*, y^* = x, y/L \quad ; \quad z^* = z/H$$

$$u^*, v^* = u, v/U \quad ; \quad w^* = w/W$$

$$P^* = P/\rho_\infty g\eta$$

If the nondimensionalized velocities and space variables are substituted into the continuity equation, as follows

$$\frac{U}{L}\left[\frac{\partial u^*}{\partial x^*} + \frac{\partial v^*}{\partial y^*}\right] + \frac{W}{H}\left[\frac{\partial w^*}{\partial z^*}\right] = 0 \qquad (1)$$

then a relation for the vertical velocity scale is obtained in terms of the horizontal velocity scale and the vertical and horizontal length scales.

$$W \simeq HU/L$$

Substitution of the nondimensional variables into the momentum equation yields the following set of equations for the x, y and z directions, respectively.

$$\frac{U^2}{L}\left[\frac{\partial(u^*u^*)}{\partial x^*} + \frac{\partial(v^*u^*)}{\partial y^*} + \frac{\partial(w^*u^*)}{\partial z^*}\right] = -\frac{g\eta}{L}\left[\frac{\partial P^*}{\partial x^*}\right] + \frac{A_H U}{L^2}\left[\frac{\partial^2 u^*}{\partial x^{*2}} + \frac{\partial^2 u^*}{\partial y^{*2}}\right] + \frac{A_V U}{H^2}\left[\frac{\partial^2 u^*}{\partial z^{*2}}\right] + fU\left[v^*\right] \qquad (2)$$

$$\frac{U^2}{L}\left[\frac{\partial(u^*v^*)}{\partial x^*} + \frac{\partial(v^*v^*)}{\partial y^*} + \frac{\partial(w^*v^*)}{\partial z^*}\right] = -\frac{g\eta}{L}\left[\frac{\partial P^*}{\partial y^*}\right] + \frac{A_H U}{L^2}\left[\frac{\partial^2 v^*}{\partial x^{*2}} + \frac{\partial^2 v^*}{\partial y^{*2}}\right] + \frac{A_V U}{H^2}\left[\frac{\partial^2 v^*}{\partial z^{*2}}\right] - fU\left[u^*\right] \qquad (3)$$

$$\frac{U^2}{L}\frac{H}{L}\left[\frac{\partial(u^*w^*)}{\partial x^*} + \frac{\partial(v^*w^*)}{\partial y^*} + \frac{\partial(w^*w^*)}{\partial z^*}\right] = -\frac{g\eta}{H}\left[\frac{\partial P^*}{\partial z^*}\right] - g + \frac{A_H U}{L^2}\cdot\frac{H}{L}\left[\frac{\partial^2 w^*}{\partial x^{*2}} + \frac{\partial^2 w^*}{\partial y^{*2}}\right] + \frac{A_V U}{H^2}\cdot\frac{H}{L}\left[\frac{\partial^2 w}{\partial z^{*2}}\right] \qquad (4)$$

Table V gives the results of the scale analysis for typical values in the near-field and far-field of the plume as well as in the basin (James Bay). The values of the eddy viscosity coefficients used are at

the lower range of those used on the Great Lakes (James Bay has about the physical dimensions of Lake Huron).

The first point to note is that the vertical (z) momentum equation is totally dominated by the gravitational and pressure gradient terms, with the advective and diffusive terms eight orders of magnitude smaller. This leads to the usual hydrostatic approximation in which the gravitational acceleration is balanced by the vertical pressure gradient.

For the x and y momentum equations the dominant term in all cases is the vertical diffusivity. When this is balanced against pressure gradient a free surface deviation of the order of 1 cm is required. In assessing the plume near-field, the inertial, Coriolis, and horizontal diffusivity terms are all of the same order of magnitude and should come into play as the river velocity increases. In the plume far-field the inertial terms decrease in importance but vertical friction still plays the dominate role. However, in the basin the balance is basically geostrophic with vertical friction an order of magnitude smaller than the dominant terms. Thus in order to model both the near- and far-field of the plume the full Navier Stokes equations with Coriolis acceleration should be retained.

3.3 TIDALLY-AVERAGED EQUATIONS

At this point it is useful to examine the effect of tidal currents on the formulation of the gradient Richardson number and thus the generation of tidally-induced turbulence.

3.3.1 Component Decomposition

So as to take into account tidal currents as well as the turbulent character of the flow, each of the velocity components and the scalar properties of the fluid are divided into three components, as follows

$$\phi = \overline{\phi} + \tilde{\phi} \cos \omega t + \phi' \qquad (5)$$

where ϕ represents the total velocity components in index notation (u_i + $u_1 = u$, $u_2 = v$, $u_3 = w$), as well as the complete salinity (s), density (ρ), and pressure (P) fields. The first term on the right is the mean value of the parameter averaged over one or more tidal periods; the second term represents a single tidal constituent, such as the M_2 tidal component where $\omega = 2\pi$ /(12.4 hrs); and the third term is the turbulent component with time scales much less than the tidal period. Each of these three components represent significant energy levels in different frequency bands and thus are separable from one another.

Using the familiar Reynolds averaging, the expressions for the decomposed quantities are substituted into the equations of momentum, mass, and salt conservation, and the equations are then averaged over some suitable time scale. For this analysis a semi-diurnal tidal period is appropriate as this time interval is generally less than that for changes in the mean flow (order of days) and much larger than turbulent fluctuations (periods on the order of seconds to minutes). An example of tidal averaging of the quadratic quantities found in the inertial terms is given in index notation below.

$$\overline{u_i u_i}^T = \frac{1}{T}\int_o^T u_i u_i \, dt + \frac{1}{T}\int_o^T \tilde{u}_i \tilde{u}_i \cos^2 \omega t \, dt + \frac{1}{T}\int_o^T u_i' u_i' \, dt$$

$$= \bar{u}_i \bar{u}_i + \frac{\tilde{u}_i \tilde{u}_i}{2} + \overline{u_i' u_i'} \qquad (6)$$

where T is the tidal period and the over-bar represents mean quantities over that period. If this process is applied to the equations of motion and to the kinetic energy equation a number of single, double and triple products are obtained which are either zero or can be represented in terms of the mean quantities given in equation (6).

3.3.2 Tidally-Averaged Momentum and Salt Conservation Equations

If the decomposed quantities are substituted into the momentum and salt concentration equations, and the equations averaged over a tidal cycle, the following mean property equations are obtained.

$$\frac{\partial \bar{u}_i}{\partial t} + \bar{u}_j \frac{\partial \bar{u}_i}{\partial x_j} = -\frac{1}{\rho_\infty}\frac{\partial \bar{P}}{\partial x_i} - \frac{\partial(-\overline{u_j' u_i'})}{\partial x_j} - \left[\frac{\partial(\tilde{u}_j \tilde{u}_i/2)}{\partial x_j}\right] + \nu \frac{\partial^2 \bar{u}_i}{\partial x_j \partial x_j} + \delta_{i3} g - \varepsilon_{ijk} f_j \bar{u}_k \tag{7}$$

$$\frac{\partial \bar{s}}{\partial t} + u_j \frac{\partial \bar{s}}{\partial x_j} = -\frac{\partial(\overline{u_j' s'})}{\partial x_j} - \left[\frac{\partial(\tilde{u}_j \tilde{s}/2)}{\partial x_j}\right] \tag{8}$$

where ν is the kinematic viscosity, δ_{i3} and ε_{ijk} denote the second- and third-order isotropic Cartesian tensors. The introduction of a tidal constituent has resulted in an additional term when compared with the usual equations. For the momentum equation the term in square brackets represents an additional shear stress on the fluid caused by gradients in the tidal amplitude. Pritchard (1956) suggested that a significant portion of the pressure force observed in the field data may be balanced by this term. A scale estimate of this quantity ($U^2/2L$ = 0.5×10^{-3} cm sec^{-2}) however indicates that this term is generally less than the inertial terms of the equations of motion and much less than the frictional terms. Pritchard (1954) also found that tidal velocities and tidal salinity variations were generally out of phase (i.e., $\tilde{u}_i$ cos ωt and $\tilde{s}$ sin ωt), which would reduce the term in square brackets in equation (8) to zero. Thus the tidal components are concluded to play a minor role in the momentum and salt conservation balances.

3.3.3 Tidally-Averaged Turbulent Kinetic Energy Equation

In order to examine the effect of tidal current shear on the production of turbulence, it is necessary to derive the turbulent kinetic energy equation. This can be accomplished by first subtracting the tidally-averaged turbulent momentum equation (9) from the same equation prior to temporal averaging. The remainder of the momentum equation is then multiplied by the turbulent velocity component $u_i'/2$, and the equations tidally averaged.

One new term resulting from the introduction of the fluctuating tidal component requires some interpretation. Pritchard (1956) notes that, "There may be a correlation between the root mean square velocity deviations and the tide, since the magnitude of the turbulent velocities may be directly affected by the magnitude of the tidal velocities." The tidal current changes in amplitude and sign over a tidal cycle and thus it would be expected that the turbulent shear stress generated by the tidal current shear would have a similar sinusoidal time behaviour of the form

$$\overline{u_i'u_j'} = \overline{u_i'u_j'}^{\,\text{MEAN}} + \overline{u_i'u_j'}^{\,\text{TIDE}} \cos \omega t \qquad (9)$$

Thus the above relationship becomes upon multiplication by $\tilde{u}_i \cos \omega t$ and averaging

$$\overline{\tilde{u}_i \cos\omega t \cdot u_j'u_k'}^{\,T} = \tfrac{1}{2}\, \tilde{u}_i \cdot \overline{u_j'u_k'} \qquad (10)$$

The resulting turbulent kinetic energy equation is as follows:

$$\frac{\partial(\overline{u_i'u_i'/2})}{\partial t} + \bar{u}_j \frac{\partial(\overline{u_i'u_i'/2})}{\partial x_j} + \frac{\tilde{u}_j}{2} \frac{\partial(\overline{u_i'u_i'/2})}{\partial x_j} = -(\overline{u_i' u_j'})\frac{\partial \bar{u}_i}{\partial x_j} - (\overline{u_i' u_j'})\frac{\partial \tilde{u}_i/2}{\partial x_j} + \delta_{i3}\, g(\overline{u_i'\rho'})$$

$$+ \nu \frac{\partial^2(\overline{u_i'u_i'/2})}{\partial x_j^2} - \frac{1}{\rho_\infty}\left(\overline{u_i' \frac{\partial P'}{\partial x_i}}\right) - \nu \frac{\overline{\partial u_i' \partial u_i'}}{\partial x_j \partial x_j} - \tfrac{1}{2} \frac{\partial(\overline{u_j'u_i'u_i'})}{\partial x_j} \qquad (11)$$

It should be noted that the Coriolis acceleration terms drop out, since these act only to redistribute turbulent stresses, not to generate turbulence. The first term in equation (11) represents the local rate of change of turbulent kinetic energy, while the next two terms account for advection of local turbulent kinetic energy past the point of observation. The first three terms on the right of the equals sign represent, respectively, production of turbulent kinetic energy by interaction with

$$\frac{\partial \bar{u}_i}{\partial t} + \bar{u}_j \frac{\partial \bar{u}_i}{\partial x_j} = -\frac{1}{\rho_\infty}\frac{\partial \bar{P}}{\partial x_i} - \frac{\partial(-\overline{u_j' u_i'})}{\partial x_j} - \left[\frac{\partial(\tilde{u}_j \tilde{u}_i/2)}{\partial x_j}\right] + \nu \frac{\partial^2 \bar{u}_i}{\partial x_j \partial x_j} + \delta_{i3} g - \varepsilon_{ijk} f_j \bar{u}_k \tag{7}$$

$$\frac{\partial \bar{s}}{\partial t} + u_j \frac{\partial \bar{s}}{\partial x_j} = -\frac{\partial(\overline{u_j' s'})}{\partial x_j} - \left[\frac{\partial(\tilde{u}_j \tilde{s}/2)}{\partial x_j}\right] \tag{8}$$

where ν is the kinematic viscosity, δ_{i3} and ε_{ijk} denote the second- and third-order isotropic Cartesian tensors. The introduction of a tidal constituent has resulted in an additional term when compared with the usual equations. For the momentum equation the term in square brackets represents an additional shear stress on the fluid caused by gradients in the tidal amplitude. Pritchard (1956) suggested that a significant portion of the pressure force observed in the field data may be balanced by this term. A scale estimate of this quantity ($U^2/2L$ = 0.5 x 10^{-3} cm sec^{-2}) however indicates that this term is generally less than the inertial terms of the equations of motion and much less than the frictional terms. Pritchard (1954) also found that tidal velocities and tidal salinity variations were generally out of phase (i.e., $\tilde{u}_i$ cos ωt and $\tilde{s}$ sin ωt), which would reduce the term in square brackets in equation (8) to zero. Thus the tidal components are concluded to play a minor role in the momentum and salt conservation balances.

3.3.3 Tidally-Averaged Turbulent Kinetic Energy Equation

In order to examine the effect of tidal current shear on the production of turbulence, it is necessary to derive the turbulent kinetic energy equation. This can be accomplished by first subtracting the tidally-averaged turbulent momentum equation (9) from the same equation prior to temporal averaging. The remainder of the momentum equation is then multiplied by the turbulent velocity component $u_i'/2$, and the equations tidally averaged.

One new term resulting from the introduction of the fluctuating tidal component requires some interpretation. Pritchard (1956) notes that, "There may be a correlation between the root mean square velocity deviations and the tide, since the magnitude of the turbulent velocities may be directly affected by the magnitude of the tidal velocities." The tidal current changes in amplitude and sign over a tidal cycle and thus it would be expected that the turbulent shear stress generated by the tidal current shear would have a similar sinusoidal time behaviour of the form

$$\overline{u_i'u_j'} = \overline{u_i'u_j'}^{\,\text{MEAN}} + \overline{u_i'u_j'}^{\,\text{TIDE}} \cos \omega t \qquad (9)$$

Thus the above relationship becomes upon multiplication by $\tilde{u}_i \cos \omega t$ and averaging

$$\overline{\tilde{u}_i \cos\omega t \cdot u_j'u_k'}^{\,T} = \tfrac{1}{2}\, \tilde{u}_i \cdot \overline{u_j'u_k'} \qquad (10)$$

The resulting turbulent kinetic energy equation is as follows:

$$\frac{\partial(\overline{u_i'u_i'/2})}{\partial t} + \bar{u}_j \frac{\partial(\overline{u_i'u_i'/2})}{\partial x_j} + \frac{\tilde{u}_j}{2} \frac{\partial(\overline{u_i'u_i'/2})}{\partial x_j} = -(\overline{u_i' u_j'})\frac{\partial \bar{u}_i}{\partial x_j} - (\overline{u_i' u_j'})\frac{\partial \tilde{u}_i/2}{\partial x_j} + \delta_{i3}\, g(\overline{u_i'\rho'})$$

$$+ \nu \frac{\partial^2(\overline{u_i'u_i'/2})}{\partial x_j^2} - \frac{1}{\rho_\infty}\left(\overline{u_i' \frac{\partial P'}{\partial x_i}}\right) - \nu \overline{\frac{\partial u_i' \partial u_i'}{\partial x_j \partial x_j}} - \tfrac{1}{2} \frac{\partial(\overline{u_j'u_i'u_i'})}{\partial x_j} \qquad (11)$$

It should be noted that the Coriolis acceleration terms drop out, since these act only to redistribute turbulent stresses, not to generate turbulence. The first term in equation (11) represents the local rate of change of turbulent kinetic energy, while the next two terms account for advection of local turbulent kinetic energy past the point of observation. The first three terms on the right of the equals sign represent, respectively, production of turbulent kinetic energy by interaction with

the mean velocity shear, production by the tidal velocity shear and generation by vertical buoyancy fluctuations. The next term accounts for viscous diffusion of turbulent kinetic energy. The last three terms represent, respectively, redistribution of turbulence by pressure fluctuations, viscous decay of turbulent eddies, and the transfer of turbulent kinetic energy from one part of the flow to another without any net production or loss (Lewellen 1977); these terms must be modelled to effect closure of the turbulent kinetic energy equation.

3.3.4 Gradient Richardson Number

To establish the effect of buoyancy forces on the generation or destruction of turbulent energy, it is necessary to examine the first three terms to the right of the equals sign in equation (11) in some detail. If the eddy viscosity analogy is employed for the Reynold's stresses, the following relationships result

$$\begin{aligned} (\overline{u_i'u_j'}) &= -A\frac{\partial \bar{u}_i}{\partial x_j} \\ (\overline{u_i'\rho'}) &= -K\frac{\partial \bar{\rho}}{\partial x_i} \\ (\overline{u_i'u_j'})\frac{\partial \tilde{u}_i/2}{\partial x_j} &= -A\left(\frac{\partial(\tilde{u}_i/\sqrt{2})}{\partial x_j}\right)^2 \end{aligned} \qquad (12)$$

Substituting (12) into (11) and writing out only these terms in full, we obtain

$$\text{TOTAL RATE OF CHANGE OF TURBULENT KINETIC ENERGY} = \left[A\left(\frac{\partial \bar{u}_i}{\partial x_j}\right)^2 + A\left(\frac{\partial(\tilde{u}_i/\sqrt{2})}{\partial x_j}\right)^2 - K\frac{g}{\rho_\infty}\frac{\partial \bar{\rho}}{\partial x_3}\right] + \text{REDISTRIBUTION \& DISSIPATION TERMS} \qquad (13)$$

The first term represents production of turbulence through interaction with velocity shear of the mean flow; the second accounts for similar

production brought about by horizontal and vertical shear in the tidal current amplitude; and, the last term represents destruction of the turbulence due to a stable vertical density gradient. These three terms can be combined to give a flux Richardson number (see Stewart 1959)

$$Ri_f = \left(\frac{K}{A}\right) \frac{\frac{g}{\rho_\infty}\frac{\partial \bar{\rho}}{\partial x_3}}{\left(\frac{\partial \bar{u}_i}{\partial x_j}\right)^2 + \left(\frac{\partial (\tilde{u}_i/\sqrt{2})}{\partial x_j}\right)^2} = \left(\frac{K}{A}\right) Ri_g \qquad (14)$$

From (13) it can be seen that if the flux Richardson number is greater than unity, the term in square brackets is negative and the stabilizing effect of buoyancy overpowers the shear production with a net loss in turbulent kinetic energy. Equation (14) leads to a definition for the gradient Richardson number for a mean plus tidal shear flow

$$Ri_g = \frac{\frac{g}{\rho_\infty}\frac{\partial \bar{\rho}}{\partial x_3}}{\left(\frac{\partial \bar{u}_i}{\partial x_j}\right)^2 + \left(\frac{\partial (\tilde{u}_i/\sqrt{2})}{\partial x_j}\right)^2} \qquad (15)$$

It should be noted that the gradient Richardson number involves gradients in the velocity components for both the tidal current amplitude and the mean flow. Thus when the interfacial Froude or Richardson number is defined later for horizontally two-dimensional flows using the scalar current speed, it may represent an underestimate of the gradient Richardson number.

3.4 ENTRAINMENT VERSUS DIFFUSION IN LAYERED MODELS

When vertical mixing takes place in a fluid that starts out fully stratified and ends up some considerable distance from source as well-mixed, it is necessary to distinguish between vertical entrainment and vertical diffusion. The La Grande River plume observations indicate the

surface plume (i.e., the fully stratified region) contains only enough mass to account for 12 days of discharge. Since it was shown that the surface plume was basically in equilibrium for constant discharge (Fig. 7) and that a relatively uniform discharge existed over the 2½ months of observation, a sink for surface plume water must exist. Thus the concept of downward entrainment is introduced. At the same time salt water is observed in the plume and a lateral or vertical diffusion mechanism must account for this movement of salt upstream toward the river mouth.

3.4.1 Entrainment

The transfer of mass across the interface of a layered system is generally expressed in terms of entrainment (see Keulegan, 1966). Entrainment is believed to occur through the mechanism of breaking internal waves due to a shearing flow across the interface. This is a one-way mass exchange mechanism, which, if it is out of a layer, represents a reduction in mass flow in that layer. Salt and fluid momentum are transferred to the new layer from the source layer. If we define ω_{12} as the velocity normal to the interface directed positively upward, the following relationships can be used to represent salt and momentum transport from one layer to the other.

$$u\,\omega_{12} = \left[\frac{\overline{\omega_{12} + |\omega_{12}|}}{2}\right] \cdot U_2 + \left[\frac{\overline{\omega_{12} - |\omega_{12}|}}{2}\right] \cdot U_1 \qquad (16)$$

$$s\,\omega_{12} = \left[\frac{\overline{\omega_{12} + |\omega_{12}|}}{2}\right] \cdot S_2 + \left[\frac{\overline{\omega_{12} - |\omega_{12}|}}{2}\right] \cdot S_1 \qquad (17)$$

In these relations the upper layer has subscripts '1' and the lower layer subscripts '2', of a two-layer system; the upper case quantities represent both tidally-averaged mean values with the overbars dropped and vertically-averaged layer values.

This formulation does not require a priori selection of the direction of entrainment, thus enabling testing of upward entrainment at the river mouth and downward entrainment over the remainder of the surface plume.

To define an entrainment velocity in a stratified tidal flow we follow the work of R.R. Long (1975). However it should be noted that, unlike Long's model, the principal turbulence generation mechanism is tidal flow in the lower layer, not the surface layer.

$$\omega_{12} = Ke \frac{\upsilon_{12}^3}{g \frac{\Delta\rho}{\rho_\infty} \cdot \frac{h_{01}\, h_{12}}{h_{02}}} \tag{18}$$

where υ_{12} is the relative root-mean-square velocity between the upper and lower layers, Ke is the entrainment coefficient and the other terms are as defined for the interfacial Froude number. By employing an interfacial Richardson number the above equation can be rewritten as follows

$$\omega_{12} = K_e \left(R_i^*\right)^{-\gamma} (\upsilon_1 - \upsilon_2) \tag{19}$$

$$R_i^{*-1} = \frac{\upsilon_{12}^2}{g \frac{\Delta\rho}{\rho_\infty} \cdot \frac{h_{01} h_{02}}{h_{02}}} \tag{20}$$

where γ takes on the value '1' in Long's study. To account for the possibility of upward or downward entrainment, the RMS velocities in each layer (υ_1 and υ_2) have been introduced. Thus the direction of the entrainment whether upward (+ve) or downward (-ve) is determined by the relative intensity of the turbulence in each of the layers. Long estimates a value of the coefficient Ke = 0.1 from a buoyancy (i.e., salt) balance in the upper layer. For downward entrainment this balance is difficult to do and Ke must be determined by trial-and-error such that the mass balance of the upper layer is preserved.

Since entrainment is really only applicable to the stratified region of the plume, it is necessary to have some criterion to define the lateral limits of this process outside of which the entrainment velocity is set to zero. Once again following R.R. Long (1975), we define an upper layer Froude number

$$F_1^2 = \frac{\upsilon_1^2}{g \frac{\Delta\rho}{\rho} h_{01}} \tag{21}$$

where υ_1 is the upper layer RMS current speed. Long found that the most appropriate criterion for defining the end of the entrainment region was when the upper layer Froude number approached the critical value of 1.0. In the case of the plume, F_1 is largely determined by the interface thickness and the top-to-bottom density, not the value of υ_1 which in the far-field approaches the value of the background flow.

3.4.2 Diffusion

Turbulent diffusion unlike entrainment does not result in a net change of mass between layers. Momentum or solute (salt) diffuses in the direction of a negative concentration gradient until that gradient is linear or balanced by advection, or in the case of momentum by a pressure gradient. An eddy viscosity formulation is the most common representation for horizontal Reynolds stresses. This leads to the following model:

$$\overline{u'u'} = -A_H \frac{\partial U_1}{\partial x} \quad ; \quad \overline{v'u'} = -A_H \frac{\partial U_1}{\partial y}$$

$$\overline{u'v'} = -A_H \frac{\partial V_1}{\partial x} \quad ; \quad \overline{v'v'} = -A_H \frac{\partial V_1}{\partial y} \tag{22}$$

$$\overline{u's'} = -K_H \frac{\partial S_1}{\partial x} \quad ; \quad \overline{v's'} = -K_H \frac{\partial S_1}{\partial y}$$

where the subscripts refer to the layer (similar relationships can be written for the lower layer by replacing subscript 1 by 2). As a first approximation the horizontal eddy viscosity and diffusivity coefficients (A_H & K_H) are kept constant even though their magnitude should be influenced by local changes in tidal kinetic energy. However, these horizontal coefficients are not affected by local changes in water column stability as are the vertical coefficients.

For flow in a layered system, in which properties within each fluid layer are expressed in terms of vertically-averaged quantities, diffusion of mass and momentum across the top and bottom layer surfaces must be expressed in terms of these averaged quantities. For the ice surface in the top layer, the momentum and salt Reynolds fluxes are modelled as

$$\left.\overline{w'u'}\right|_{ice} = k_i \cdot \upsilon_1 \cdot U_1$$

$$\left.\overline{w'v'}\right|_{ice} = k_i \cdot \upsilon_1 \cdot V_1 \qquad (23)$$

$$\left.\overline{w's'}\right|_{ice} = 0.0$$

where υ_1 is the root-mean-square current speed of the upper layer, and k_i is an ice friction coefficient. Note that the assumption of zero diffusive salt flux between the ice and the water has been made. For the bottom of the lower layer a similar set of relationships are used, namely

$$\left.\overline{w'u'}\right|_{bot} = k_b \cdot \upsilon_2 \cdot U_2$$

$$\left.\overline{w'v'}\right| = k_b \cdot \upsilon_2 \cdot V_2 \qquad (24)$$

$$\overline{w's'}\Big|_{bot} = 0.0$$

where υ_2 is the root-mean-square current speed of the lower layer, and k_b is bottom friction coefficient.

The specification of interfacial diffusion of mass and momentum is somewhat more complex since the diffusion coefficient is dependent on the flow situation. Karelse et al. (1974) have shown that for large values of Reynolds number and low values of interfacial Froude number no explicit relationship exists between interfacial friction coefficient and these parameters. However, they note that a variation of two times the value of the coefficient can exist for different two-layer flow situations. These situations range from a streaming upper layer, to counter flow, to streaming under layer. The turbulent momentum diffusion terms at the interface are modelled by the relations

$$\begin{aligned} w'u'\Big|_{1,2} &= k_I \cdot \upsilon_{12} \cdot (U_1 - U_2) \\ w'u'\Big|_{1,2} &= k_I \cdot \upsilon_{12} \cdot (V_1 - V_2) \end{aligned} \tag{25}$$

where υ_{12} is the relative root-mean-square velocity between the upper and lower layer.

For the vertical diffusion of salt, the diffusion coefficent should have a Richardson number dependence similar to the dependence of entrainment on Richardson number in equation (19). The stable density stratification inhibits vertical diffusion while an increased velocity shear tends to generate turbulent diffusion. Thus we define as the vertical turbulent salt flux at the interface

$$\overline{w's'}\Big|_{1,2} = k_S \cdot (R_i^*)^{-\gamma} \cdot \upsilon_{12} \cdot (S_1 - S_2) \tag{26}$$

where 'k_S' is the salt diffusion coefficient at the interface. Note that by setting $\gamma = o$, the Richardson number dependence drops out of the expression; this is convenient for testing the constant coefficient case.

3.5 TWO SIMPLIFIED MODELS

Thus far in the chapter, basic modelling considerations have been discussed and relationships for the modelling of diffusion and entrainment presented. At this point two simplified models for plume dispersion are given. An integral model to examine some of the factors affecting interface slope and an advection-diffusion model to obtain estimates of the diffusivity coefficients.

3.5.1. A Far-Field Integral Model

In a first approximation of the plume dynamics it is possible to neglect the Coriolis acceleration term. With this simplification, a one-dimensional integral model can be derived to study the role of friction and horizontal density gradient on interface adjustment. It is assumed that there is a slowly moving underlying flow U_2 in the direction of the plume $U_1(x)$. Salt flux into the plume is accomplished only by lateral ($E_y\ U_1$) and vertical ($E_z\ U_1$) entrainment, not diffusion. The thickness and width of the plume are given by $h(x)$ and $b(x)$ respectively, while H represents the uniform basin depth. Both the density of the upper layer $\rho_1(x)$ and the density of the lower layer $\rho_2(x)$ are allowed to vary in the downstream direction. The free surface elevation is given by $\eta(x)$.

Integrating the continuity equation over the plume cross-sectional area, using Leibniz's rule for integration of a partial derivative

$$\int_{b/2}^{b/2} \int_{-h}^{o} \left(\frac{\partial u}{\partial x} + \frac{\partial v}{\partial y} \frac{\partial w}{\partial z} \right) dz \cdot dy = 0 \qquad (27)$$

we obtain

$$\frac{d(bhU_1)}{dx} = 2E_y hU_1 + E_z bU_1 \qquad (28)$$

Similarly, if we integrate the x-momentum equation in the upper layer, neglecting the longitudinal shear stress,

$$\int_{-b/2}^{b/2}\int_{-h}^{o}\left(\frac{\partial u^2}{\partial x}+\frac{\partial vu}{\partial y}+\frac{\partial wu}{\partial z}+\frac{1}{\rho_\infty}\frac{\partial P}{\partial x}+\frac{\partial \tau_{xy}}{\partial y}+\frac{\partial \tau_{xz}}{\partial z}\right)dz\cdot dy=0 \tag{29}$$

we obtain (30)

$$\frac{d(hbU_1^2)}{dx}-2E_y hU_1^2-E_z bU_1^2=-\frac{gbh}{\rho_\infty}\left[\frac{h}{2}\frac{d\rho_1}{dx}+\rho_1\frac{d\eta}{dx}\right]-2h\tau_{xb}-b\left[\alpha_i U_1+\alpha_I(U_1-U_2)\right]$$

where τ_{xb} is the lateral shear stress on the plume, and α_i and α_I are linear friction coefficients for the ice and interface surfaces, respectively. Now, if we vertically integrate the lower layer x-momentum equation, neglecting lateral shear stress, and inertial terms

$$\int_{-H}^{-h}\left(\frac{1}{\rho_\infty}\frac{\partial P}{\partial x}+\frac{\partial \tau_{xz}}{\partial z}\right)dz=0 \tag{31}$$

we obtain the following relationships for surface pressure ($g'=g\Delta\rho/\rho_\infty$)

$$-\frac{gh}{\rho_\infty}\rho_1\frac{d\eta}{dx}=\left(\frac{h}{H}\right)\left[\alpha_B U_2+\alpha_I(U_2-U_1)\right]+\frac{gh^2}{\rho_\infty}\frac{d\rho_1}{dx}-\frac{gh}{\rho_\infty}\Delta\rho\frac{dh}{dx}+g\frac{H'h'}{2\rho_\infty}\frac{d\rho_2}{dx} \tag{32}$$

combining equation (32) with (30), the surface pressure gradient can be eliminated to yield

$$\frac{d(hbU_1^2)}{dx}=2hE_y U_1^2+bE_z U_1^2-2h\tau_{xb}-b\left[\alpha_i U_1+\alpha_I(U_1-U_2)\right]+\left(\frac{bh}{H}\right)\left[\alpha_B U_2+\alpha_I(U_2-U_1)\right]$$

$$+\frac{ghb}{\rho_\infty}\left[\frac{h}{2}\frac{d\rho_1}{dx}+\frac{H}{2}\frac{d\rho_2}{dx}\right]-bhg'\frac{dh}{dx} \tag{33}$$

Since h/H<<1 the lower layer stress terms can be dropped. Now, combining equation (28) and (33), the following equation is obtained for the rate of change of the plume thickness with distance away from the plume discharge

$$\frac{dh}{dx} = \frac{F_b^2 \frac{db}{dx} - 2F_b^2 E_y - F_L^2 E_z - \frac{2}{g'b}\tau_{xb} - \frac{\alpha_i U_1 + \alpha_I (U_1 - U_2)}{g'h} + \frac{1}{\Delta\rho}\left[\frac{h}{2}\frac{d\rho_1}{dx} + \frac{H}{2}\frac{d\rho_2}{dx}\right]}{\left(1 - F_L^2\right)}$$

where $F_L^2 = \frac{U_1^2}{g'h}$ and $F_b^2 = \frac{U_1^2}{g'b}$ (34)

The first thing to note in the above equation is that the slope of the interface depends critically on the value of the local densimetric Froude number F_L^2. As F_L^2 approaches unity from either direction a singularity occurs and the interface slope becomes infinite. This is similar to the case of an internal hydraulic jump where flow over a sill causes a change from subcritical to supercritical flow. As the densimetric Froude numbers in the plume are generally subcritical, except perhaps at the seaward extremity of the plume, then the numerator is a positive quantity. Thus for the case of subcritical plume flow we see that both momentum entrainment and friction cause the interface to thin, while the density gradient in the surface layer and lateral spreading tend to counteract this effect.

To complete the integral model the v-momentum equation and the conservation of salt equations must be similarly integrated. Integrating v-momentum, and retaining only the vertical shear stress,

$$\int_{-b/2}^{b/2} \int_{-h}^{o} \left(\frac{\partial uv}{\partial x} + \frac{\partial vv}{\partial y} + \frac{\partial wv}{\partial z} + \frac{1}{\rho_\infty}\frac{\partial P}{\partial y} + \frac{\partial \tau_{yz}}{\partial z}\right) dz \cdot dy \qquad (35)$$

we obtain

$$\frac{d(hbU_1V_1)}{dx} = 2hE_yU_1V_1 + bE_zU_1V_1 - g'h - g\rho_1\eta_y - b\left[\alpha_i V_1 + \alpha_I(V_1 - V_2)\right] \qquad (36)$$

Integrating the conservation of salt equation over the plume cross-section

$$\int_{-b/2}^{b/2} \int_{o}^{h} \left(\frac{\partial(us)}{\partial x} + \frac{\partial(vs)}{\partial y} + \frac{\partial(ws)}{\partial z} \right) dz\, dy = 0 \qquad (37)$$

yields

$$\frac{d(hbU_1 S_1)}{dx} = 2hE_y S_2\, U_1 + bE_z\, S_2\, U_1 \qquad (38)$$

Density (ρ_1, ρ_2) is taken as a linear function of salinity. The cross-plume slope (η_y = negative slope) is chosen to just about balance the cross-plume density gradient such that the desired spreading rate is achieved.

Numerical integration of equations (28), (34), (36), and (38), using a fourth order Runge - Kutka technique permits an initial estimate to be made of the model parameters under the 1980 La Grande discharge condition of 1,600 $m^3\ sec^{-1}$. The coefficients used in this analysis are the following

$$\alpha_1 = 0.0\ ;\ \alpha_I = 0.0022\ U_1 \quad (cm\ sec^{-1})\ ;\ U_2 = 0.0$$

$$E_y = 0.2\ ;\ E_z = -0.00002\ ;\ \rho_2 = 1.022 \text{ (a constant)}$$

$$U_R = 17.8\ cm\ sec^{-1}\ ;\ b_R = 3\ km\ ;\ h_R = 3\ m\ ;\ \Delta x = 10m$$

It should be noted that vertical entrainment is specified as a negative value (i.e., downward out of the plume); this must be slightly positively balanced by lateral entrainment to bring salt into the plume. The 10^5 ratio of E_y to E_z is of the same order as horizontal to vertical diffusion coefficients. As can be seen in Fig. 22 the density (σ_T) rapidly increases over the first 10 km but never quite reaches the background level. This results from the need to balance laterally inflowing saline water with outward and downward flowing brackish water. The plume thickness shows a slight increase off the river mouth but then gradually

decreases in the downstream direction until the local Froude number (F_L) approaches its critical value of 1.0. In this region the plume velocity rapidly increases and the thickness rapidly decreases, representing the end of the stable region of the plume. Throughout the length of the plume the lateral spread is basically linear. It should be noted that both the rate of spread and the location of the critical Froude number are strongly dependent on the value assigned to the friction coefficient.

3.5.2 A Far-Field Analytical Model

The advection-diffusion equation for salinity can be solved analytically, for the case of a constant freshwater source discharging into a uniform flow field U_s. This permits the roles of horizontal and vertical mixing on plume dispersion in the far-field to be examined. In this case $b_s \cdot h_s \cdot U_s$ is an area source. It can be determined by joining to an integral near-field model, or as in the case presented here, by fitting the resulting salinity field to observations. The advection diffusion equation solved in this analysis is,

$$U_s \frac{\partial s}{\partial x} = K_H(x) \frac{\partial^2 s}{\partial y^2} + K_V(x) \frac{\partial^2 s}{\partial z^2} \tag{39}$$

Following Csanady (1973) we assume that a number of point sources are located over the source area. For boundary conditions, it is assumed that there is zero salt flux through the ice-water interface, while the lateral and bottom boundaries are kept at constant background levels. Then integrating the point-source solutions of the form

$$S = \frac{S_s}{\sigma_y \sigma_z} e^{-\frac{y^2}{\sigma_y^2} - \frac{z^2}{\sigma_z^2}} \tag{40}$$

over the area of the source region as follows

$$S = \frac{S_s}{\pi \sigma_y \sigma_z} \int_{-b_s/2}^{b_s/2} e^{-\left(\frac{y-y'}{\sigma_y}\right)^2} dy' \int_{-h_s}^{0} \left(e^{-\left(\frac{z+z'}{\sigma_z}\right)^2} + e^{-\left(\frac{z-z'}{\sigma_z}\right)^2} \right) dz' \tag{41}$$

we obtain

$$S = \frac{S_s}{4}\left[\operatorname{erf}\left(\frac{h_s + z}{\sigma_z}\right) + \operatorname{erf}\left(\frac{h_s - z}{\sigma_z}\right)\right]\left[\operatorname{erf}\left(\frac{b_s/2 + y}{\sigma_y}\right) + \operatorname{erf}\left(\frac{b_s/2 - y}{\sigma_y}\right)\right] \qquad (42)$$

where

$$\frac{d\sigma_y^2}{dx} = \frac{4K_H(x)}{U_s} \qquad \frac{d\sigma_z^2}{dx} = \frac{4K_V(x)}{U_s}$$

The relationship for K_V following Munk and Anderson (1947), is adopted

$$K_V(x) = \tilde{K}_V \left(1 + 3.33\, R_i^*(x)\right)^{-3/2}$$

$$K_H(x) = \tilde{K}_H \qquad (43)$$

$$R_i^*(x) = U^2/\left(gh_o\, .000801\, (S(x) - S_o)\right) \qquad (44)$$

Using equations (42) to (44), the three-dimensional salinity field was determined for different values of K_V and K_H until the computed salinity field best fitted the observed 1976 data (see Fig. 1). These values are given below

$$\tilde{K}_V = 50 \text{ cm}^2 \text{ sec}^{-1} \quad ; \quad \tilde{K}_H = 7 \times 10^5 \text{ cm sec}^{-1}$$

Horizontal and vertical sections of the analytical model results are given in Fig. 23 for the 1976 discharge conditions ($Q_o = 450$ m^3 sec^{-1}). The horizontal distribution of salinity predicted by the model is in good agreement with the field observations of Peck (1976). Also, the Richardson number inhibition of vertical mixing seems to work well; the prediction shows the plume to spread out essentially as a layer and only in the far-field, where the vertical density gradient is substantially less, does it mix downward. The analytical model thus points out the importance of both horizontal and vertical mixing and the density effects upon the latter.

4. A TWO-LAYER NUMERICAL MODEL

4.1 MODEL DERIVATION

The integral model reported in the previous chapter predicted to a good first approximation the fully stratified region of the plume. The model, however, has several shortcomings. First, it was unable to resolve the horizontal two-dimensionality of the flow field in and around the plume, in particular the plume bending and attachment to the landward boundary. In addition the lateral spreading rate of the plume had to be specified a priori by assuming a cross-stream free-surface slope. No underlying basin flow could be introduced and thus the ice and interface friction could not be properly described. In the analytical advection-diffusion model there was no mechanism to feed the density field back into a momentum equation to alter the flow field. Coriolis accelerations were not taken into account in either of these models. Thus, in order to redress these shortcomings and better represent the horizontal motion and dilution fields a two-layer numerical model has been developed.

Figure 24 gives the plan and elevation views of the coordinate system employed in the derivation of the vertically-averaged equations. The z-axis is directed upward along the local zenith, while the y-axis and thus the v velocity component points approximately toward the west. The x-axis and the u velocity component are directed toward the north. The exact orientation of the horizontal axis with respect to true north is determined by the orientation of the landward boundary as depicted in Fig. 8. It should be noted that the velocity components in this coordinate system have been rotated counter-clockwise 90° from those given in the observations of Chapter 2. The use of a lower reference level simplifies the vertical integration. The heavy dashed line in Fig. 24 represents the pycnocline with the layer thicknesses given by

1) Upper Layer: $h_{01} = h_0 - h_1$
2) Lower Layer: $h_{12} = h_1 - h_2$

Velocity, salinity and thus density are allowed to vary in the x and y directions in each layer as determined by the solution of the vertically integrated momentum, mass and salt conservation equations. However, uniform vertical profiles of these properties need not be specified for an individual layer. For example, it may be physically more realistic to specify an exponential variation of salinity with depth in the lower layer, more in keeping with station 132 data in Fig. 10, than a uniform sub-pycnocline salinity profile. This can be accomplished by substituting a z-dependent function for salinity that satisfies the top and bottom boundary conditions and then analytically integrating this expression for the mean value of salinity, density and thus pressure over the layer thickness. In the present work, however, uniform values of all properties are assumed in each layer, as a first step in the modelling of plume dynamics.

Some basic approximations have been introduced to simplify the model derivations. First, the tidally-averaged equations of motion are used with the background flow and river discharge assumed constant. As pointed out earlier the Bousinesq and hydrostatic approximations are applied to all regions of the flow field. The fluid is assumed to be incompressible with density linearly dependent on salinity only (see Fig. 11 for justification of this assumption). The vertical Coriolis acceleration term is neglected as are latitudinal variations in the Coriolis parameter 'f'. Direct forcing by surface wind stress or atmospheric pressure gradient is ignored; however, the indirect effect of this external forcing can be incorporated by adjusting the background flow. The Ekman layers under the ice and at the bottom boundary are neglected in this initial treatment of plume dynamics.

4.1.1 Vertical Integration of the Pressure Gradient Term

For the vertical integrations to follow, Leibniz's rule for integration of a partial derivative with variable limits of integration, will be employed:

$$\int_{h_1(x)}^{h_0(x)} \left(\frac{\partial u(x,z)}{\partial x}\right) dz = \frac{\partial}{\partial x}\left(\int_{h_1}^{h_0} u(x,z)\, dz\right) - u(x,h_0)\,\frac{\partial h_0}{\partial x} + u(x,h_1)\,\frac{\partial h_1}{\partial x} \quad (45)$$

Using the hydrostatic equation, the vertical pressure distribution in the upper layer is obtained

$$P_1(x,y,z) = P_a + g\,\rho_1(x,y)\left[h_0(x,y) - z\right] \tag{46}$$

Then, vertically integrating the x-directed pressure gradient

$$PGx_1 = -\frac{1}{\rho_\infty}\int_{h_1}^{h_0}\left(\frac{\partial P_1(x,y,z)}{\partial x}\right) dz = -\frac{1}{\rho_\infty}\left[\frac{\partial\left(\int_{h_1}^{h_0} P_1\,dz\right)}{\partial x} - P_1(h_0)\frac{\partial h_0}{\partial x} + P_1(h_1)\frac{\partial h_1}{\partial x}\right]$$

we obtain the following expression

$$PGx_1 = -\frac{gh_{01}}{\rho_\infty}\left[\rho_1\frac{\partial h_0}{\partial x} + \frac{h_{01}}{2}\frac{\partial \rho_1}{\partial x}\right] \tag{47}$$

As we have assumed that the atmospheric pressure P_a is horizontally uniform, it drops out of the pressure gradient calculation. An expression analogous to (46) can be derived for the y-directed pressure gradient.

In the lower layer the expression for the pressure gradient is slightly more complicated, but can be derived in the same manner as above. The vertical distribution of pressure in the lower layer is once again obtained from the hydrostatic relationship

$$P_2(x,y,z) = P_a + g\rho_1(x,y)\left[h_0(x,y)-h_1(x,y)\right] + g\rho_2(x,y)\left[h_1(x,y) - z\right] \tag{48}$$

Then vertically integrating the x-directed pressure gradient over the lower layer, yields

$$PGx_2 = -g\frac{h_{12}}{\rho_\infty}\left[\rho_1\frac{\partial h_0}{\partial x} + h_{01}\frac{\partial \rho_1}{\partial x} + \rho_{21}\frac{\partial h_1}{\partial x} + \frac{h_{12}}{2}\frac{\partial \rho_2}{\partial x}\right] \tag{49}$$

there $\rho_{21} = (\rho_2 - \rho_1)$ represents the local difference in density between the top and bottom layers. The first two terms basically represent a transmission of the pressure gradient driving the flow in the surface layer, while the third term represents the interface adjustment necessary to drive flow in the bottom layer. A similar expression can also be derived for the y-directed pressure gradient.

If the right-hand side of equation (49) is set to zero, using the quasi-compensation assumption of Welander (1968), then the expression for the free surface gradient, $\partial h_0/\partial x$, could be substituted into equation (47). This would result in the direct coupling of interface displacements and upper layer pressure gradient. However, it is uncertain a priori whether the shallow basin in James Bay lends itself to the quasi-compensation assumption and thus this manipulation is not made. An alternate approach would be to define a new pressure variable,much the same as that introduced by Welander (1966) and Stronach (1978), which combines the free surface and interface gradients and is substituted into equation (47). While this enables direct adjustment of the interface in the solution of the upper layer momentum equation it still requires iteration with the lower layer equation to obtain an appropriate value for the new pressure variable. Thus it was decided to retain the pressure gradients in their original form as given by equations (47) and (49).

4.1.2 Vertical Integration of the Momentum Equations

The integration of the advection terms over the upper layer can be used to demonstrate the general procedure for integration of the momentum equations. Carrying out the integration on the conservative form of the advection terms

$$\int_{h_1}^{h_0} \left(\frac{\partial(uu)}{\partial x} + \frac{\partial(vu)}{\partial y} + \frac{\partial(wu)}{\partial z} \right) dz \qquad (50)$$

we obtain

$$\frac{\partial\left(\int_{h_1}^{h_0} uu\, dz\right)}{\partial x} - (uu)_{h_0}\frac{\partial h_0}{\partial x} + (uu)_{h_1}\frac{\partial h_1}{\partial x} + \frac{\partial\left(\int_{h_1}^{h_0} uvdz\right)}{\partial y} - (uv)_{h_0}\frac{\partial h_0}{\partial y}$$

$$+ (uv)_{h_1}\frac{\partial h_1}{\partial y} + (wu)_{h_0} - (wu)_{h_1} \qquad (51)$$

But the vertical velocities at the interfaces have the following kinematic relationship

$$w_{h_0} = u_{h_0}\frac{\partial h_0}{\partial x} + v_{h_0}\frac{\partial h_0}{\partial y} + \omega_{01}$$

$$w_{h_1} = u_{h_1}\frac{\partial h_1}{\partial x} + v_{h_1}\frac{\partial h_1}{\partial y} + \omega_{12} \qquad (52)$$

where ω_{01} is the entrainment velocity across the ice-water interface and ω_{12} the entrainment between the bottom layer and the top layer. Substituting (52) into (51), and noting that no entrainment is allowed across the ice-water interface, we obtain the following expression for the vertically-integrated advection terms:

$$\frac{\partial\left(\int_{h_1}^{h_0} uudz\right)}{\partial x} + \frac{\partial\left(\int_{h_1}^{h_0} uvdz\right)}{\partial y} - u\omega_{12} \qquad (53)$$

Since all parameters are uniform over the layer thickness we can rewrite equation (53) as follows

$$\frac{\partial(h_{01}U_1U_1)}{\partial x} + \frac{\partial(h_{01}V_1U_1)}{\partial y} - u\omega_{12} \qquad (54)$$

where U_1 and V_1 are the average horizontal velocity components in the upper layer. The expression $u\omega_{12}$ represents, when positive, the upward entrainment of u-momentum from the lower layer.

If the same procedures are applied to the other terms, the vertically-integrated u- and v-momentum equations for the upper layer are

$$\frac{\partial(h_{01}U_1U_1)}{\partial x}+\frac{\partial(h_{01}V_1U_1)}{\partial y}-u\omega_{12}=PGx_1+h_{01}\left[\frac{\partial}{\partial x}\left(A_H\frac{\partial U_1}{\partial x}\right)+\frac{\partial}{\partial y}\left(A_H\frac{\partial U_1}{\partial y}\right)\right]$$

$$-\alpha_i U_1+\alpha_I(U_2-U_1)+f\,h_{01}V_1 \qquad (55)$$

$$\frac{\partial(h_{01}U_1V_1)}{\partial x}+\frac{\partial(h_{01}V_1V_1)}{\partial y}-v\omega_{12}=PGy_1+h_{01}\left[\frac{\partial}{\partial x}\left(A_H\frac{\partial V_1}{\partial x}\right)+\frac{\partial}{\partial y}\left(A_H\frac{\partial V_1}{\partial y}\right)\right]$$

$$-\alpha_i V_1+\alpha_I(V_2-V_1)-f\,h_{01}U_1 \qquad (56)$$

where α_i and α_I are the ice and interfacial friction coefficients, respectively. They represent the first two terms in equations (23) and (25). Performing a similar integration for the lower layer between the limits $z = h_2$ and $z = h_1$, yields

$$\frac{\partial(h_{12}U_2U_2)}{\partial x}+\frac{\partial(h_{12}V_2U_2)}{\partial y}+u\omega_{12}=PGx_2+h_{12}\left[\frac{\partial}{\partial x}\left(A_H\frac{\partial U_2}{\partial x}\right)+\frac{\partial}{\partial y}\left(A_H\frac{\partial U_2}{\partial y}\right)\right]$$

$$-\alpha_b U_2-\alpha_I(U_2-U_1)+f\,h_{12}V_2 \qquad (57)$$

$$\frac{\partial(h_{12}U_2V_2)}{\partial x}+\frac{\partial(h_{12}V_2V_2)}{\partial y}+v\omega_{12}=PGy_2+h_{12}\left[\frac{\partial}{\partial x}\left(A_H\frac{\partial V_2}{\partial x}\right)+\frac{\partial}{\partial y}\left(A_H\frac{\partial V_2}{\partial y}\right)\right]$$

$$-\alpha_b V_2-\alpha_I(V_2-V_1)-f\,h_{12}U_2 \qquad (58)$$

where h_{12} is the lower layer thickness, and U_2, V_2, represent the average horizontal velocities for the lower layer.

4.1.3 Conservation of Mass and Salt

The continuity equation and the equation for salt conservation can both be readily integrated over each layer, in a manner similar to the momentum equations. The upper and lower layer continuity equations become, upon integration,

$$\frac{\partial(h_{01}U_1)}{\partial x} + \frac{\partial(h_{01}V_1)}{\partial y} - \omega_{12} = 0 \tag{59}$$

$$\frac{\partial(h_{12}U_2)}{\partial x} + \frac{\partial(h_{12}V_2)}{\partial y} + \omega_{12} = 0 \tag{60}$$

It should be noted that when the entrainment velocity ω_{12} is positive it takes mass from the bottom layer and adds it to the top layer, thus the change in sign in the expressions for the upper and lower layers.

Vertically integrating the advection-diffusion equation for salinity, we obtain the following equations for the upper and lower layers.

$$\frac{\partial(h_{01}U_1S_1)}{\partial x} + \frac{\partial(h_{01}V_1S_1)}{\partial y} - s\omega_{12} = h_{01}\left[\frac{\partial}{\partial x}\left(K_H\frac{\partial S_1}{\partial x}\right) + \frac{\partial}{\partial y}\left(K_H\frac{\partial S_1}{\partial y}\right)\right] + \kappa(S_2-S_1) \tag{61}$$

$$\frac{\partial(h_{12}U_2S_2)}{\partial x} + \frac{\partial(h_{12}V_2S_2)}{\partial y} + s\omega_{12} = h_{12}\left[\frac{\partial}{\partial x}\left(K_H\frac{\partial S_2}{\partial x}\right) + \frac{\partial}{\partial y}\left(K_H\frac{\partial S_2}{\partial y}\right)\right] - \kappa(S_2-S_1) \tag{62}$$

where κ equals the interface diffusion coefficient corresponding to the first three terms in equation (26). It should be noted that horizontal diffusion is multiplied by the layer thickness and thus its role should decrease as the layer thins out.

4.1.4 Boundary Conditions

The application of a mathematical model to the dispersion of river water entering such a large basin as James Bay involves either the

specification of a very large solution region (i.e., all of James Bay and Hudson Bay) and simple boundary conditions, or the selection of a more localized region with the inherent difficulty of specifying boundary conditions on three open boundaries. In order to maximize the model resolution around the river mouth and still carry out a number of test runs, the latter approach is adopted in this study. It is assumed that the open boundaries are sufficiently far away from the surface plume that they will have little effect upon it. The effectiveness of this approximation can be judged by careful examination of predicted model parameters near these boundaries.

The conditions specified for the single closed boundary, the shoreline, (y=0) are quite straightforward. First, the velocity normal to the shore is set to zero except at the river entrance where the mass flow rate is specified. This is represented as follows

$$V_1\Big|_{y=0,Y} = 0$$

$$V_2\Big|_{y=0,Y} = 0 \tag{63}$$

$$V_1\Big|_{river} = Q_0/(h_{01}\,\Delta x) \tag{64}$$

Note that the river does not discharge into the bottom layer. A free-slip condition is used to minimize lateral transfer of momentum into the system and is represented as follows

$$\frac{\partial U_1}{\partial y}\Big|_{y=0,Y} = \frac{\partial U_2}{\partial y}\Big|_{y=0,Y} = 0 \tag{65}$$

A similar condition is employed for salt, i.e., zero salt flux

$$\frac{\partial S_1}{\partial y}\Big|_{y=0} = \frac{\partial S_2}{\partial y}\Big|_{y=0} = 0 \tag{66}$$

On the seaward boundary that is opposite but parallel to the shoreline (y=Y), the specification of the cross-boundary velocity is not as straightforward. For the purpose of this study it is assumed that this seaward boundary lies within the shore parallel, northward flowing, coastal current of James Bay, but far enough offshore not to be influenced by the river momentum. This necessitates that the flow remains shore parallel along the boundary and thus a zero normal velocity boundary condition given by equation (63) is employed. It is also assumed that there is zero flux of momentum at this seaward boundary as given by relationship (65). Salinity at this location acts as a source for lateral diffusion and is thus specified at a value representative of observations taken there. However, it is always specified 2 to 3°/oo smaller than the bottom salinity at the same location for two reasons: 1) this top-to-bottom salinity difference is observed in the actual field data, and 2) a density contrast is necessary to the two-layer formulation. Thus we have the following Dirichelet condition on salinity

$$S_1\Big|_{y=Y} = S_1(x)$$

$$S_2\Big|_{y=Y} = S_2(x) \qquad (67)$$

and $S_2(x)-S_1(x)$ must be greater than some δS.

At the cross-flow upstream boundary (x=0), a shore parallel flow field is specified in both the upper and lower layers. However, rather than impose the rigid condition of absolutely no y-directed flow at this boundary we rather use the free-slip condition given in equation (69). Then if a V velocity is created along this boundary we know that the upstream boundary is not far enough removed from the river mouth. The velocity boundary conditions, are the Dirichelet condition

$$U_1\Big|_{x=0} = U_1(y)$$

$$U_2\Big|_{x=0} = U_2(y) \tag{68}$$

and the Neumann condition

$$\frac{\partial V_1}{\partial x}\Big|_{x=0} = \frac{\partial V_2}{\partial x}\Big|_{x=0} = 0 \tag{69}$$

The boundary condition on salinity must be a specified function, as this salt is advected downstream by the background flow in both layers. The Dirichelet condition is then

$$S_1\Big|_{x=0} = S_1(y)$$

$$S_2\Big|_{x=0} = S_2(y) \tag{70}$$

where $S_2(x)-S_1(x)$ must be greater than some δS.

Lastly, the downstream or outflow boundary (x=X) must insure that there is no mass build-up in the system. Thus, a zero mass flux condition is required at the downstream end of the solution region, providing a boundary condition on pressure

$$\frac{\partial(h_{01}U_1)}{\partial x}\Big|_{x=X} = \frac{\partial(h_{12}U_2)}{\partial x}\Big|_{x=X} = 0 \tag{71}$$

A zero normal velocity gradient and zero normal salt gradient boundary condition prevent momentum and salt flux through this boundary

$$\frac{\partial S_1}{\partial x}\Big|_{x=X} = \frac{\partial S_2}{\partial x}\Big|_{x=X} = 0 \; ; \; \frac{\partial U_1}{\partial x}\Big|_{x=X} = \frac{\partial U_2}{\partial x}\Big|_{x=X} = 0 \tag{72}$$

A free-slip condition on the V velocity insures that there is no momentum introduced at the downstream boundary and thus requires the following Neumann condition

$$\frac{\partial V_1}{\partial x}\bigg|_{x=X} = \frac{\partial V_2}{\partial x}\bigg|_{x=X} = 0 \qquad (73)$$

While the above relationships are the basic conditions applied at the boundaries of the solution region, considerable flexibility in testing alternate conditions has been retained in the finite-difference formulation of these boundary conditions.

4.2 FINITE DIFFERENCE FORMULATION

The traditional approach to the numerical solution of the equations governing geophysical fluid dynamics problems has been to temporally integrate the time-dependent equations out to steady state; see Freeman et al. (1972), Stronach (1978) and Simons (1980). Because the time-step is limited by numerical stability, thousands of time steps are often required to reach steady-state. Stronach with a time step of 120 seconds required upwards of 3000 time steps to reach a steady state. Thus it was decided at the outset that a more quickly converging scheme was required to provide the parameter testing capability indicated by the data analysis.

The flexible finite-difference formulation developed by Raithby and Torrance (1974) was chosen. This scheme was developed for use with the system of elliptic equations normally encountered in problems involving heat, mass, and momentum transfer, and thus had to be extended to geophysical fluid problems by incorporating the Coriolis force term. The essence of the technique is in the differencing of the advection and diffusion terms so as to extend their numerical stability for larger and non-uniform time steps. This involves the use of upstream-weighted difference schemes, with weighting factors just sufficient to achieve numerical stability.

A second major divergence from the traditional numerical solution of geophysical fluid dynamics problems is the handling of the coupling between the momentum and mass conservation equations. For the vertically integrated equations this is normally accomplished by solving for interface displacement from the time-dependent form of the continuity equation and then substituting this value into the pressure gradient term of the momentum equations; this procedure often leads to slow convergence in iterative solution techniques. Raithby and Schneider (1979) have evaluated various techniques for improving this pressure - velocity coupling and along with other more advanced methods have recommended an implicit transient technique which insures that a consistent time step is used both to correct the velocity and to update the pressure field.

Thus the numerical modelling effort in this study not only involves finding a solution to the two-layer system of differential equations, but at the same time attempts to improve on convergence of the finite-difference solution over traditional geophysical fluid modelling techniques.

4.2.1 Finite-Difference Equations

The staggered grid used by Raithby and Schneider (1979) was adopted in the present study. Figure 25 shows the storage locations for the dependent variables in the x-y plane. Although the finite-difference approximations are derived for the uniform grid shown in the figure, their extension to the non-uniform grid of Raithby and Torrance (1974) is quite straightforward. The control volume for the U-momentum equation at the point of interest 'P' is delineated by a solid line in the figure. The 'P' control volume for mass and salt conservation is half grid point to the west, while the 'P' control volume for V-momentum is half grid point to the west and half grid point to the north. The compass points (e.g., 'N' for north) are used to designate the grid point parameters in the immediate vicinity of the point of interest 'P' and not, at this point, geographical coordinates. It should be noted that the dash-dot line indicates the location of the U_P, V_P, and S_P

(h_p and ρ_p) parameters associated with the point 'P'. The principal advantage of the staggered grid is that pressure and velocity variables are strongly coupled.

The detailed derivation of the finite-difference equations will be given only for the U_1-momentum equation. However, it is first useful to rewrite the partial differential equation for U_1-momentum in a slightly more condensed form than given by equation (55)

$$-\left[\frac{\overset{+}{\omega}_{12}U_2}{h_{01}} + \frac{\overset{-}{\omega}_{12}U_1}{h_{01}}\right] = AD_{U1} - \frac{\alpha_1 U_1}{h_{01}} + \frac{\alpha_I (U_2-U_1)}{h_{01}} + \overset{*}{S}_{U1} \qquad (74)$$

where the entrainment velocities are defined as follows

$$\overset{+}{\omega}_{12} = (\omega_{12} + |\omega_{12}|)/2 \; ; \; \overset{-}{\omega}_{12} = (\omega_{12} - |\omega_{12}|)/2 \qquad (75)$$

The advection and diffusion terms are combined in the single expression

$$AD_{U1} = -\frac{1}{h_{01}}\left[\frac{\partial(h_{01}U_1U_1)}{\partial x} + \frac{\partial(h_{01}V_1U_1)}{\partial y}\right] + \left[\frac{\partial}{\partial x}\left(A_H \frac{\partial U_1}{\partial x}\right) + \frac{\partial}{\partial y}\left(A_H \frac{\partial U_1}{\partial y}\right)\right] \qquad (76)$$

and the pressure gradient and the Coriolis term are collected together in the source term

$$\overset{*}{S}_{U1} = -\frac{g}{\rho_\infty}\left(h_{01}\frac{\partial \rho_1}{\partial x} + \rho_1 \frac{\partial h_0}{\partial x}\right) + fV_1 \qquad (77)$$

The finite-difference representation of the advection-diffusion terms is the most complex and will thus be derived first. Following Raithby and Torrance (1974) we define the value of the dependent

variable U_1 at each of the x-directed faces of the U_1-momentum control volume

$$U_1/_{face\ E} = (\tfrac{1}{2} - \beta_E)U_{1E} + (\tfrac{1}{2} + \beta_E)U_{1P} \; ; \; U_1/_{face\ P} = (\tfrac{1}{2} - \beta_W)U_{1P} + (\tfrac{1}{2} + \beta_W)U_{1W}$$

$$U_1/_{face\ N} = (\tfrac{1}{2} - \beta_N)U_{1N} + (\tfrac{1}{2} + \beta_N)U_{1P} \; ; \; U_1/_{face\ S} = (\tfrac{1}{2} - \beta_S)U_{1P} + (\tfrac{1}{2} + \beta_S)U_{1S} \tag{78}$$

Introduction of the free parameter β enables run-time modification of the differencing scheme, ranging from central to upstream differences. The advective mass flux is taken as a simple two-point average from adjacent grid points, as follows

$$HU_{1E} = (h_{01EEE}U_{1E} + h_{01PE}U_{1P})/2 \; ; \; HU_{1W} = (h_{01PE}U_{1P} + h_{01PW}U_{1W})/2$$

$$HV_{1N} = (h_{01PN}V_{1P} + h_{01ENE}V_{1E})/2 \; ; \; HV_{1S} = (h_{01PS}V_{1S} + h_{01ESE}V_{1SE})/2 \tag{79}$$

where the layer thicknesses are simple averages such as

$$h_{01EEE} = (h_{01E} + h_{01EE})/2 \; ; \; H_{01PE} = (h_{01P} + h_{01E})/2 \tag{80}$$

Substituting equations (78) and (79) into the horizontal advection-diffusion terms, we obtain

$$AD_{U1} = -\frac{1}{h_{01PE}}\left[\frac{HU_{1E}\left((\tfrac{1}{2}-\beta_E)U_{1E}+(\tfrac{1}{2}+\beta_W)U_{1P}\right) - HU_{1W}\left((\tfrac{1}{2}-\beta_W)U_{1P}+(\tfrac{1}{2}+\beta_W)U_{1W}\right)}{\delta x}\right.$$

$$\left. + \frac{HV_{1N}\left((\tfrac{1}{2}-\beta_N)U_{1N} + (\tfrac{1}{2}+\beta_N)U_{1P}\right) - HV_{1S}\left((\tfrac{1}{2}-\beta_S)U_{1P}+(\tfrac{1}{2}+\beta_S)U_{1S}\right)}{\delta y}\right]$$

$$+ \left[\frac{A_H(U_{1E}-U_{1P})/\delta x - A_H(U_{1P}-U_{1W})/\delta x}{\delta x} + \frac{A_H(U_{1N}-U_{1P})/\delta y - A_H(U_{1P}-U_{1S})/\delta y}{\delta y}\right] \tag{81}$$

If we multiply U_{1P}/h_{01PE} times the conservation of mass equation for the momentum cell

$$U_{1P}\frac{(HU_{1E}-HU_{1P})}{h_{01PE}\delta x}+U_{1P}\frac{(HV_{1N}-HV_{1S})}{h_{01PE}\delta y}-U_{1P}\frac{\omega_{12PE}}{h_{01PE}}=0 \tag{82}$$

and then add it to the equation (81), we obtain after some rearrangement, the final form of the finite-difference equation for the horizontal advection-diffusive terms

$$AD_{U1}=C_{U1E}\cdot U_{1E}+C_{U1W}\cdot U_{1W}+C_{U1N}\cdot U_{1N}+C_{U1S}\cdot U_{1S}-C'_{U1P}\cdot U_{1P} \tag{83}$$

where the five-point operator coefficients are defined as follows

$$C_{U1W}=\left[\frac{\overline{\beta}_W|HU_{1W}|+\frac{1}{2}HU_{1W}}{h_{01PE}\delta x}+\frac{A_H}{\delta x\delta x}\right] \tag{84}$$

$$C_{U1E}=\left[\frac{\overline{\beta}_E|HU_{1E}|-\frac{1}{2}HU_{1E}}{h_{01PE}\delta x}+\frac{A_H}{\delta x\delta x}\right] \tag{85}$$

$$C_{U1S}=\left[\frac{\overline{\beta}_S|HV_{1S}|+\frac{1}{2}HV_{1S}}{h_{01PE}\delta y}+\frac{A_H}{\delta y\delta y}\right] \tag{86}$$

$$C_{U1N}=\left[\frac{\overline{\beta}_N|HV_{1N}|-\frac{1}{2}HV_{1N}}{h_{01PE}\delta y}+\frac{A_H}{\delta y\delta y}\right] \tag{87}$$

$$C'_{U1P}=C_{U1W}+C_{U1E}+C_{U1S}+C_{U1N}+\frac{\omega_{1PE}}{h_{01PE}} \tag{88}$$

The interpolation coefficient β as originally introduced can be positive or negative. We will show later, however, that for stability reasons the products like $(\beta_W \cdot HU_{1W})$ must remain positive. This product can be rewritten with β_W always chosen as positive and absolute values placed around the mass flow quantity as seen in equation (84). Examining the advective portion of the C_{U1W} and C_{U1E} coefficients we see that if $\beta_W = \frac{1}{2}$ and the flow is positive (i.e., from West to East) then the advective term in the C_{U1W} coefficient will be $HU_{1W}/(h_{01PE}\delta x)$, while the same term in the C_{U1E} coefficient will be zero. The opposite is true when the flow is from East to West. Thus for both flow directions when $\beta = \frac{1}{2}$ we have a fully upstream differencing scheme, with positive advective coefficients (note: the diffusive term of coefficient is always positive). On the other hand when $\beta=0$ the advective term reduces to a central difference, with one of the two advective coefficients definitely negative. Torrance and Rockett (1969) have shown that a five-point linear equation of the form of equation (83) with the appropriate source and time step added (see Raithby and Torrance 1974) is numerically stable if the coefficients appearing in the equation are all positive. While the upstream difference would always result in a positive advective coefficient and thus a stable numerical solution, the truncation error for this differencing scheme is to first order in δx versus second order for central differences. Therefore, a compromise is required. Beta must be chosen such that the coefficients C_{U1W}, C_{U1E}, etc. are positive for stability reasons, but as close to zero as possible to achieve the increased accuracy of the central differences. If we rewrite the U_{1W} equation coefficient

$$C_{U1W} = \frac{|HU_{1W}|}{h_{01PE}} \left[\beta_W + \tfrac{1}{2} \left(\frac{HU_{1W}}{|HU_{1W}|} \right) + \frac{A_H \, h_{01PE}}{\delta x |HU_{1W}|} \right] \tag{89}$$

and note that the term in square brackets must always be positive, then we obtain an expression for weighting coefficient of the form

$$\beta_W = \text{MAX}\left\{0,\ \tfrac{1}{2} - \frac{A_H\, h_{01PE}}{\delta x\,|HU_{1W}|}\right\} \tag{90}$$

This is scheme IV in Raithby and Torrance (1974) and similar expressions can be derived for the three other coefficients. Equation (90) has the effect of shifting the differencing scheme from the more accurate central difference ($\beta=0$) to the less accurate but stable upstream difference ($0<\beta<\frac{1}{2}$) as the convective flux HU_{1W} across the cell boundaries increases.

Now that we have the advection-diffusion terms it is a simple matter to write down the pressure gradient and Coriolis source terms.

$$\dot{S}_{U1} = -g/\rho_\infty \left[\frac{H_{01PE}}{2}\left(\rho_{1E} - \rho_{1P}\right)/\delta x + \rho_{1PE}\left(h_{0E} - h_{0P}\right)/\delta x\right]$$

$$+ f\left(V_{1S} + V_{1P} + V_{1E} + V_{1SE}\right)/4 \tag{91}$$

Substituting the individual expressions for the advection-diffusion terms (83) and the source term (91) into (74) and redefining some coefficients, we obtain as a final expression of the upper layer U_1-momentum equation

$$C_{U1P}\, U_{1P} = C_{U1W}\, U_{1W} + C_{U1E}\, U_{1E} + C_{U1S}\, U_{1S} + C_{U1N}\, U_{1N} + \dot{S}^L_{U1} + \dot{S}^M_{U1} \tag{92}$$

where C_{U1W}, C_{U1E}, C_{U1S}, C_{U1N} are the same as defined in equations (83) through (86), and

$$C_{U1P} = C'_{U1P} - \bar{\omega}_{12}/h_{01PE} + \alpha_1/h_{01PE} + \alpha_I/h_{01PE} \tag{93}$$

$$\dot{S}^{L}_{U1P} = - g/\rho_{\infty} \left[h_{01PE}/2 \, (\rho_{1E} - \rho_{1P})/\delta x \right] + (\omega^{+}_{12} + \alpha_{I})/h_{01PE} U_{2P} \qquad (94)$$

$$\dot{S}^{M}_{U1P} = - g/\rho_{\infty} \left[\rho_{1PE} (h_{0E} - h_{0P})/\delta x \right] + f(V_{1S} + V_{IP} + V_{1E} + V_{1SE})/4 \qquad (95)$$

The superscript L and M represent the iteration level at which these source terms are updated and will be discussed more fully in a later section.

4.2.2 Pressure-Velocity Coupling

The essence of the pressure-velocity coupling is to determine the distribution of pressure, in this case the h_0 and h_1 fields, which when substituted into the upper and lower layer u- and v- momentum equations, produce U and V velocities that satisfy mass conservation in each layer. Following the method of Patankar and Spalding (1972) we derive a velocity correction equation by holding all terms constant in equation (92), except the central velocity term $C_{U1P}\, U_{1P}$ and the surface pressure gradient. This results in the following h' equations

$$U_{1P} = U^{*}_{1P} - \frac{g\rho_{1PE}}{\rho_{\infty} C_{U1P} \delta x} \left[h'_{0E} - h'_{0P} \right]$$

$$V_{1P} = V^{*}_{1P} - \frac{g\rho_{1PN}}{\rho_{\infty} C_{V1P} \delta y} \left[h'_{0N} - h'_{0P} \right] \qquad (96)$$

where U^{*}_{1P} & V^{*}_{1P} are the velocities obtained from the full upper layer u- and v-momentum equations using a guessed free-surface elevation h^{*}_{0}. The pressure (i.e., the h_0 field) is then updated using

$$h_0 = h^{*}_{0} + \alpha h'_{0} \qquad (97)$$

where α is a relaxation parameter whose value is specified later. A set of equations similar to (96) and (97) is necessary for the bottom layer velocity corrections and interface h_1 update.

Chorin (1968) demonstrated that a non-mass conserving velocity field (U*, V*) when corrected by the appropriate potential field (second term in equation (96)) would give mass conserved velocities. In order to obtain the correct potential field it is necessary to substitute equation (96) into the finite difference representation of the continuity equation as follows:

$$\left(\frac{h_{01PE}U^*_{1P}-h_{01PW}U^*_{1W}}{\delta x}\right)+\left(\frac{h_{01PN}V^*_{1P}-h_{01PS}V^*_{1S}}{\delta y}\right)-\omega_{12P}-\left[\frac{gh_{01PE}\rho_{1PE}}{\rho_\infty C_{U1P}\delta x^2}\right]\left(h'_{0E}-h'_{0P}\right)+$$

$$\left[\frac{gh_{01PW}\rho_{1PW}}{\rho_\infty C_{U1PW}\delta x^2}\right]\left(h'_{0P}-h'_{0W}\right)-\left[\frac{gh_{01PN}\rho_{1PN}}{\rho_\infty C_{V1P}\delta y^2}\right]\left(h'_{0N}-h'_{0P}\right)+\left[\frac{gh_{01PS}\rho_{1PS}}{\rho_\infty C_{V1PS}\delta y^2}\right]\left(h'_{0P}-h'_{0E}\right)=0 \tag{98}$$

Gathering terms we obtain the following Poisson equation for the h'_0 field.

$$C_{hOP}\,h'_{0P} = C_{hOW}\,h'_{0W} + C_{hOE}\,h'_{0E} + C_{hOS}\,h'_{0S} + C_{hON}\,h'_{0N} + \dot{S}_{hOP} \tag{99}$$

where the coefficients and source terms are defined as

$$C_{hOW} = \frac{gh_{01PW}\rho_{1PW}}{\rho_\infty C_{U1PW}\,\delta x^2} \quad ; \quad C_{hOE} = \frac{gh_{01PE}\,\rho_{1PE}}{\rho_\infty C_{U1P}\delta x^2} \tag{100}$$

$$C_{hOS} = \frac{gh_{01PS}\rho_{1PS}}{\rho_\infty C_{V1PS}\,\delta y^2} \quad ; \quad C_{hON} = \frac{gh_{01PN}\,\rho_{1PN}}{\rho_\infty C_{V1P}\delta y^2}$$

$$C_{hOP} = C_{hOW} + C_{hOE} + C_{hOS} + C_{hON} \tag{101}$$

$$\dot{S}_{h0P} = -\left[\left(\frac{h_{01PE}U^*_{1P} - h_{01PW}U^*_{1W}}{\delta x}\right)+\left(\frac{h_{01PN}V^*_{1P} - h_{01PS}V^*_{1S}}{\delta y}\right) - \omega_{12P}\right] \qquad (102)$$

Again a similar Poisson equation is required for the lower layer pressure field involving lower layer velocities and the density difference between the upper and lower layer.

4.2.3 Finite-Difference Boundary Conditions

A simple algebraic expression is used to incorporate the boundary conditions in the finite difference equations. For instance, at the downstream boundary (i=NX) the values of the dependent variables outside the computational domain would be given as follows

$$\begin{aligned} U_{1NX} &= EXN_{U1}\ U_{1NX-1} + FXN_{U1} \\ V_{1NX} &= EXN_{V1}\ V_{1NX-1} + FXN_{V1} \\ S_{1NX} &= EXN_{S1}\ S_{1NX-1} + FXN_{S1} \end{aligned} \qquad (103)$$

Thus the Neumann condition is given by setting EXN = 1 and FXN = 0, while the Dirichelet condition can be specified at the mid-grid point location by setting EXN = -1 and FXN = $2xU_1$ (SPECIFIED). Since the upper and lower layer thicknesses vary during the computation, the velocities normal to the boundary must be modified to insure mass conservation. Thus at the i = NX boundary the U_1 boundary velocity is obtained in the following way

$$h_{01PE}U_{1NX} = h_{01PW}\ EXN_{U1}\ U_{1NX-1} + h_{01PE}\ FXN_{U1}$$

or dividing through by h_{01PE} we have

$$U_{1NX} = (h_{01PW}/h_{01PE})\ EXN_{U1}U_{1NX-1} + FXN_{U1} \qquad (104)$$

There is one further modification of the normal mass flux boundary condition, but only at the river mouth where a constant river discharge is specified. At this location the boundary coefficients are given as follows

$$FX1_{V1} = Q_{RIVER} / (h_{01PS}\, \delta x) \quad ; \quad EX1_{V1} = 0 \tag{105}$$

We have not yet specified any boundary conditions for the h'_0 field. If we specify the velocity or zero mass flux normal to the boundaries then the values of h'_0 outside the computational region are determined by equations like (96). However the normal velocity boundary condition such as equation (103) can be substituted directly into the continuity equation during the derivation of the h'_0 Poisson equation. This results in the following modification to the interior coefficients and source term for the i = NX boundary

$$C^{NX}_{h0PW} = (1. - EXN_{U1})\, C_{h0PW} \quad ; \quad C^{NX}_{h0PE} = 0$$

$$C^{NX}_{h0PN} = C_{h0PN} \quad ; \quad C^{NX}_{h0PS} = C_{h0PS} \tag{106}$$

$$S^{NX}_{h0P} = -\left[\left(\frac{h_{01PE} FXN_{U1} - h_{01PW}(1.-EXN_{U1})\, U^*_{1W}}{\delta x}\right) + \left(\frac{h_{01PN} V^*_{1P} - h_{01PS} V^*_{1S}}{\delta y}\right) - \omega_{12P}\right]$$

Similar modifications to the coefficients and source term occur at the other boundaries.

4.2.4 Solution Procedures

Before discussing the detailed solution procedure it is necessary to reformulate the finite-difference approximation to the steady-state equations of motion and salt conservation into an implicit transient

form by the addition of a local time derivative. The implicit formulation is preferred over an explicit one as the time step permitted by the former is far less restrictive.

Following Raithby and Schneider (1979) the u-momentum equation (92) can be rewritten to represent the implicit advancement of the U_l velocity through the maximum allowable time step δt_p at that location

$$(1 + \frac{1}{E})\, C_{U1P}U_{1P} = C_{U1W}U_{1W} + \text{----} + C_{U1N}U_{1N} + \overset{\bullet L}{S}_{U1} + \overset{\bullet M}{S}_{U1} + \frac{1}{E}\, C_{U1P}U^{o}_{1P} \tag{107}$$

where $E = \delta t_p C_{U1P}$ and U^{o}_{1P} is velocity at P from the previous time step. The solution of equation (107) results in the advancement of U_{1P} through a temporal interval of E times the maximum allowable explicit time step for U_{1P}. The value of the implicit formulation is that values of E in excess of unity can be employed.

Raithby and Schneider (1979) have also shown that a consistent time step should be used to both correct the velocity and update the pressure. They have found that if α is related to E in the following manner a consistent time step is obtained for the pressure-velocity coupling

$$\alpha = \frac{1}{1 + E} \tag{108}$$

The value of α is then substituted into equation (97) and as E increases, that is larger time steps are used, the pressure update is more under-relaxed.

The pressure-velocity coupling algorithm is shown on the left-hand side of Fig. 26 for the upper layer u- and v- momentum equations. It represents the M level of four iteration levels (K,L,M,N) for the complete equation set. If there was no lower layer (i.e., fixed interface), or density-driven circulation, this iteration loop would represent the complete time integration for the U_l and V_l velocities out to

steady state. Convergence is determined when h'_0 has been reduced below a specified level.

Within the pressure-velocity iteration loop there is a further iteration level (N) required for successive applications of the Alternating Direction Implicit line solver. For the U_1* and V_1* equations, only a few applications are required and thus a fixed number of iterations is specified (N=3). However, the h'_0 coefficients are generally more variable and the h'_0 ADI is applied until the maximum equation residual is reduced by a specified percentage or below a minimum level, whichever comes first. The ADI scheme used in this work is as given in Roache (1976) and was supplied by J. Van Doormal, a graduate student at the University of Waterloo.

The coupling for the equation set is given on the left-hand side of Fig. 26. The K iteration level represents the problem level; with K=1 the background flow problem; K=2 the lower river discharge problem; and K=3 the higher river discharge problem, etc. The L iteration level accounts not only for the coupling between the salinity, density and momentum equations, but more importantly for the coupling between the upper and lower layer momentum equations. Both the upper and lower layer thicknesses are adjusted each "L" iteration until successive changes in the crucial upper layer thickness are below a specified level. Also, to avoid zero or negative values of the upper layer thickness, which would cause singularities in the finite-difference solution, a minimum thickness limit is specified. The upper layer thickness, which includes compensation for the density-driven pressure gradient and thus salinity, is monitored to assess convergence to steady state. These and other parameters are graphed in the next chapter, when model sensitivity tests and prototype runs are presented.

4.3 MODEL RESULTS

The numerical model derived in the previous section is first tested on a two-layer open channel flow problem to evaluate different E values for numerical stability, and to check on mass conservation and

pressure fields in a simplified flow problem. Next, the model is used to simulate the fluid motion and salt concentration fields resulting from the discharge of freshwater into the upper layer. The overall solution convergence is demonstrated and different E values are tested to optimize the rate of convergence while maintaining numerical stability. In the next section a number of model parameters are changed and the effect on the solution evaluated. Some of these parameters include friction factors, cross-flow velocities in the upper layer, and vertical diffusion and entrainment coefficients. Finally, the model is run for calibration with the 1980 La Grande salinity field. A further run is made without change of parameters for the lower discharge 1976 La Grande River plume for validation. The parameter values for the model runs shown in the figures are given in Table VI for ease of reference.

4.3.1 Channel Flow Problem

For the channel flow problem the upstream velocities were specified as uniform cross-stream values, and salinity was kept constant in both the upper ($S_1(x,y)$ = 25°/oo) and lower layers ($S_2(x,y)$ = 28°/oo). For all model runs reported in this study the lower layer upstream velocity boundary condition was kept at a uniform value of 5 cm sec^{-1}, except in the linear cross-stream profile of model run 41. The value of 5 cm sec^{-1} is consistent with the near surface mean-flow values observed off La Grande in 1980 and reported in Table II. The value of the upper layer velocity specified at the upstream boundary is determined from the U_1 momentum equation by assuming the interface slope normal to the boundary is zero. This gives a value of 2.9 cm sec^{-1} for the uniform friction coefficients given in Table VI.

The channel flow problem was run out to 500 'L' iterations for a number of different values of the time-step multiple E. It should be noted that for E values less than 1.0 the numerator in the relaxation parameter (equation 108) is replaced by E, i.e., $\alpha = E/(1+E)$. As can be seen in Fig. 27(a), the value of E = 0.2 produces a series of non-converging oscillations in the interface elevation. When E is reduced

to a value of 0.1 these oscillations are no longer unstable, but very slowly converging to a steady-state solution. Oscillations of similar period can be observed in the free-surface displacement at the same location (see Fig. 28 for the grid point location).

The period of these oscillations can be calculated by first estimating the equivalent time step as given by equation (107). From a printout of the coefficients a value of the central coefficient for the U_1 momentum equation can be obtained

$$C_{UIP} = 3.31 \times 10^{-2} \text{ sec}^{-1}$$

C_{UIP} for this problem is principally determined by the magnitude of the friction coefficients. Using this value the time step can be calculated

$$\delta t = E/C_{UIP} = 0.08268 \text{ hrs}$$

From Fig. 27(b) it can be seen that one oscillation is 61 'L' iterations long, and thus has a period of 5.04 hrs. The fundamental free-oscillation period for the surface mode of a long, narrow embayment using Merian's formula, gives a value of 5.275 hrs. Thus the channel flow solution, with a fixed interface reference level at the outflow boundary (24,11) and a specified velocity at the upstream boundary, appears to oscillate at the natural frequency of a quarter wave oscillator.

When this problem is run with a slightly lower value of the upstream velocity in the upper layer ($U_1 = 2.5$), the oscillation disappears altogether (see Fig. 27(d)). What seems to happen is that this lower value of velocity causes a slightly negative interface slope to be established. This results in the interface becoming fixed at the upstream boundary as it runs into the limit value (minimum thickness of 100 cm), and can no longer oscillate as a quarter wave oscillator. In a separate test it was found that when the interface was held fixed over

the entire field no oscillations appeared, and a similar rate of convergence was achieved. For the remaining runs the upper layer velocity specified at the upstream boundary was always slightly less than the value necessary for a zero interface slope. Perhaps a rigid-lid condition of some form can be used to eliminate these barotropic oscillations in future work.

Figure 28 gives the channel flow solution for the converged case (Fig. 27(d)). The first thing to note is that the layer thickness limit (see diagram (b)) is invoked over most of the solution region. Because of the low density contrast between top and bottom layer, as well as the substantial velocity difference between these two layers, a considerable cross-channel interface slope is necessary to effect a geostrohic balance, as shown in diagram (c). To eliminate the intersection of the interface with the free-surface (i.e., the $h_1 = 0$ contour) it is necessary only to lower the interface reference level by another 300 to 400 cm. However, it is useful to study the artificial problem of fixing the upper layer thickness while still maintaining the pressure gradient across it.

In diagrams (a) and (b) of Fig. 28, contour plots of free-surface and interface elevation show the negative linear cross-stream pressure gradient required to balance the flow velocities in the upper layer and the difference in flow velocities between the upper and lower layers, respectively. The curvature of the contours in the downstream direction represents the effect of along-stream pressure gradient balancing frictional stress in that same direction. The pressure gradient is small but negative in each layer, as desired. One further point to note is that, as the layer thickness increases in the upper right-hand corner, the velocity in the upper layer decreases and there is slight increase in the lower layer velocity, as a result of conservation of mass in each layer.

4.3.2 The River Flow Problem

For this case, the V_1 velocity at grid point (9,1) is no longer set to zero, but calculated such that the mass flux into the system at

this location is equal to 1,600 m^3 sec^{-1}. The same upper and lower layer background flow is specified as in the channel flow problem of Fig. 28. Also at grid point (9,1) the zero salinity gradient boundary condition is replaced by a specified value of salinity (S_1 = 0.).

A number of runs are made to determine the largest value of E which will produce a numerically stable solution to the set of coupled equations. The results of some of these tests are shown in Fig. 29. The interface elevation at a central downstream location is used to monitor solution stability. The first thing to note is that the five-hour barotropic oscillation observed in the channel flow solution is very rapidly damped out, as momentum from the river flow distorts the upper layer flow field. However, too large a value of E (i.e., time-step multiple) during this initial oscillation process causes the solution to become unstable almost immediately (see diagram (a), Fig. 29). This problem is overcome by specifying a low value of E for the first 100 'L' iterations, and then increasing it linearly to a larger value for the next 50 iterations. After 150 iterations the E value is held constant. As can be seen in diagrams (b), (c), and (d), final E values of 4.0, 1.0, and 0.9 also lead to numerical instability. However, a final E value of 0.4 does result in a stable solution (diagram (e)). It was later found that a final E value of 0.7 generally results in stable solutions, and almost doubles the rate of convergence (see Fig. 30). The ramp increase from the initial E value to the final E value was also found to be unnecessary and was replaced by a step change at the 150th iteration.

Figure 30 enables us to examine solution convergence for a number of key dependent variables in the river flow problem. The surface salinity values are plotted against number of 'L' iterations in diagram (a). As would be expected, the salinity value just off the river mouth (9,2) reaches its final value quickly within some 50 iterations, i.e., four hours at an E value of 0.1. It takes approximately 56 hours for the downstream (19,2) and the upstream (6,2) salinities to approach their equilibrium values. Beyond this point there appears to be a long

period oscillation, which ranges from 90 to 100 hours, but is eventually damped out. This oscillation is observed in the lower layer velocity, but not the upper layer velocity, thus suggesting that the system is responding to an internal quarter wave-length oscillation similar to the surface mode response observed in the channel flow problem. Using the top-to-bottom density contrast near the river mouth, the period for the internal mode of free-oscillation in the embayment can be computed as 117 hours. It is also interesting to note that the interface elevation approaches equilibrium much faster than the velocity and salinity fields but doesn't appear to have the baroclinic oscillation.

In Fig. 31 the horizontal distribution of the model variables is plotted for the river flow problem. The upper layer cross-flow in diagram (a) is diverted around the river plume. In the upstream region the background flow seems to parallel the lines of constant surface elevation, indicating a fairly strong geostrophic balance in this area. Toward the downstream end of the flow region frictional effects have tended to divert the flow from a strictly geostrophic balance. At the river mouth the flow diverges rapidly, and within four grid points is almost completely in the direction of the background flow. There is a slight increase (2 cm sec^{-1}) in the downstream velocity at grid point (24,11), indicating that the offshore boundary should be further removed from the river mouth, or that some additional momentum dissipators should be brought into play as the river enters the background flow; for example, quadratic friction or a downstream component to the river flow vector.

In diagram (c) of Fig. 31, the flow field in the lower layer is plotted along with the interface elevation. Very little change in the uniform flow field can be observed, except perhaps a slight deflection toward the plume in the upstream* region. The interface elevation

* In this section upstream and downstream are defined in relation to the cross-flow not the river flow.

field, while generally reflecting the free-surface elevation distribution as in the quasi-compensation assumption, appears to diverge from it in the offshore region, where there are very small horizontal density gradients. Just off the river mouth the interface changes rapidly from 4 m to a minimum of 2.5 m, some 6 to 12 km from the river mouth. This is in the same direction, but more rapid than observed in the actual field observations, and may be related to the depth of the reference level specified in the numerical model. In diagram (b) the surface salinity distribution is given. Upstream of the river mouth a sharp frontal region is predicted by the model, while downstream a considerable amount of the salt is advected out of the solution region. It should be noted that vertical diffusion of salt has not yet been included in the salt conservation equation. As we will see later, its inclusion will bring the downstream salinity distribution more in line with actual field observations.

4.3.3 Model Parameter Testing

Starting with the model results presented in Fig. 31 as the reference case, model parameters were systematically changed to test the sensitivity of the model predictions to alternate values of the coefficients. Table VI gives the values employed in these model tests and indicates the figures in which the results are presented.

The first such test undertaken was the variation of frictional coefficients. The absolute values of the friction coefficients were taken from Karelse et al. (1974). Each of the three coefficients, ice, interface and bottom, were varied separately while holding the other two constant. However, for each test the upstream U_1 boundary velocity was recalculated to give zero interface slope at that point. This value of velocity was reduced slightly, by the same amount in each case, in order to give a small negative slope to the interface at this upstream boundary. Since the background flow fields differed with different friction coefficients, it was difficult to observe the effect of these changes on the flow field - thus the more sensitive interface elevation

distribution was chosen instead. In Fig. 32, diagram (a) and diagram (b) represent the results of halving the ice friction and interface friction coefficients, respectively. Diagram (c) gives the results of a five-fold increase in bottom friction coefficient. As can be seen by comparing these three cases with the reference case in Fig. 31, the most significant difference in the interface elevation contour patterns is as a result of the weakening of the cross-stream geostrophic pressure gradients (diagrams (a) and (c), Fig. 32), resulting from the reduced top-to-bottom velocity contrasts ($U_1 - U_2$). Near the river mouth the patterns appear similar, with only the cross-stream gradients significantly affected by the velocity contrasts. Overall, the exact choice of friction coefficient seems to have little effect on the along-stream pressure field.

In Fig. 33 two quite different background flow conditions are investigated. For the model results presented in diagram (a), U_1 is set to zero at the upstream boundary. In this case the river momentum drives a recirculation cell upstream of the river outflow. Downstream of the river mouth the outflow appears to be less shorebound, and seems to reach all the way across to the offshore boundary. It should be noted that the layer thickness limit is reached at the interface elevation of -100, but fixing the upper layer thickness at 100 cm in this region doesn't appear to affect the recirculating cell significantly. In diagram (b) we see the results of prescribing a linearly decreasing U_1 and U_2 boundary condition. U_1 ranges from 2.5 cm sec^{-1} at the shoreward end of the upstream boundary to 0.0 at the seaward end, and U_2 ranges from 5.0 to 0.0 cm sec^{-1}. The flow field around the river mouth is not significantly altered, but there is a general reduction in background flow. However, this run does emphasize the fact that the offshore boundary at its present location is influencing the background flow, and should be moved further offshore in future work. It is interesting to note that the cross-stream pressure gradients are weaker in the offshore region due to the reduction in layer velocity contrast ($U_1 - U_2$) in this direction.

In Fig. 34 the results of altering the interface elevation reference level are presented. The reference level at point (24,11) was set to -200 instead of the normal -400 cm. This resulted in a considerable reduction in the layer thickness in the upstream region of the background flow. For this experiment the layer thickness limit was reduced to 50 cm. Little change was observed in the downstream flow field, except an overall reduction in velocities due to the decreased mass flow at the upstream boundary. However, the salinity distribution (diagram (b)) showed a marked increase in advection of salt out of the system, due to the increased flow field off the river mouth.

In Fig. 35 the results of a vertical diffusion and downward entrainment test are presented. As can be seen in diagram (a), vertical diffusion tends to replace the salt advected horizontally out of the system. This results in salinity contours that are more representative of the actual plume observations. Downward entrainment tends to counter this effect by advecting brackish water out of the plume. Since the change in the surface salinity distribution was slight for the value of entrainment coefficient used, it was decided to plot the interface elevation to see if upper layer thinning was occurring. As can be seen in diagram (b) of Fig. 35, the interface elevation does significantly decrease in the downstream direction. For the remaining runs, however, only vertical diffusion has been included in the model formulation. Additional work is needed to investigate the effect of Richardson number on the diffusion and entrainment coefficients.

4.3.4 La Grande Model Predictions

The model predictions for the La Grande 1980 discharge condition of 1600 m^3 sec^{-1} and the La Grande 1976 discharge of 500 m^3 sec^{-1} are presented in Fig. 36. Only the salinity field is given for the first case, as the flow field is similar to that shown in Fig. 31. A slight reduction in horizontal diffusion coefficient from the model run presented in Fig. 35(a) results in salinity contours that are more representative of field observations. Comparing diagram (a) with Fig. 8, we see

that there is generally good agreement on the overall size of the surface plume, but that the sharpness of the frontal regions is underestimated. This must be due in part to the lack of a Richardson number dependent relationship for the vertical diffusion coefficient. The sharp upstream frontal region and the downstream spreading of the isohalines are well represented in the model predictions.

The salinity observations collected in the winter of 1976 (see Fig. 19) provide an independent check on the model's predictive capability. The modelled salinity contours for the 1976 discharge case are presented in diagram (b) of Fig. 36. Once again the areal extent of the brackish water plume is well represented by the model prediction. The frontal regions are still less sharply defined than in the actual observations, but the overall shape of the surface plume and distribution of salinity is quite similar to the observations in Fig. 19(b). It is interesting to note that for this lower discharge case the background flow along the seaward boundary is largely unaltered in the downstream direction, due to the reduced momentum of the river flow. The interface also rises sharply off the river mouth this time to a minimum layer thickness of about 1.0 m. This is about two-fifth's the thickness of the upper layer in the higher discharge case of 1980. Figures 19(a) and (b) give the pycnocline depths for these discharge cases, and when 1 to 1.5 m of ice thickness is subtracted from these observed depths, reasonable agreement with the model results is obtained. Perhaps agreement could be further enhanced by adjusting the interface reference level.

4.3.5 Conclusions Based on the Two-Layer Model

As we have seen in the previous section, the two-layer model with constant coefficients effectively predicts the areal extent of the river plume under different discharge conditions. The horizontal salinity distributions are well reproduced, but the sharp frontal regions are underestimated. The flow field is in good qualitative agreement with the observed velocity field, particularly near the river mouth. As well, the upper layer thinning just off the river entrance as observed

in the pycnocline depth data is reasonably well reproduced for the dependent (1980) and independent (1976) test cases. The sensitivity of the model results to relative values of the friction coefficients for ice, interface, and bottom seems to be small. However, the interface reference level and the upstream velocity (U_1) boundary condition seem to have an effect on both the upper layer thickness and the advection of salt out of the solution domain.

Further work is required on the model prior to using it as a tool to study the effects of different vertical diffusion and entrainment formulations. Testing of other interface reference levels is a first priority. The introduction of quadratic friction is essential as a further momentum dissipator near the river mouth, which in turn should reduce the river flow to the offshore boundary. Also, the introduction of a variable grid mesh with finer grid spacing near the river mouth and a coarser grid at the offshore boundary should help obviate this problem. Ways to eliminate the oscillations in the solution convergence should be investigated. Finally, a fine tuning of the model is necessary before any non-uniform formulation of vertical diffusion and entrainment is introduced.

5. CONCLUSIONS

The detailed conclusions relating to the measurement and modelling efforts undertaken in this study have been included at the end of the relevant chapters. Therefore, only a brief summary of the work will be presented here.

The primary purpose of the numerical modelling work was to provide a means of predicting the horizontal and vertical distribution of brackish water resulting from changes in freshwater discharge brought about by the James Bay hydroelectric developments. Data sets collected in 1980 and 1976 under different discharge conditions were used respectively to calibrate and to verify the model predictions of the salt concentration fields. A secondary objective of both the field measurements and mathematical modelling was to obtain a more complete understanding of the mixing processes (particularly the competing roles of stratification and tidally-generated turbulence), as well as the balance of forces in freshwater plumes under an ice cover.

From the observations of flow and salinity fields near the mouth of the La Grande River there would appear to be very little shear-generated turbulence. Thus, under the present discharge rates no near-field region (using the definition of Jirka et al. 1975) is presently observed in the under-ice river plume. Whether the substantially increased post-project discharges will create sufficient turbulence, or still enable internal hydraulic control to be maintained, must be the subject of future experimental and theoretical investigations.

The two-layer numerical model presented in Chapter 4 is capable of modelling both the near- and far-field, and thus could be considered as a complete field model in the definitions of Jirka et al. However, the large horizontal grid scale used in the model runs ($\delta x, \delta y = 4.0$ km) reduces the influence of horizontal advection and diffusion to an order of magnitude less than similar terms in the vertical. This would tend to minimize the effect of horizontal shear and inertia, even in the higher velocity region around the river mouth. Thus the near-field is effectively smoothed over and a far-field balance of forces exists over

the entire solution region. This balance of forces is between the pressure gradient (made up of a horizontal density gradient and interface slope) and vertical gradients in shear at the ice and interface surfaces. Momentum dissipation around the river mouth is further smoothed out in the model runs, as a linearized friction coefficient is used for momentum dissipation in the vertical. A better representation of the near-field processes would be accomplished by employing a finer grid near the river mouth and quadratic friction in the vertical.

The two-layer numerical model differs in a number of respects from the upper layer model of the Fraser River plume (Stronach 1975). Firstly, two full layers are included in the numerical solution, thus eliminating the need for the quasi-compensation assumption, which is restrictive when applied to shallow waters. Also the two-layer approach enables the upper and lower layer coupling to be examined in some detail. Secondly, the much smaller top-to-bottom density differences (Stronach: $g' \approx 10$ cm sec^{-2} versus Freeman: $g' \approx 1$ to 2 cm sec^{-2}) at the extremities of the solution region in the present model, leads to substantial interface displacements. This necessitated the development of a technique to handle interface intersection of the free-surface. Thirdly, while a direct comparison has not been made, it would appear that the use of the pressure-velocity coupling and an implicit transient approach to the numerical solution of the equations is more efficient than Stronach's time stepping scheme.

The numerical model presented in this thesis when related to other mathematical models of plume dispersion would appear to represent the horizontal flow (including geostrophic effects) and dilution fields better than integral models, but at a much lower cost (computationally) than the three-dimensional models of Waldrop and Farmer (1973), and Paul and Lick (1974).

In summary, phase I of the research involved extensive field measurements over a two-year period in the winter in James Bay. An in-depth analysis of these observations provided:

1) three independent data sets of the salt concentration field under different discharge and tidal conditions;

2) the first flow measurements in and below a freshwater plume under an ice-cover;
3) general mixing relationships for under-ice river plumes; and
4) an indication of the biological importance of these lenses of fresh water to the spring phytoplankton bloom.

Phase II involved a study of the balance of forces affecting the mixing and motion of the freshwater plume. The development and testing of a two-layer model achieved the following objectives:

1) a predictive capability of the areal extent of the surface plume,
2) a means of studying the flow and dilution fields.

Further work, however, is required on the two-layer numerical model to employ it as a tool for the investigation of various mixing relationships.

REFERENCES

Alexander, V. 1974. Primary productivity regions of the nearshore Beaufort Sea, with reference to the potential role of ice biota. In: The Coast and Shelf of the Beaufort Sea, eds. J.C. Reed and J.E. Sater, pp. 609-632. Arctic Institute of North America, Arlington, Virginia.

Baird, S.D. and Anning, J.L. 1979. La Grande/Great Whale winter oceanographic survey - 1979 Field Report. Bayfield Laboratory for Marine Science and Surveys, Dept. of Fish. and Oceans, Canada Centre for Inland Waters, Burlington, Ont.

Barber, F.G. 1967. A contribution to the oceanography of Hudson Bay. Manuscript Report Series No. 4, Marine Sciences Branch, Dept. of Energy, Mines and Resources, Ottawa, Ont.

Barber, F.G. 1978. Speculation concerning fish populations in the water of the Hudson Bay system. Fisheries and Marine Service Technical Report No. 829, Fish. and Oceans, Ottawa, Ont. 6 p.

Barber, F.G., Murty, T.S. and Godin, G. 1972. On the oceanography of James Bay. Manuscript Report Series No. 24, Marine Sciences Branch, Dept. of the Environment, Ottawa, Ont.

Barber, F.G. and Murty, T.S. 1977. Perennial sea ice: Speculations concerning physical and biological consequences. In: Polar Oceans, ed. M.J. Dunbar, pp. 257-268. Proc. of the Polar Oceans Conf., May 1974. McGill University, Montreal. 682 p.

Bowden, K.F. 1967. Circulation and diffusion. In: Estuaries, ed. Lauff, pp. 15-36. Washington: A.A.A.S. Publication 83.

Bowman, M.J. 1978. Spreading and mixing of the Hudson River effluent into the New York bight. In: Hydrodynamics of Estuaries and Fjords, ed. J.C.J. Nihoul, pp. 373-386. Elsevier Oceanographic Series, 23.

Brooks, D.J. 1980. James Bay/La Grande winter oceanographic survey - 1980 Field Report. Bayfield Laboratory for Marine Science and Surveys, Dept. of Fish. and Oceans, Canada Centre for Inland Waters, Burlington, Ont. 74 p.

Bugden, G.L., Hargrave, B.T., Sinclair, M.M., Tang, C.L., Therriault, J.-C. and Yeats, P.A. 1981. Freshwater runoff effects in the marine environment: the Gulf of St. Lawrence example. Internal Report, Bedford Institute of Oceanography, Dartmouth, Nova Scotia.

Cordes, R. E., Pond, S., de Lange Boom, B.R., Le Blond, P.H. and Crean, P.B. 1980. Estimates of entrainment in the Fraser River plume, British Columbia. Atmos. Ocean, 18:15-26.

Chorin, A.J. 1968. Numerical solution of the Navier-Stokes equations. Mathematics of Computation. 22:745-762.

Csanady, G.T. 1973. Turbulent Diffusion in the Environment. Geophysics and Astrophysics Monographs. D. Reidel Publishing Company, Boston.

Dunbar, M.J. and Acreman, J.C. 1980. Standing crops and species composition of diatoms in sea ice from Robeson Channel to the Gulf of St. Lawrence - Ophelia. 19:61-72.

Dunn, W.E., Policastro, A.J. and Paddock, R.A. 1975. Surface thermal plumes: evaluation of mathematical models for the near and complete field. Argonne National Laboratory, ANL/WR-75-3, Part 1, 397 p., Part 2, 531 p.

El Sabh, M.J. and Koutitonsky, V.G. 1977. An oceanographic study of James Bay before the completion of the La Grande hydroelectric complex. Arctic, 30:3:169-186.

Environment Canada. 1974. Analytical Methods Manual. Inland Waters Directorate, Water Quality Branch, Environment Canada, Ottawa, 148 p.

Festa, J.F. and Hansen, D.V. 1976. A two-dimensional numerical model of estuarine circulation: the effects of altering depth and river discharge. Estuarine and Coastal Marine Science. 4:309-323.

Fischer, H.B. 1972. Mass transport mechanisms in partially stratified estuaries. J. Fluid Mech. 53:4:671-687.

Fischer, H.B. 1976. Mixing and dispersion in estuaries. Annual Review of Fluid Mechanics. 8:107-133.

Foreman, M.G.G. 1978. Manual for tidal currents analysis and prediction. Pacific Marine Science Report 78-6, Institute of Ocean Sciences, Patricia Bay, Sidney, B.C.

Freeman, N.G., Hale, A.M. and Danard, M.B. 1972. A modified sigma equations' approach to the numerical modelling of Great Lakes hydrodynamics. J. Geophys. Res. 77:6:1050-1060.

Freeman, N.G. and Murty, T.S. 1976. Numerical modelling of tides in Hudson Bay. J. Fish. Res. Board of Canada. 33:10:2345-2361.

Freeman, N.G., Roff, J.C. and Pett, R.J. 1982. Physical, chemical and biological features of river plumes under an ice cover in James and Hudson Bays. Accepted for publication in Le Naturaliste Canadien, Les Presses de L'Université Laval, Quebec, P.Q.

Fujino, K., Lewis, E.L. and Perkin, R.G. 1974. The freezing point of seawater at pressures up to 100 bars. J. Geophys. Res. 79:12:1792-1797.

Garvine, R.W. 1974a. Physical features of the Connecticut River outflow during high discharge. J. Geophys. Res. 79:6:831-846.

Garvine, R.W. 1974b. Dynamics of small-scale oceanic fronts. J. Phys. Oceanogr. 4:557-569.

Garvine, R.W. 1977. Observations of the motion field of the Connecticut River plume. J. Geophys. Res. 82:3:441-454.

Garvine, R.W. 1979a. An integral, hydrodynamic model of upper ocean frontal dynamics. Part I. Development and analysis. J. Phys. Oceanogr. 9:1-18.

Garvine, R.W. 1979b. An integral, hydrodynamic model of upper ocean frontal dynamics. Part II. Physical characteristics. J. Phys. Oceanogr. 9:19-36.

Garvine, R.W. and Monk, J.D. 1974c. Frontal structure of a river plume. J. Geophys. Res. 79:15:2251-2259.

Gerrath, J., Roff, J.C. and Anderson, J.T. 1980. Phytoplankton of fresh-water origins in Hudson Bay. Nova Hedwigid. 32:167-183.

Grainger, E.H. and McSween, S. 1976. Marine zooplankton and some physical-chemical features of James Bay related to La Grande hydro-electric development. Fisheries and Marine Service Technical Report No. 650, Ottawa, Ont. 94 p.

Grainger, E.H. 1979. Primary production in Frobisher Bay, Arctic Canada. In: Marine Production Mechanisms, ed. M.J. Dunbar, pp. 9-30. Cambridge University Press, International Biological Programme 20.

Hansen, D.V. and Rattray, Jr., M. 1965. Gravitational circulation in straits and estuaries. J. Mar. Res. 23(2):104-122.

Harleman, D.R.F. 1966. Diffusion processes in stratified flow. In: Estuary and Coastline Hydrodynamics, ed. A.T. Ippen, pp. 565-597. New York: McGraw-Hill Book Company Ltd. 747 p.

Holm-Hansen, O. 1973. Determination of total microbial biomass measurement of adenosine triphosphate. In: Estuarine Microbial Ecology, eds. L.H. Stevenson and R.B. Colwell, pp. 73-89. Estuarine Microbial Ecology, U. of South Carolina Press, Columbia, S.C.

Hsiao, S.I.C. 1980. Quantitative composition, distribution, community structure and standing stock of sea ice microalgae in the Canadian Arctic. Arctic. 33:768-793.

Hunter, J.G. 1968. Fishes and fisheries. Chapter 7, Volume I, Science and History of Hudson Bay, ed. C.S. Beals. Dept. of Energy, Mines and Resources, Ottawa, Ont.

Ingram, R.G. 1981. Characteristics of the Great Whale River plume. J. Geophys. Res. 86:C3:2017-2023.

Ippen, A.T. 1966. Salinity intrusion in estuaries. In: Estuary and Coastline Hydrodynamics, ed. Ippen. Engineering Societies Monographs. New York: McGraw-Hill Book Company, 747 p.

Kato, H. and Phillips, O.M. 1969. On the penetration of a turbulent layer into a stratified fluid. J. Fluid Mech. 37:4:643-655.

Karelse, M., Vreugdenhill, C.B. and Delvigne, G.A.L. 1974. Momentum and mass transfer in stratified flows. Report on Literature Study, Delft Hydraulics Laboratory.

Keulegan, G.H. 1966. The mechanism of an arrested saline wedge. In: Estuary and Coastline Hydrodynamics, ed. Ippen. New York: McGraw-Hill Book Company Ltd.

Lewellen, W.S. 1977. Use of invariant modelling. In: Handbook of Turbulence, eds. Walter Frost and Trevor Moulden. Volume I: Fundamentals and Applications. New York and London: Plenum Press.

Long, R.R. 1975. Circulations and density distributions in a deep, strongly stratified, two-layer estuary. J. Fluid Mech. 71:3:529-540.

Mackinnon, M.L. 1976. Measurement of adenosine triphosphate (ATP) in freshwaters. Unpublished Report, Canada Centre for Inland Waters, Environment Canada, Burlington, Ont. 13 p.

McClimans, T.A. 1979. On the energetics of river plume entrainment. Geophys. Astrophys. Fluid Dynamics. 13:67-81.

Munk, W.H. and Anderson, E.R. 1947. Notes on a theory of the thermocline. J. Mar. Res. 7:276-295.

Neu, H.J.A. 1976. Runoff regulation for hydro-power and its effect on the ocean environment. Hydrological Sciences, Bulletin XXI, 3, 9, pp. 433-444.

Paul, J.F. and Lick, W.J. 1973. A numerical model for a three-dimensional variable-density jet. Proc. of 16th Conf. on Great Lakes Research. pp 818-830.

Paul, J.F. and Lick, W.J. 1974. A numerical model for thermal plumes and river discharges. Proc. of 17th Conf. on Great Lakes Research. pp 445-455.

Peck, G.S. 1976. Winter and nearshore oceanography of James Bay. In Proceedings of the James Bay Environment Symposium, pp. 115-145. Société d'Energie de la Baie James, Montreal, Quebec, P.C.

Peck, G.S. 1978. James Bay oceanographic data report. Volume 1: winter, 1975 and 1976. Bayfield Laboratory for Marine Science and Surveys, Dept. of Fish. and Oceans, Canada Centre for Inland Waters, Burlington, Ont., 151 p.

Peck, G.S. 1980. Arctic oceanographic data report 1979: Sverdrup Basin. Volume 1: Data Report Series No. 80-2. Research and Development Division, Dept. of Fish. and Oceans, Canada Centre for Inland Waters, Burlington, Ont.

Pett, R.J. 1981. Biological oceanographic studies of the La Grande River plume, James Bay - winter 1980. Volume 1, Nutrients and Seston. Final Report to Supply and Services Canada, Dept. of Fish. and Oceans, Canada Centre for Inland Waters, Burlington, Ont. (In press.)

Prinsenberg, S.J. 1978. Analytical study of the circulation of James Bay. Manuscript Report Series No. 6, Ocean and Aquatic Sciences, Central Region, Canada Centre for Inland Waters, Burlington, Ont.

Prinsenberg, S.J. 1980. Man-made changes in the freshwater input rates of Hudson and James Bays. Canadian J. Fish. and Aquatic Sci. 37:7:1101-1110.

Prinsenberg, S.J. and Collins, D. 1979. Hudson Bay/Great Whale oceanographic data report - Winter 1977. Bayfield Laboratory for Marine Science and Surveys, Dept. of Fish. and Oceans, Canada Centre for Inland Waters, Burlington, Ont.

Pritchard, D.W. 1954. Salt balance in a coastal plain estuary. J. Mar. Res. 13:1:133-144.

Pritchard, D.W. 1956. The dynamic structure of a coastal plain estuary. J. Mar. Res. 15:1:33-42.

Raithby, G.D. and Torrance, G.E. 1974. Upstream-weighted differencing schemes and their application to elliptic problems involving fluid flow. Computers and Fluids. 2:191-206. Pergamon Press.

Raithby, G.D. and Schneider K.E. 1979. Numerical solution of problems in incompressible fluid flow: treatment of the velocity-pressure coupling. Numerical Heat Transfer. 2:417-440.

Rattray, Jr., M. and Hansen, D.V. 1962. A similarity solution for circulation in an estuary. J. Mar. Res. 20:2:121-133.

Rattray, Jr., M. 1967. Some aspects of the dynamics of circulation in fjords. In: Estuaries, ed. Lauff, pp. 52-62. Washington: A.A.A.S. Publication 83.

Roache, P.J. 1976. Computational Fluid Dynamics. Hermosa Publishers, Albuquerque, N.M.

Simons, T.J. 1980. Circulation Models of Lakes and Inland Seas. Can. Bull. Fish. Aquat. Sci. 203: 146 p.

Stewart, R.W. 1959. The problem of diffusion in a stratified fluid. Adv. Geoph. 16.:303-311.

Stommel, H. and Farmer, H.G. 1952. Abrupt change in width in two-layer open channel flow. J. Mar. Res. XI:2:205-214.

Strickland, J.D.H. and Parsons, T.R. 1972. A practical handbook of seawater analysis. Bulletin 167. Fish. Res. Board of Canada, Ottawa, Ont. 310 pp.

Stronach, J.A. 1978. Observational and modelling studies of the Fraser River plume. PhD Thesis, Institute of Oceanography, U. of British Columbia.

Sutcliffe, Jr., W.H. 1972. Some relations of land drainage, nutrients, particulate material, and fish catch in two eastern Canadian bays. J. Fish. Res. Board of Canada. 29:4:357-362.

Sweers, H.E. 1970. Oceans IV: a processing, archiving and retrieval system for oceanographic station data. Manuscript Report Series No. 15, Marine Sciences Branch, Dept. of Energy, Mines and Resources.

Takano, K. 1954a. On the velocity distribution off the mouth of a river. J. Ocean. Soc. of Japan. 10:60-64.

Takano, K. 1954b. On the salinity and velocity distribution off the mouth of a river. J. Ocean. Soc. of Japan. 10:92-98.

Takano, K. 1955. A complementary note on the diffusion of the seaward flow off the mouth of a river. J. Ocean. Soc. of Japan. 11:1-3.

Torrance, K.E. and Rockett, J.A. 1969. Numerical study of natural convection in an enclosure with localized heating from below. J. Fluid Mech. 36:33-54.

Waldrop, W. and Farmer, R.C. 1974. Three-dimensional computation of buoyant plumes. J. Geophys. Res. 79:9:1269-1276.

Walker, E.R. and Chapman, K.D. 1973. Salinity-conductivity formulae compared. Pacific Marine Science Report 73-5, Marine Sciences Directorate, Pacific Region, Dept. of the Environment.

Welander, P. 1966. A two-layer frictional model of wind-driven motion in a rectangular oceanic basin. Tellus XVIII, 1:54-66.

Welander, P. 1968. Wind-driven circulation in one- and two-layer oceans of variable depth. Tellus XX, 1:1-15.

Wright, L.D. and Coleman, J.M. 1971. Effluent expansion and interfacial mixing in the presence of a salt wedge, Mississippi River delta. J. Geophys. Res. 79:36:8649-8661.

APPENDIX A - TABLES

TABLE II - ANALYSIS OF CURRENT METER DATA

STN. NO.	STN DEPTH m	AVG SAL o /oo	C.M. DEPTH m	MEAN		M_2				$\frac{K_1+O_1}{M_2+S_2}$	$\frac{S_2}{M_2}$	$\frac{N_2}{M_2}$
				MEAN cm sec^{-1}	INC[1] °	MAJOR cm sec^{-1}	MINOR[3] cm sec^{-1}	INC[2] °	G[4] °			
260	7	0.0	2.5	48.5	173	18.6	-0.2	172	153	0.059	0.34	0.29
		0.0	3.5	49.2	194	18.8	-0.4	193	135	0.067	0.34	0.33
01A	16	20.0	3.0	5.3	103	19.8	-11.0	81	188	0.076	0.18	0.14
		23.5	6.0	2.9	136	15.6	-8.1	83	206	0.055	0.23	0.29
		24.0	10.0	1.9	79	9.7	-3.5	97	229	0.139	0.27	0.34
238	19	18.0 to 4.0	2.0	5.3	140	3.5	-0.7	157	140	0.458	0.43	0.40
		20.0 to 18.0	3.0	2.8	159	20.0	-3.2	141	152	0.171	0.34	0.26
		21.0	5.0	3.0	139	TIME ERROR						
		23.0	10.0	2.0	188	19.2	0.5	177	147	0.148	0.33	0.28
		23.5	15.0	3.9	68	20.0	0.7	26	345	0.126	0.28	0.26

1 the angle of the mean flow measured in degrees counter-clockwise from east (true)
2 the inclination of the major axis of the tidal current ellipse in degrees counter-clockwise from east (true)
3 if the sign of the minor axis is negative, the current vector rotates clockwise
4 the Greenwich phase lag in degrees referred to GMT

TABLE III - CORRELATIONS (PEARSON'S r) BETWEEN NUTRIENT AND SESTON VARIABLES

	Phaeo	Chlor *a*	BIOC	POC	SiO_2	$NO_3 + NO_2$	TDKN	TDP	TP
Salinity	-0.50	-0.53	-0.46	-0.77	0.39	0.96	0.64	0.90	0.86
TP	-0.49	-0.53	-0.51	-0.63	0.41	0.84	0.70	0.92	
TDP	-0.54	-0.57	-0.54	-0.71	0.36	0.85	0.69		
TDKN	NS	NS	-0.42	-0.46	NS	0.63			
$NO_3 + NO_2$	-0.55	-0.54	-0.41	-0.79	0.41				
SiO_2	NS	-0.63	NS	NS					
POC	NS	0.48	0.45						
BIOC	NS	0.66							
Chlor *a*	NS								

P <0.05 for all values; NS = not significant.

TABLE IV - ESTIMATES OF FRESHWATER CONTENT ABOVE PYCNOCLINE
(RELATIVE TO BASE SALINITY OF 30 °/oo)

	DATES	Q m^3/sec	FW hmin m^3	FW 25°/oo m^3	Δt hmin days	Δt 25°/oo days
GREAT WHALE - 1979	FEB. 8-18	200	422×10^6	422×10^6	24.4	24.4
LA GRANDE - 1976	FEB. 27 to MAR. 3	450	355×10^6	$1,652 \times 10^6$	9.13	42.5
LA GRANDE - 1980	FEB. 3-10	1,400	$1,342 \times 10^6$	$4,486 \times 10^6$	11.1	37.1
	MARCH 1-9	1,800	$1,866 \times 10^6$	$5,454 \times 10^6$	11.9	35.1
	MARCH 15-30	1,500	$1,711 \times 10^6$	$4,798 \times 10^6$	13.2	37.0

TABLE V - SCALE ANALYSIS

REGION	SCALE VALUES			x, y MOMENTUM					z MOMENTUM				
	U cm sec^{-1}	L cm	H cm	$\frac{U^2}{L}$	$\frac{g\eta}{L}$	$\frac{A_H U}{L^2}$	$\frac{A_V U}{H^2}$	fU	$\frac{U^2}{L}\frac{H}{L}$	$\frac{g\eta}{H}$	g	$\frac{A_H U}{L^2}\frac{H}{L}$	$\frac{A_V U}{H^2}\frac{H}{L}$
PLUME NEAR-FIELD	10	10^5	10^2	10^{-3}	$10^{-2}\eta$	10^{-3}	10^{-2}	10^{-3}	10^{-6}	10η	10^3	10^{-6}	10^{-5}
PLUME FAR-FIELD	1	10^6	10^2	10^{-6}	$10^{-3}\eta$	10^{-6}	10^{-3}	10^{-4}	10^{-10}	10η	10^3	10^{-10}	10^{-7}
BASIN	1	10^6	10^3	10^{-6}	$10^{-3}\eta$	10^{-6}	10^{-5}	10^{-4}	10^{-9}	η	10^3	10^{-9}	10^{-8}

$g = 10^3$ cm sec^{-2} ; $f = 10^{-4}$ sec^{-1} ; $A_H = 10^6$ cm^2 sec^{-1} ; $A_V = 10$ cm^2 sec^{-1}

TABLE VI - PARAMETER VALUES USED IN RUNS OF TWO-LAYER MODEL

Run No.	Figure No.	$U_{1/x=0}$ cm sec^{-1}	Q_o m^3 sec^{-1}	k_i × 10^{-3}	k_I × 10^{-3}	k_b × 10^{-3}	K_e × 10^{-5}	$K_H \times 10^6$ cm^2 sec^{-1}	k_s × 10^{-5}	h_{1REF} cm	h_{01LIM} cm	Model Constants
3.4	27(a),(b),(c)	2.9	0.0	2.0	2.0	1.0	0.0	1.0	0.0	-400	100	g = 980 cm sec^{-2}
9	27(d)	2.5	0.0	2.0	2.0	1.0	0.0	1.0	0.0	-400	100	
9	28(a),(b),(c)	2.5	0.0	2.0	2.0	1.0	0.0	1.0	0.0	-400	100	$f = 1.176 \times 10^{-4}$ sec^{-1}
14,13 15,16,21	29	2.5	1600	2.0	2.0	1.0	0.0	1.0	0.0	-400	100	ρ_∞ = 1.022 gm cm^{-3}
21	30	2.5	1600	2.0	2.0	1.0	0.0	1.0	0.0	-400	100	$A_H = 10^6$ cm^2 sec^{-1}
21	31	2.5	1600	2.0	2.0	1.0	0.0	1.0	0.0	-400	100	$\delta x, \delta y = 4 \times 10^5$ cm
24	32(a)	3.5	1600	1.0	2.0	1.0	0.0	1.0	0.0	-400	100	
25	32(b)	2.0	1600	2.0	1.0	1.0	0.0	1.0	0.0	-400	100	υ_1 = 5 cm sec^{-1}
26	32(c)	3.5	1600	2.0	2.0	5.0	0.0	1.0	0.0	-400	100	υ_2 = 10 cm sec^{-1}
27	33(a)	0.0	1600	2.0	2.0	5.0	0.0	1.0	0.0	-400	100	υ_{12} = 5 cm sec^{-1}
41	33(b)	2.5-0.	1600	1.0	2.0	2.0	0.0	1.0	0.0	-400	100	$S_{1/x=0, y=Y}$ = 25°/oo
30	34(a)	2.5	1600	2.0	2.0	5.0	0.0	1.0	0.0	-200	50	$S_{2/x=0, y=Y}$ = 28°/oo
30	34(b)	2.5	1600	2.0	2.0	5.0	0.0	1.0	0.0	-200	50	
51	35(a)	2.5	1600	2.0	2.0	1.0	0.0	1.0	4.0	-400	100	δS = 2°/oo
46	35(b)	2.5	1600	2.0	2.0	1.0	0.8	1.0	0.0	-400	100	γ = 0.0001
53	36(a)	2.5	1600	2.0	2.0	1.0	0.0	0.5	4.0	-400	100	U_2 = 5.0 cm sec^{-1}
55	36(b)	2.5	500	2.0	2.0	1.0	0.0	0.5	4.0	-400	50	33(b) U_2 = 5.0 → 0.0
55	36(c)	2.5	500	2.0	2.0	1.0	0.0	0.5	4.0	-400	50	h_{02} = 4000 cm

APPENDIX B - FIGURES

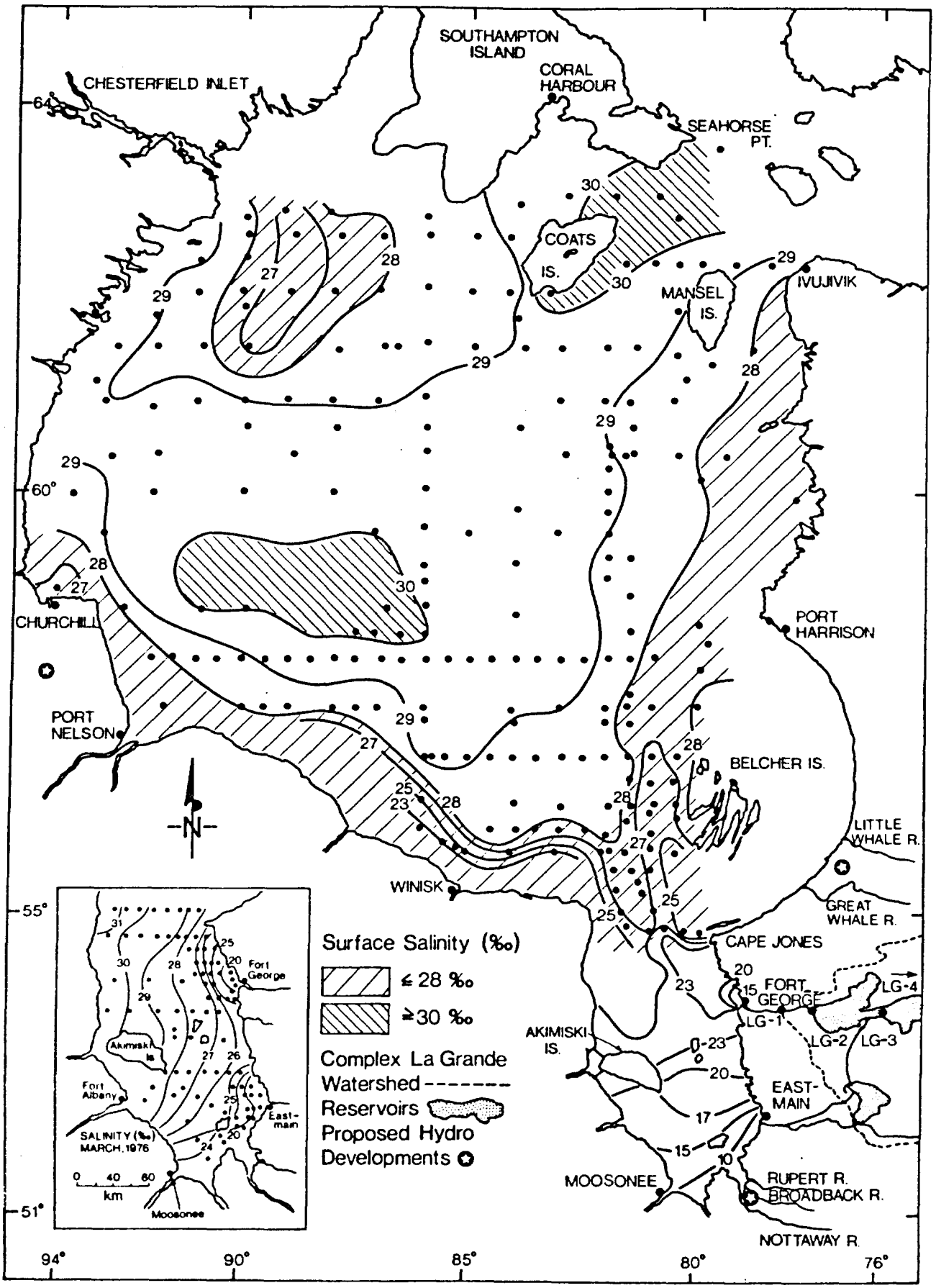

Fig.1 Surface salinity (^{o}/oo) features and hydroelectric developments in the Hudson-James Bay basin (modified from Prinsenberg, 1978)

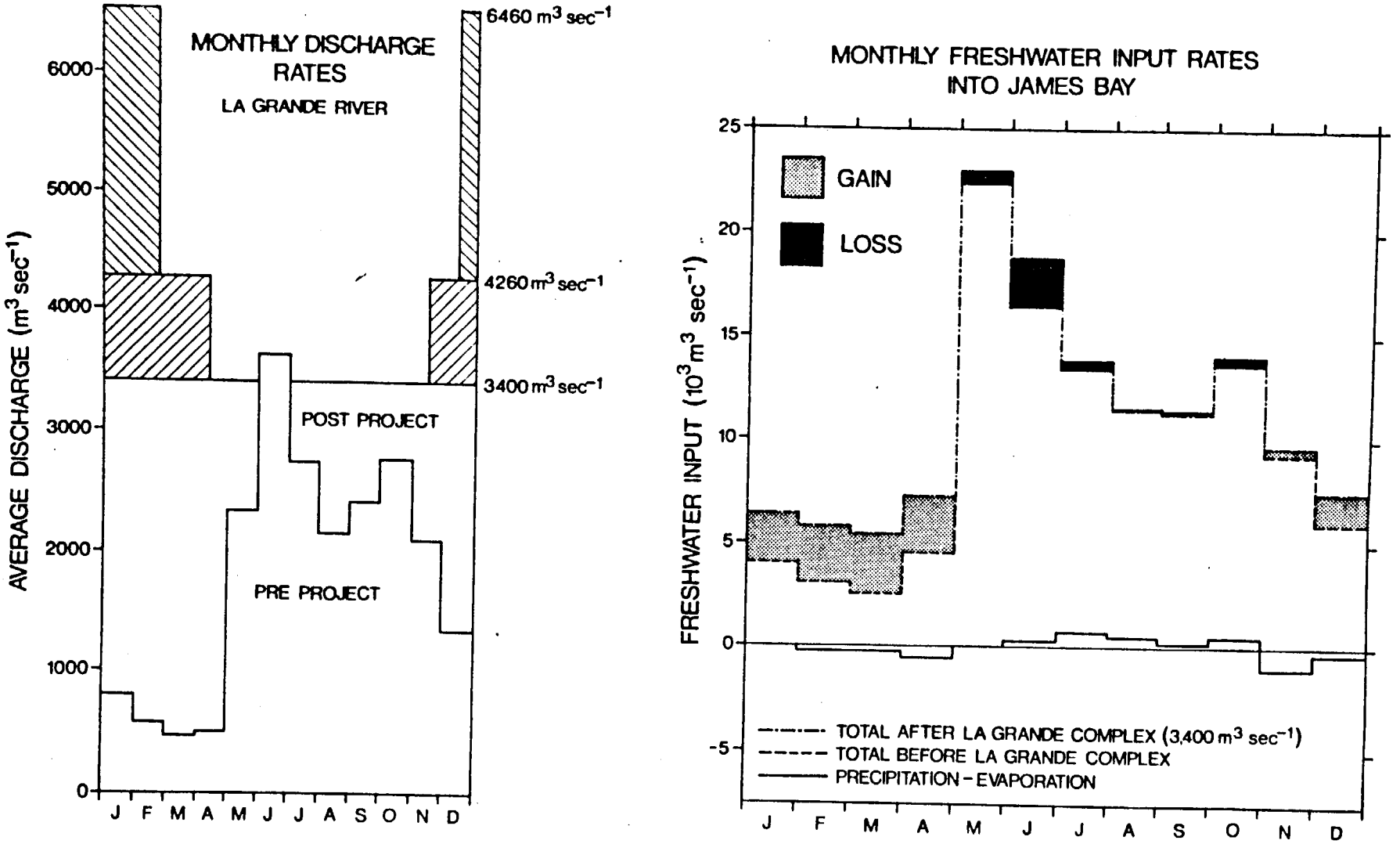

Fig.2 Present and future La Grande River discharges
(modified from Peck, 1976 and Prinsenberg, 1980)

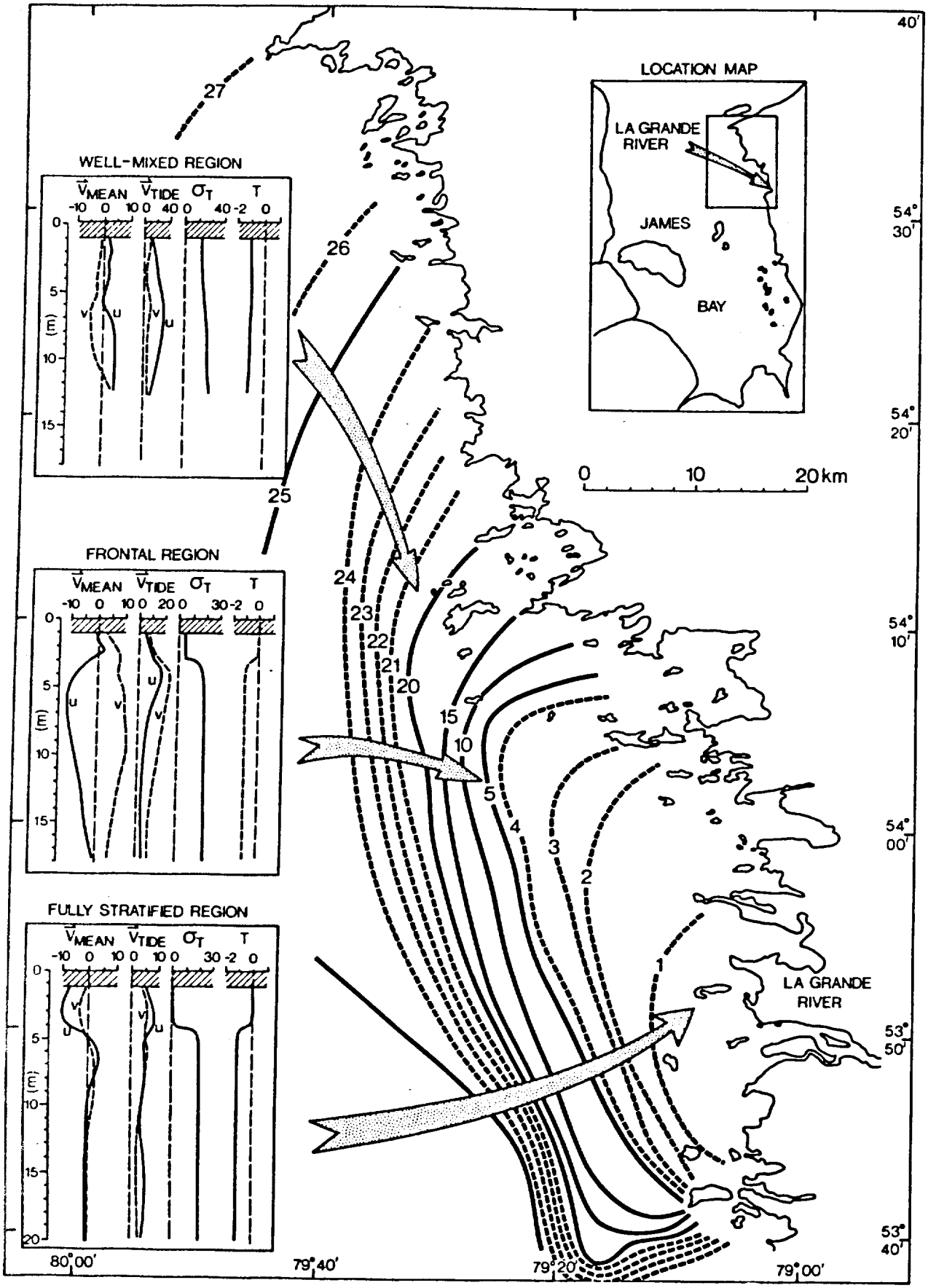

Fig.3 Surface salinity (°/oo) contours and averaged 25-hour profile data for period March 1-9, 1980

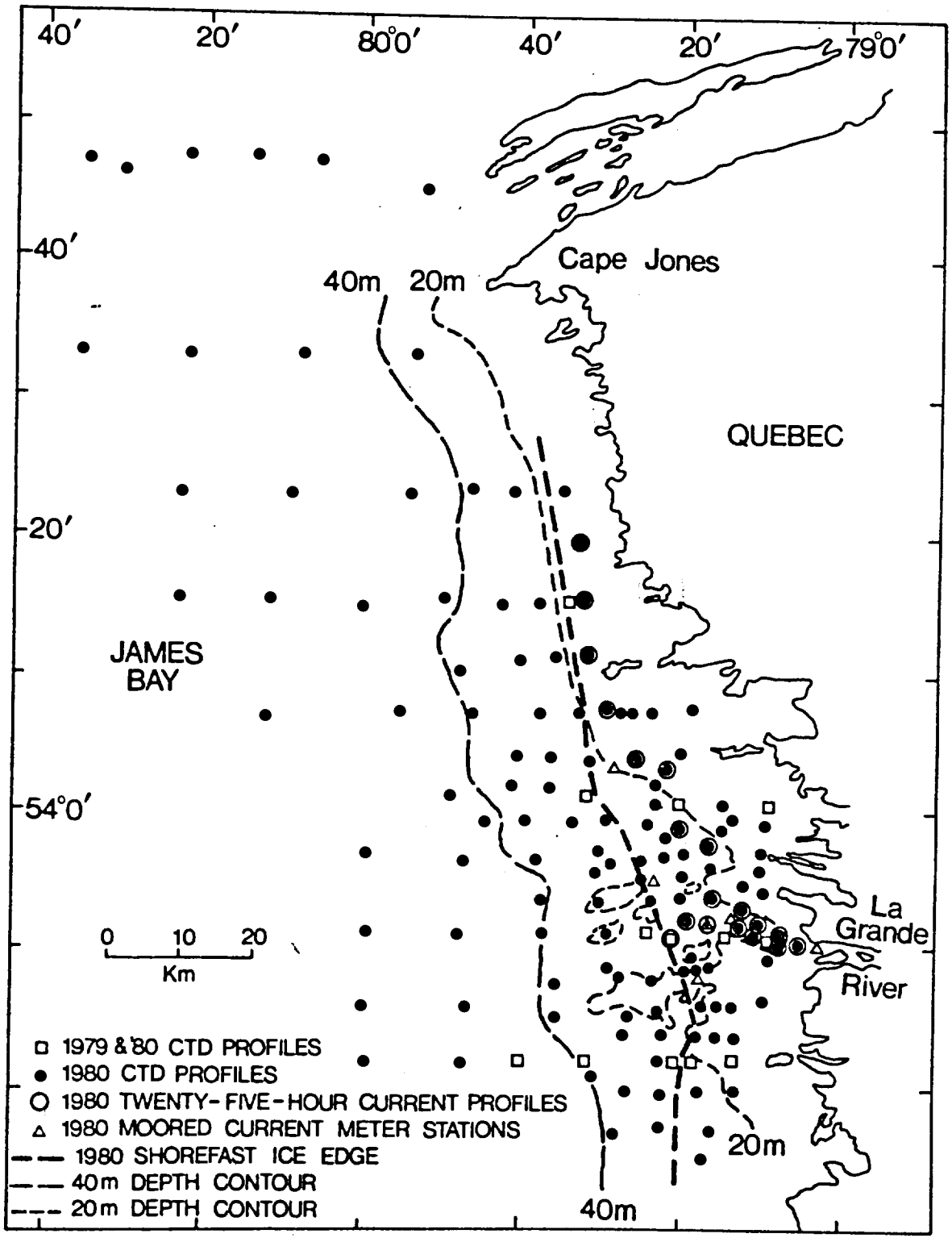

Fig.4 La Grande winter oceanographic stations (1979 and 1980)

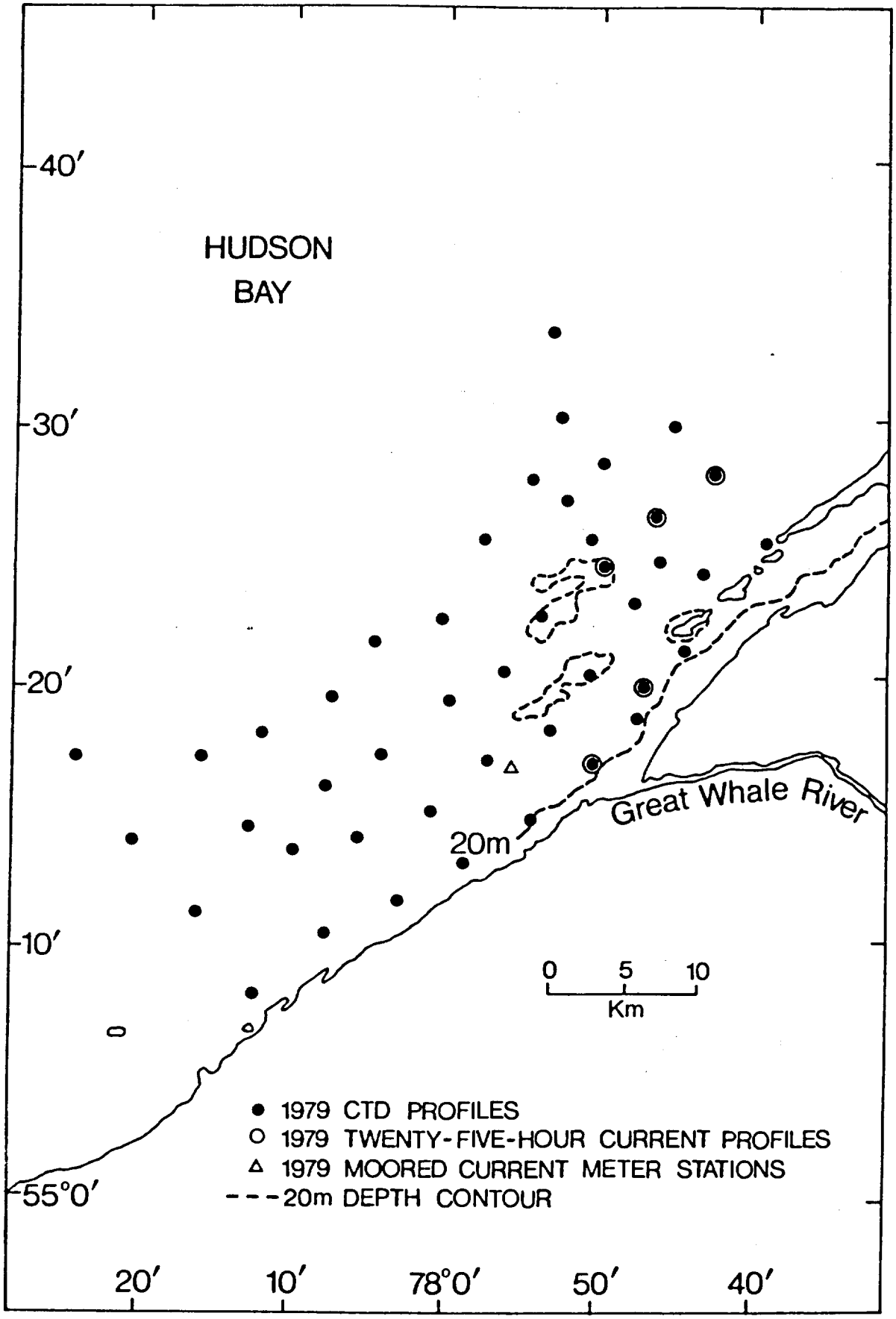

Fig.5 Great Whale winter oceanographic stations (1980)

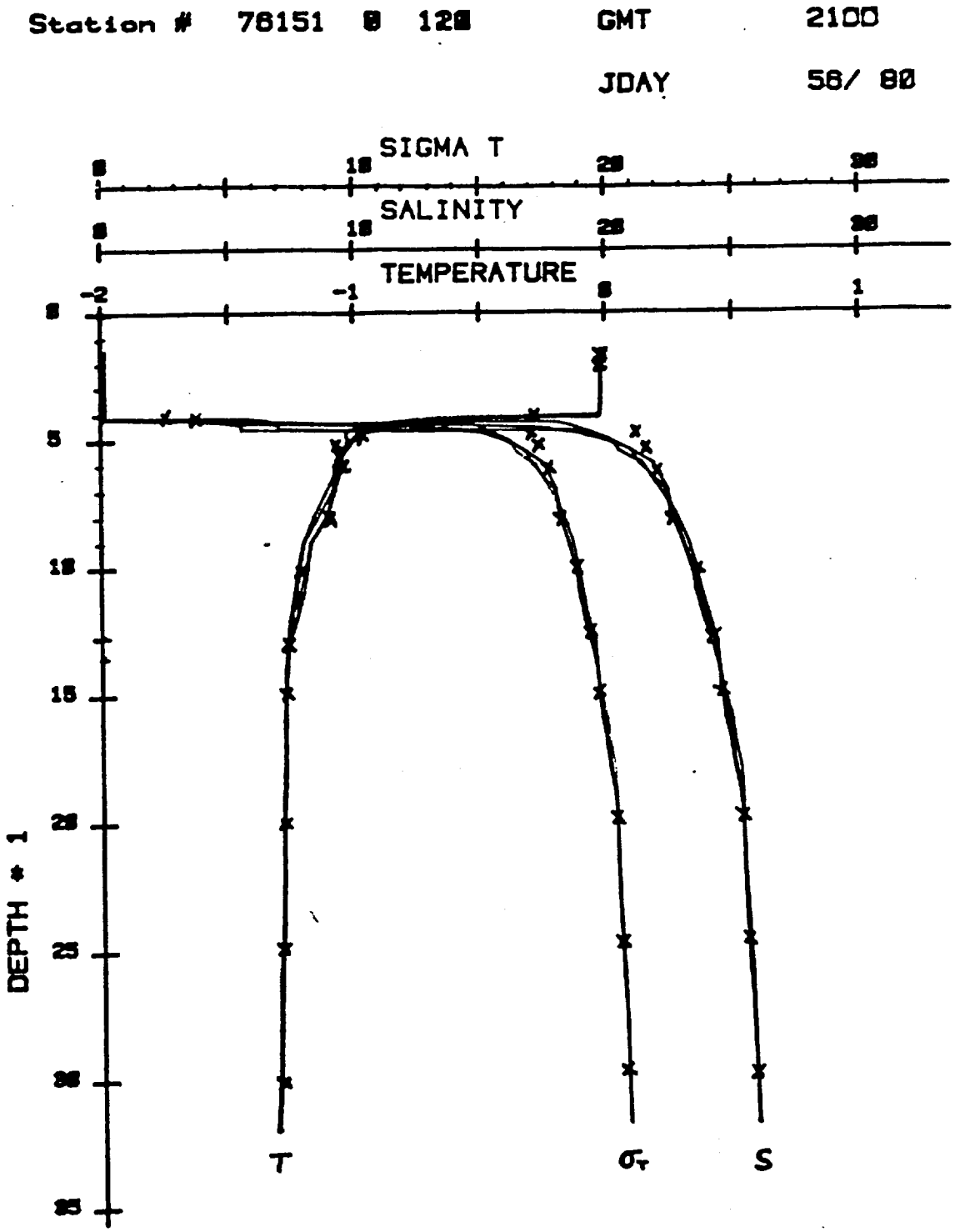

Fig.6 Salinity and temperature data from the Guildline Mark IV CTD probe (solid lines) and the modified Aanderaa 25-hour profiler (crosses)

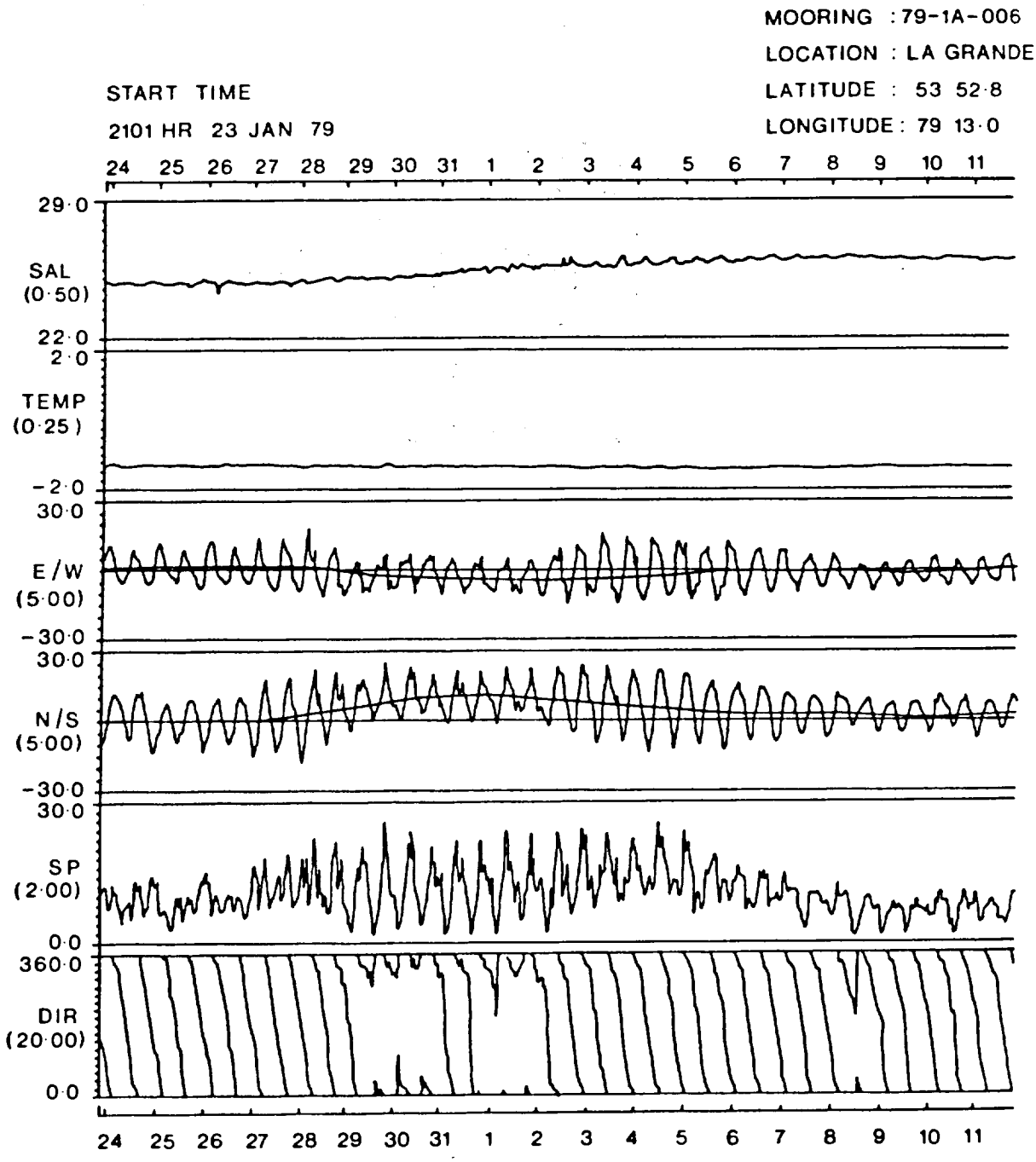

Fig.7 Partial record for current meter at 6m depth and approximately 9km off the mouth of the La Grande River in the winter of 1979

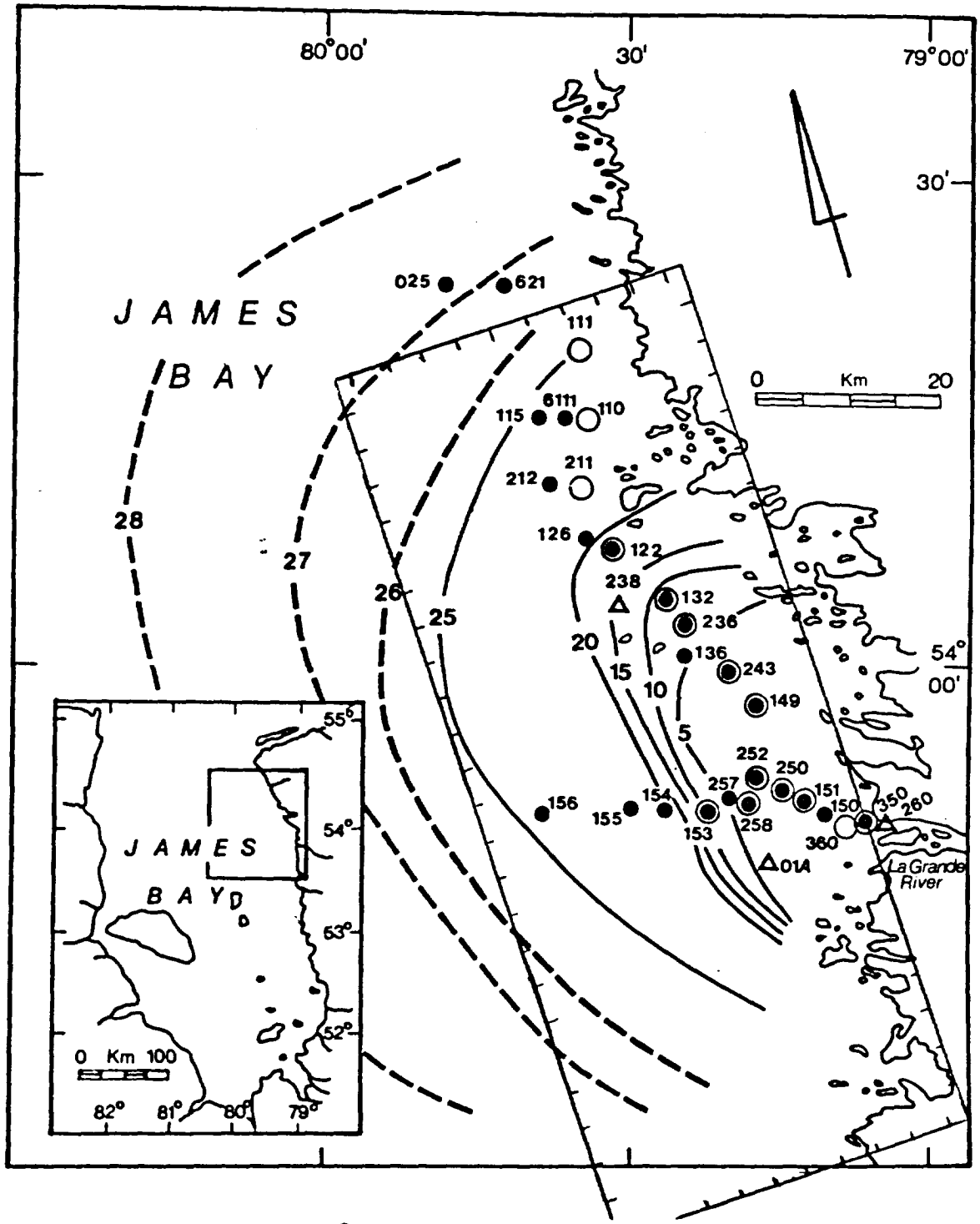

Fig.8 Surface salinity (^{0}/oo) distribution off La Grande during March 15-30, 1980. Station locations used in the subsequent analysis: ●CTD profiles, ⊙25-hour current profiles, Δcurrent meter moorings

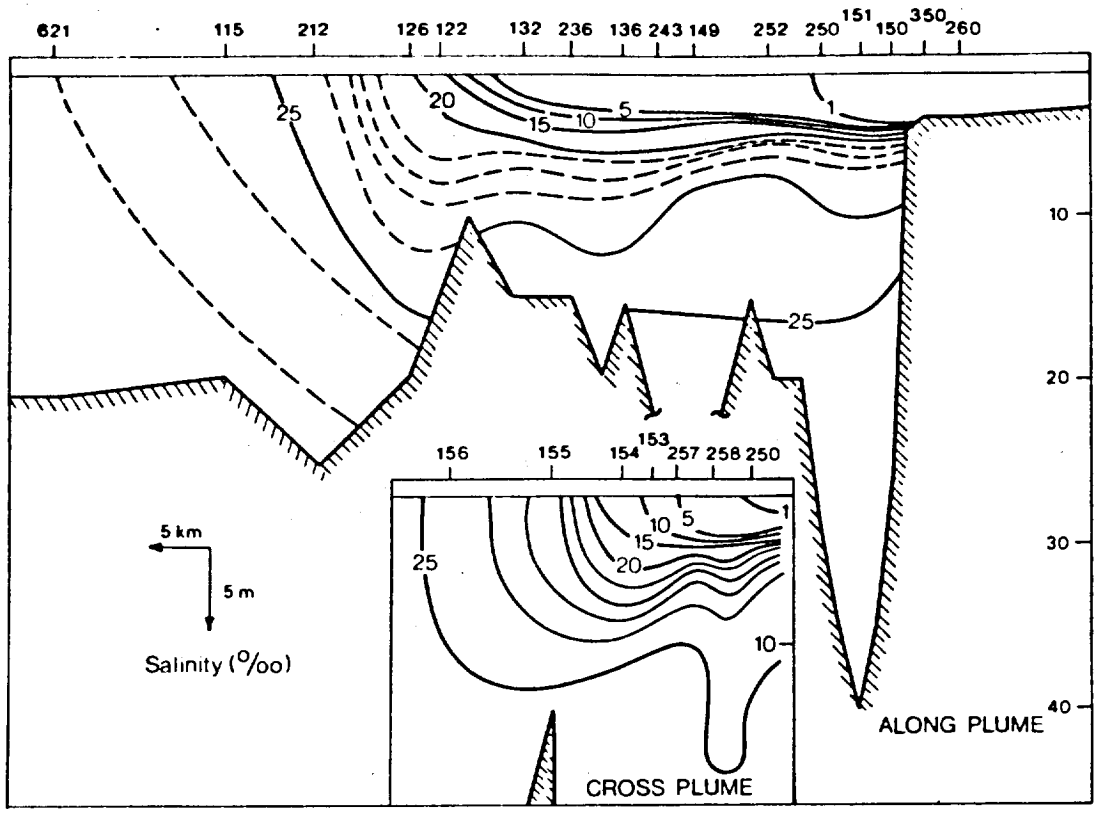

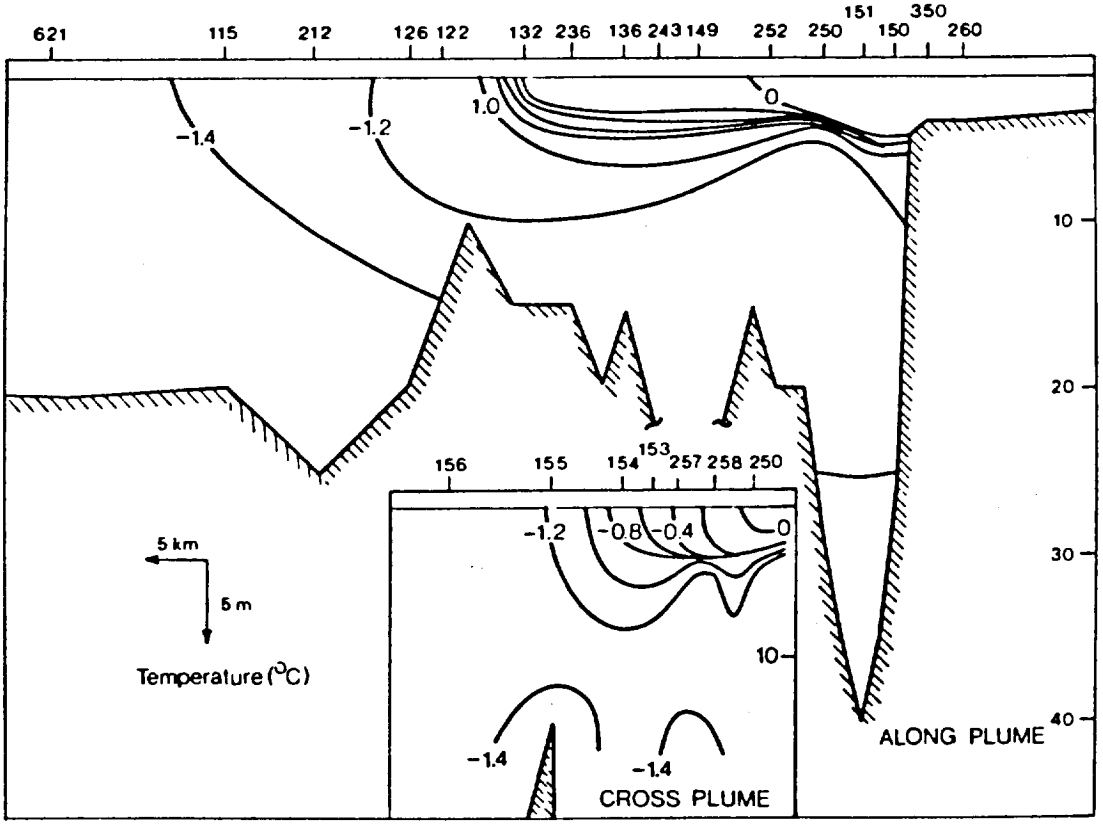

Fig.9 Salinity (°/oo) and temperature (°C) sections along and across the plume axis from March 1-9, 1980.

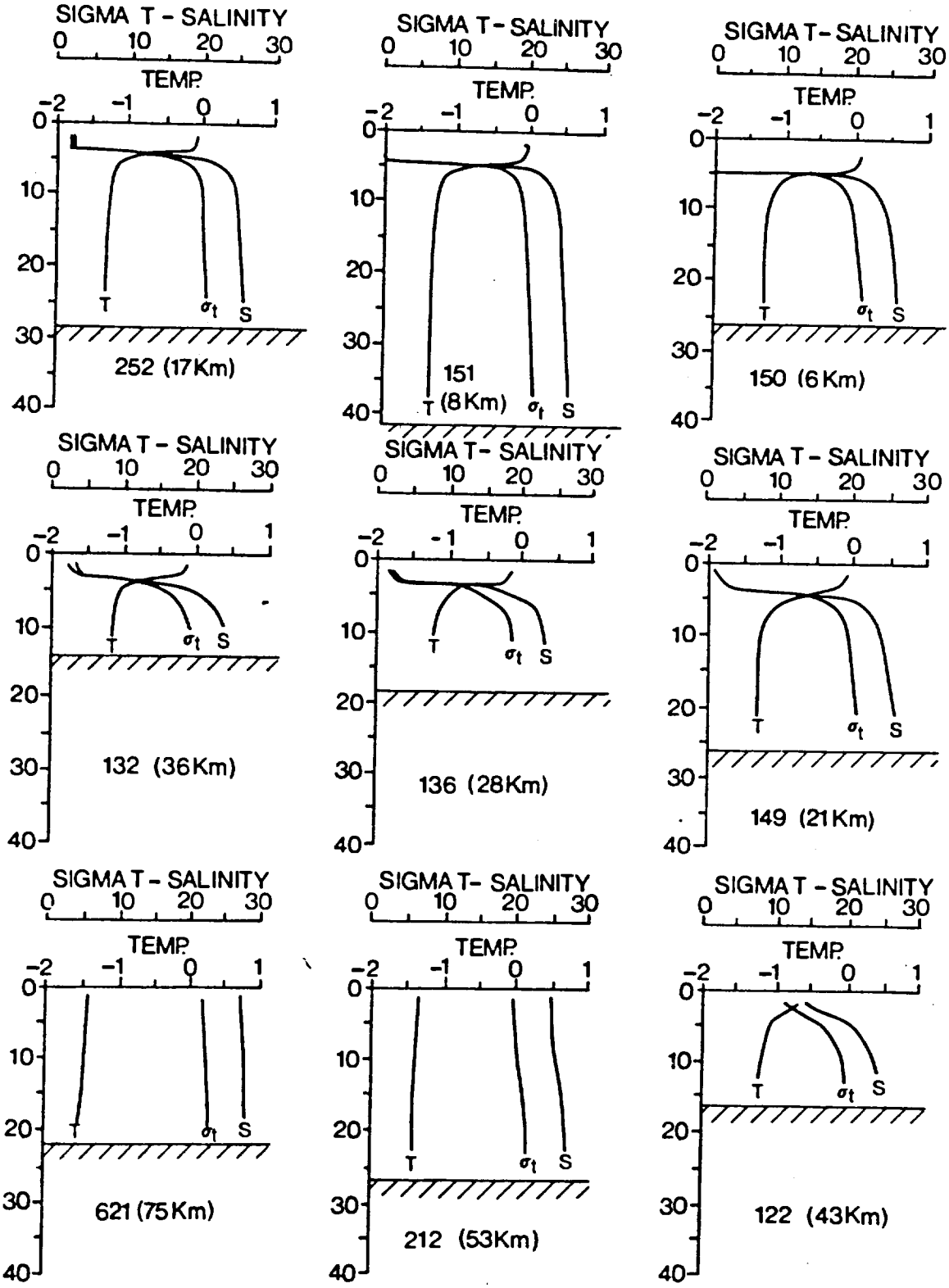

Fig.10 Salinity (^{o}/oo), temperature (^{o}C) and sigma-t profiles at selected stations along the plume axis.

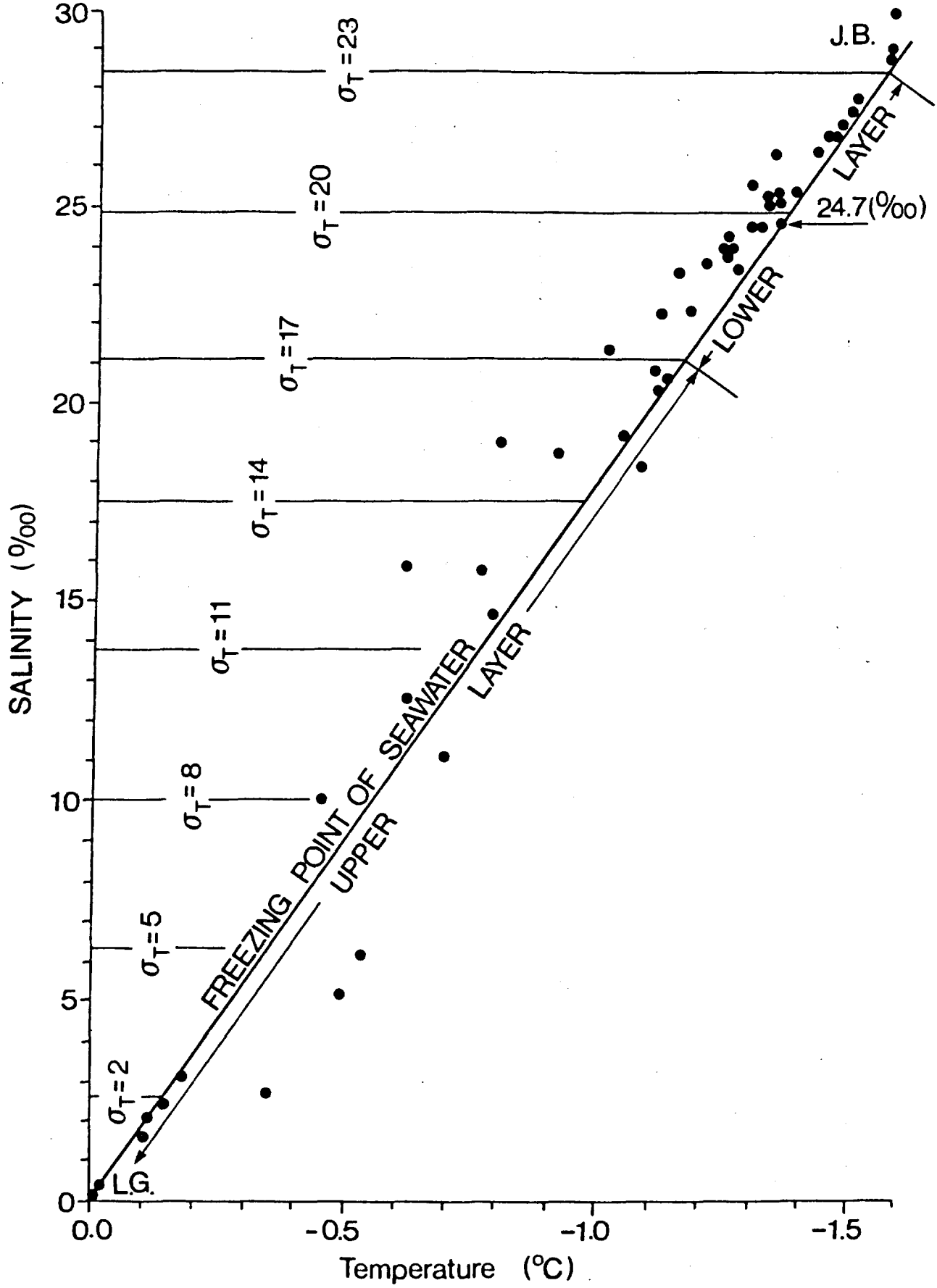

Fig.11 T-S diagram for data discretized from Fig. 10.

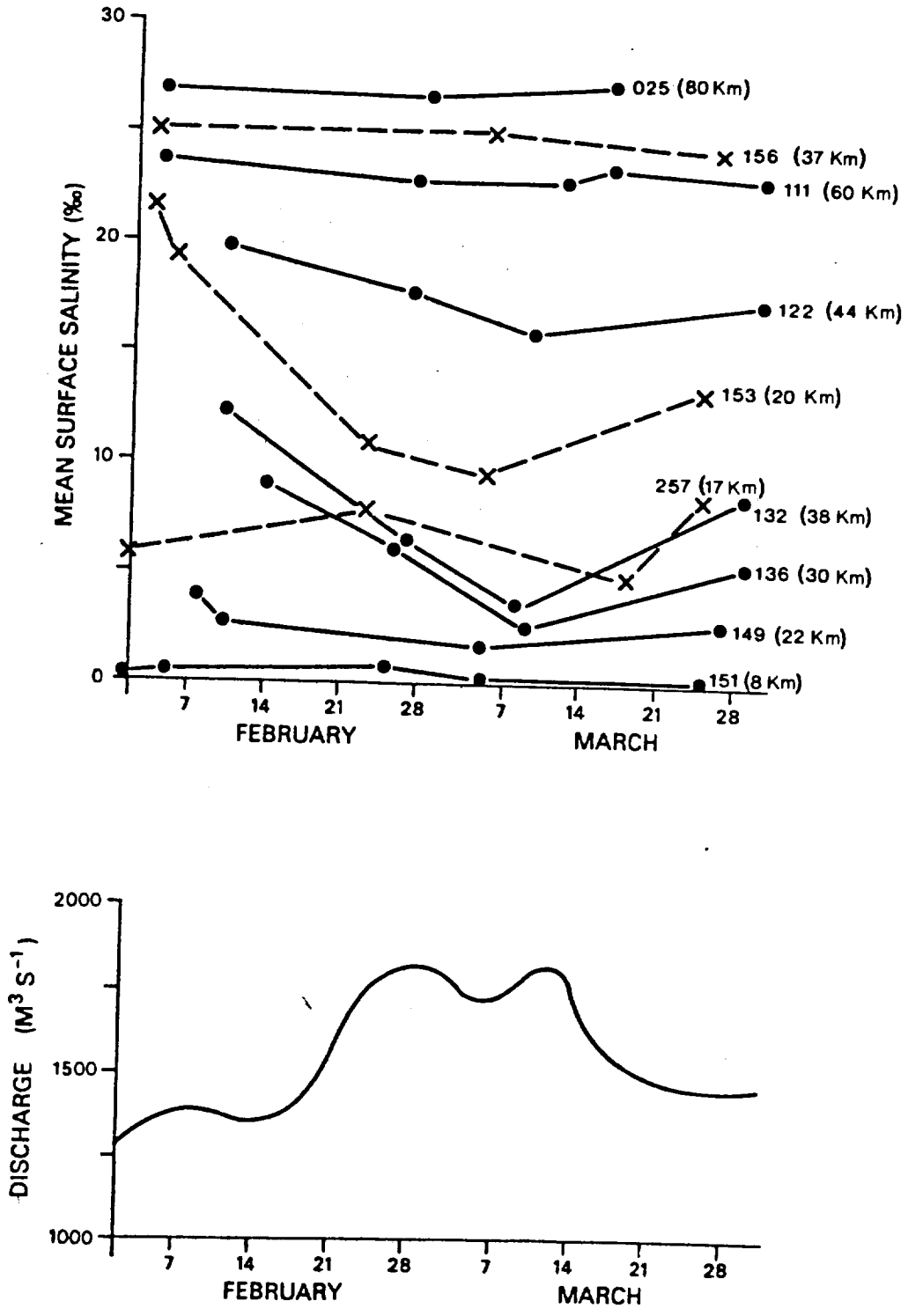

Fig.12 Temporal variations in La Grande River discharge and mean surface salinity at selected stations along the plume (0-0) and across the plume (X-X) axes.

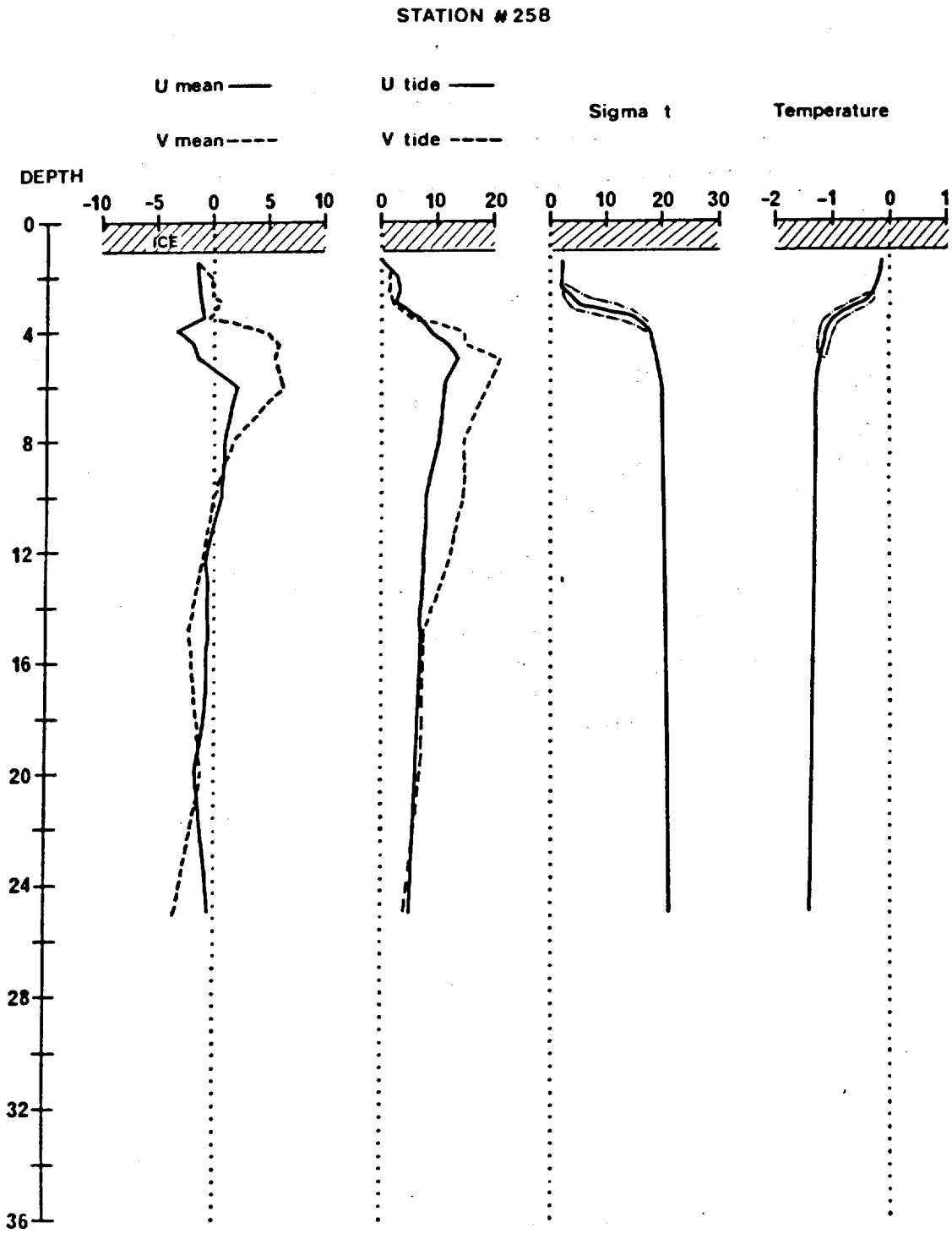

Fig.13 Vertical profile plot obtained by averaging the hourly Aanderaa profiler data at station 0258 over a diurnal tidal period. U(cm sec^{-1}) is toward the east and V (cm sec^{-1}) is toward the north (true). Temperature is in ^{o}C.

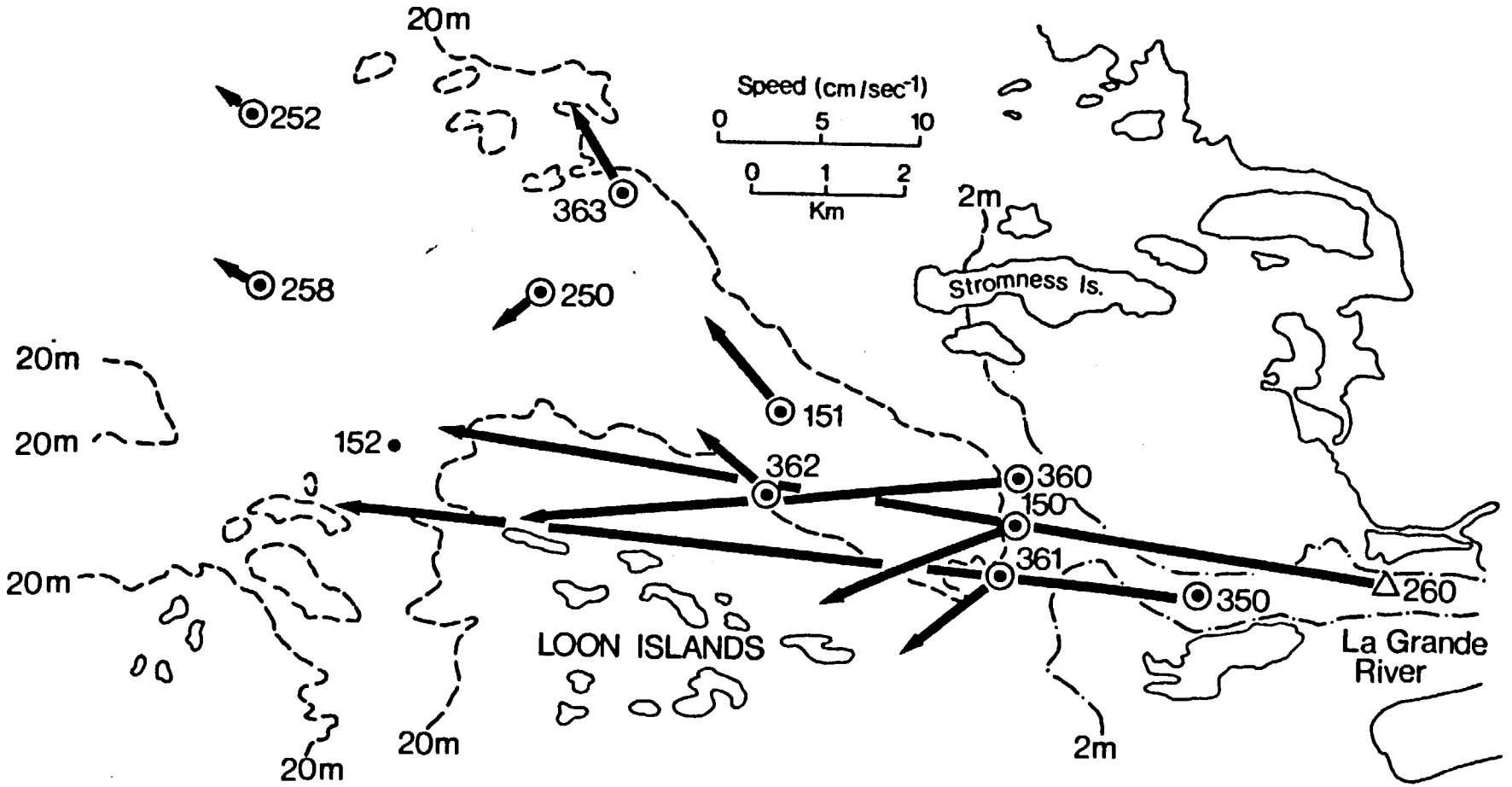

Fig.14 Surface current vectors off the mouth of the La Grande River over the period of Feb. 7 - March 26, 1980.

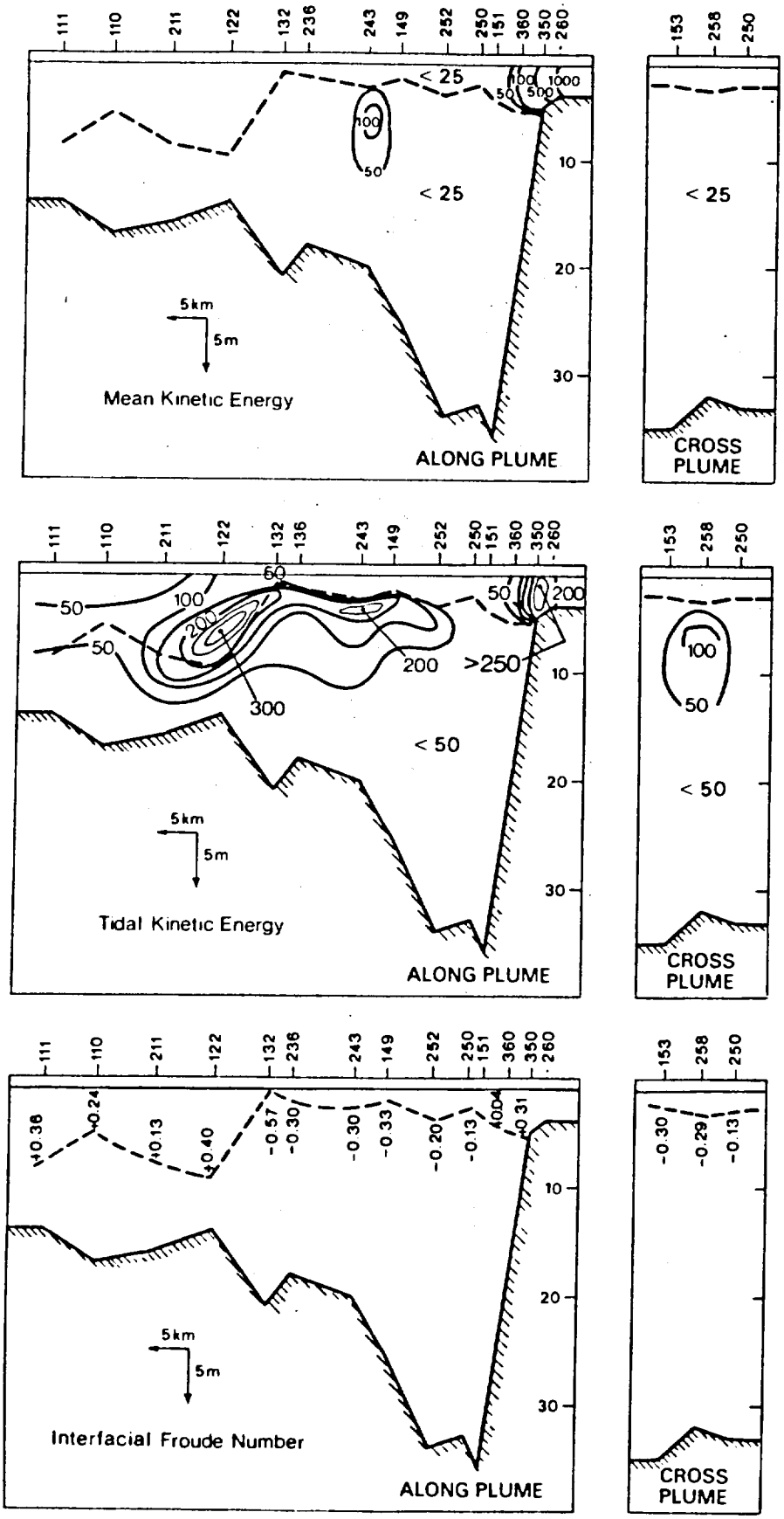

Fig.15 Contours of mean and tidal kinetic energy and interfacial Froude number. Heavy dashed line delineates the pycnocline.

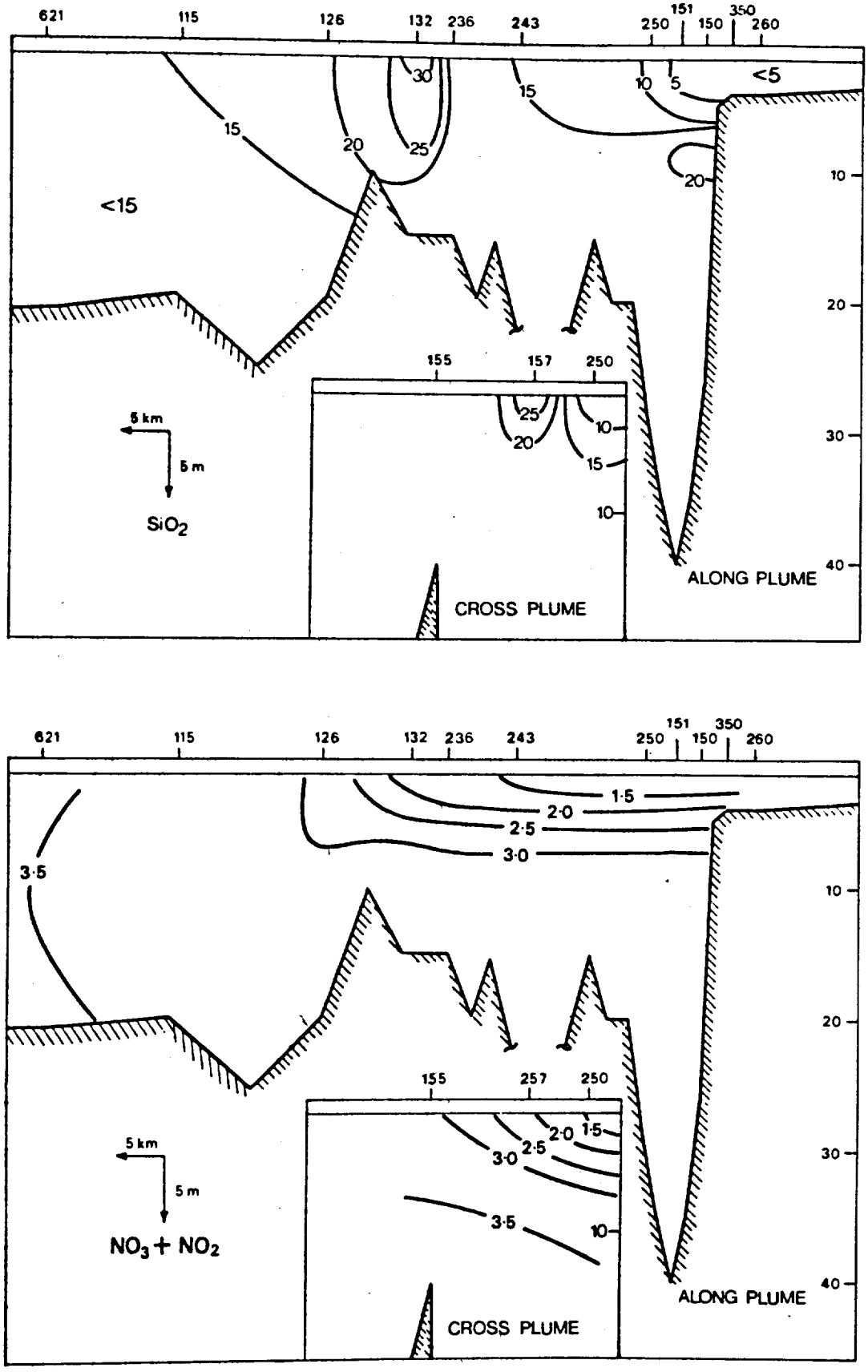

Fig. 16 Reactive silicate (SiO_2) and nitrate plus nitrite ($NO_3 + NO_2$) sections (μg-at. ℓ^{-1}); reproduced by permission of Dr. J.C. Roff, University of Guelph.

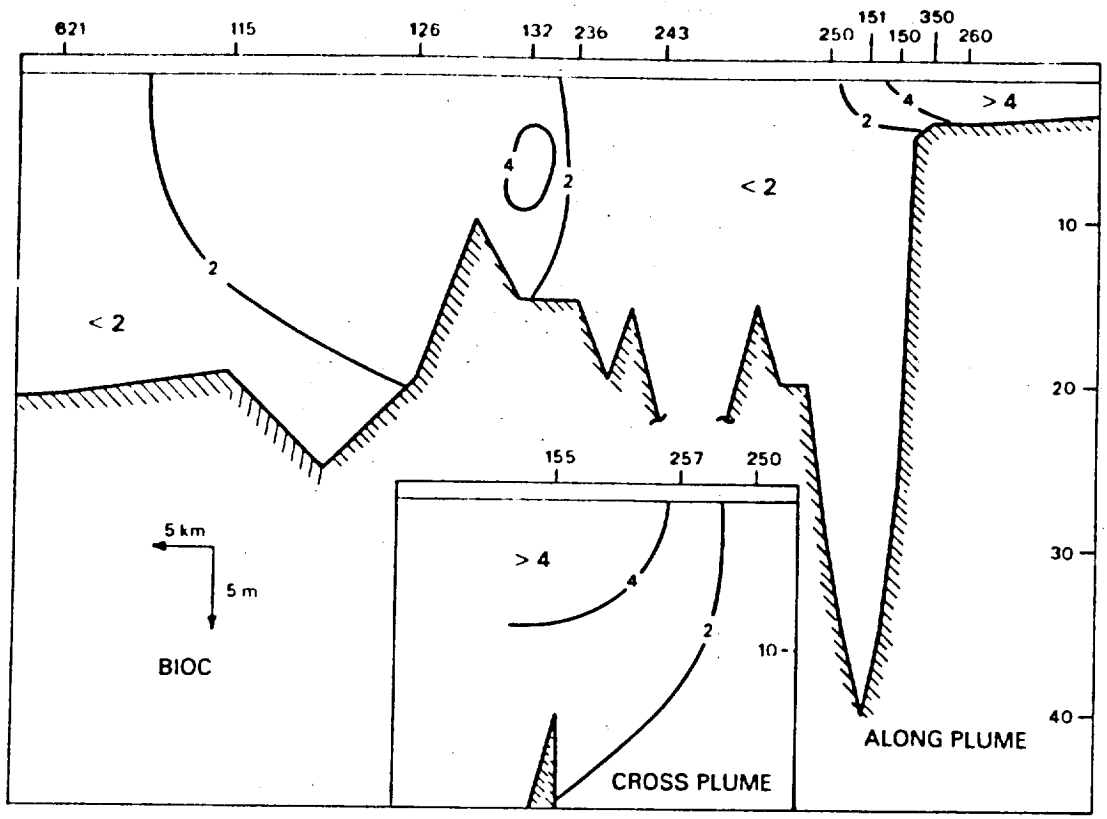

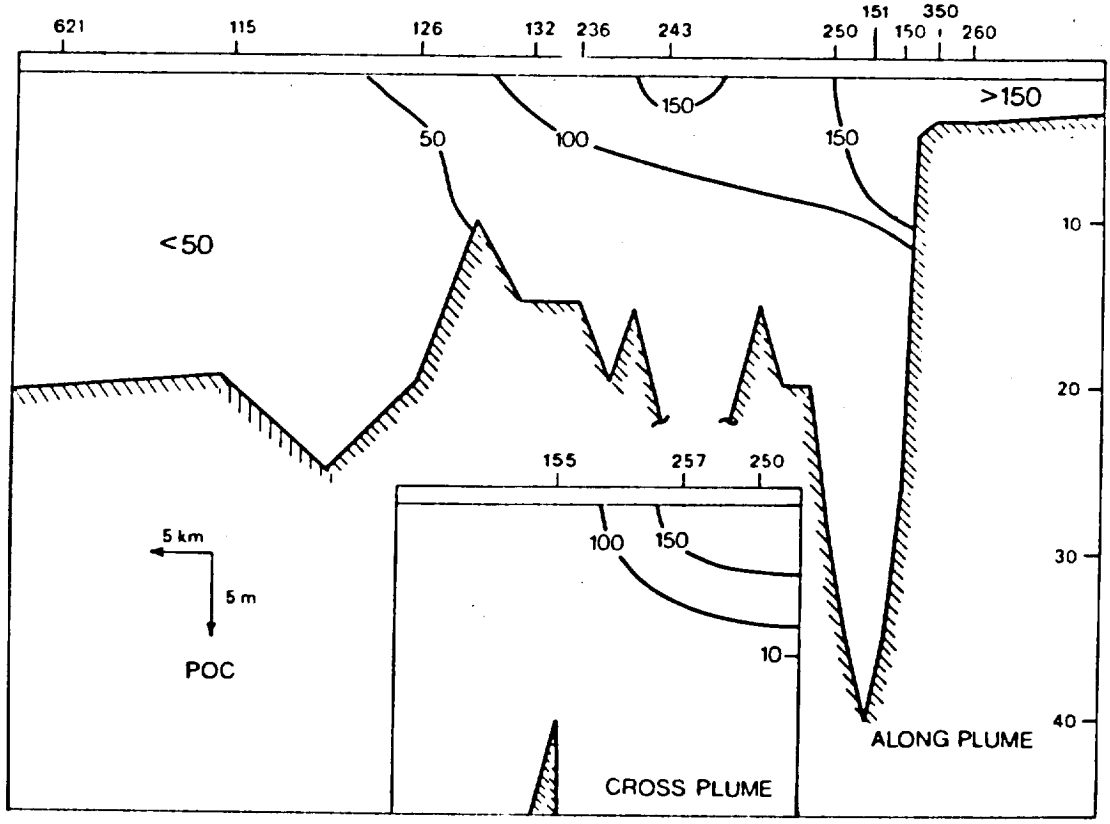

Fig.17 Biocarbon (BIOC = ATP x 250) and particulate organic carbon (POC) sections (µg ℓ^{-1}); reproduced by permission of Dr. J.C. Roff, University of Guelph.

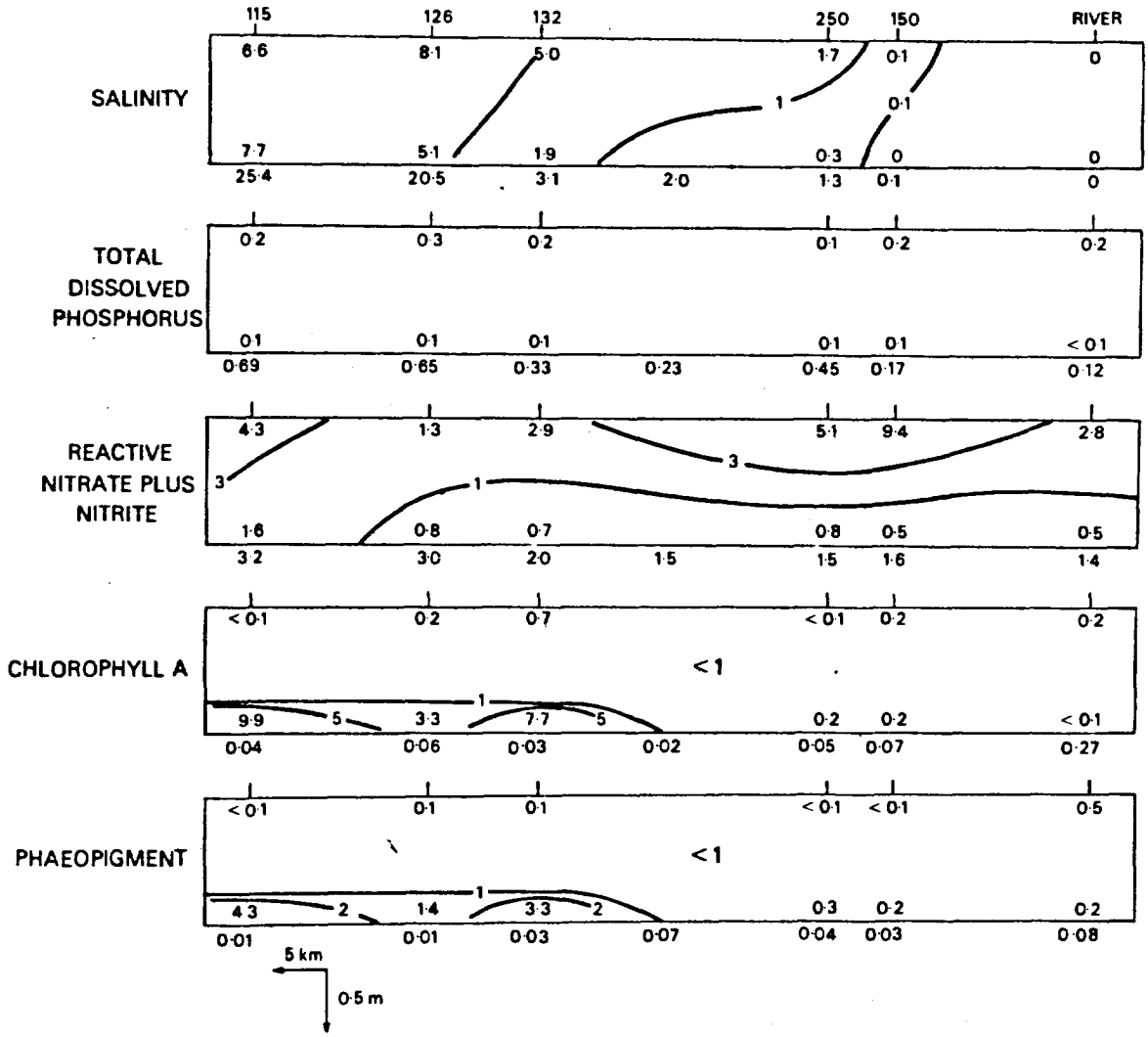

Fig.18 Chemical and biological data from ice samples along the plume axis. Units are: salinity ($^{o}/oo$); TDP & NO_3 + NO_2 ($\mu g\text{-at } \ell^{-1}$); chlorophyll a and phaeopigments ($\mu g\ \ell^{-1}$); reproduced by permission of Dr. J.C. Roff, University of Guelph.

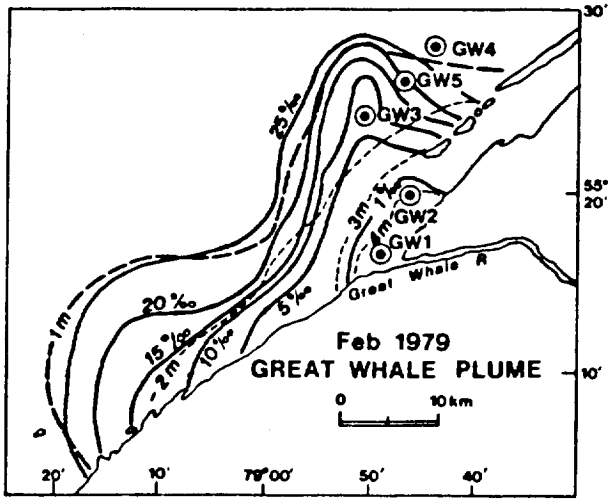

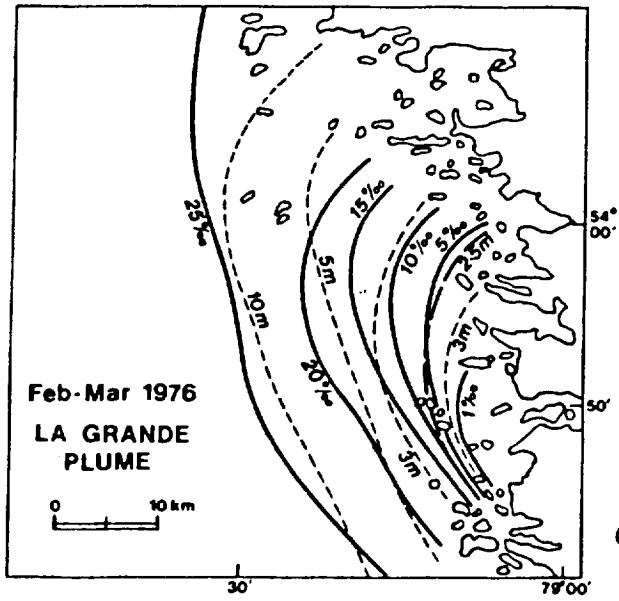

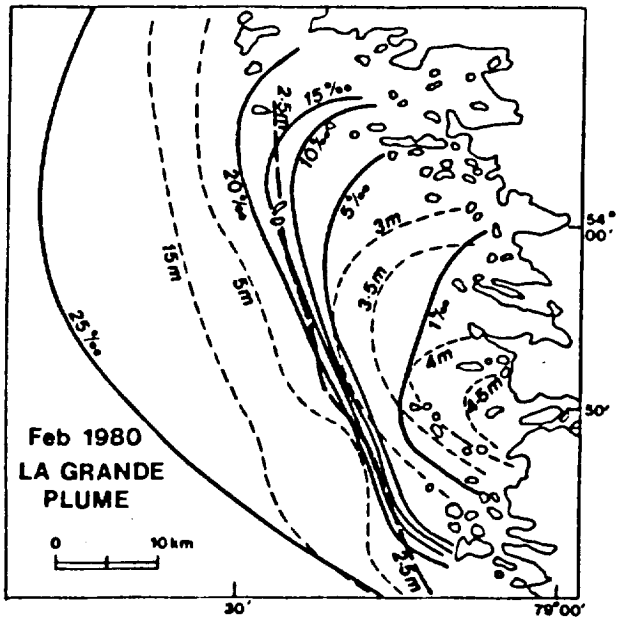

Fig.19 Surface distributions plotted for three different plume configurations:

(a) Gt. Whale winter 79:
discharge = 200 m^3 sec^{-1}
kinetic energy = 25 cm^2 sec^{-2}

(b) La Grande winter 76:
discharge = 500 m^3 sec^{-1};
kinetic energy = 300 cm^2 sec^{-2}

(c) La Grande March 15-30, 1980:
discharge = 1,600 m^3 sec^{-1};
kinetic energy = 300 cm^2 sec^{-2}

Contours: salinity (^{o}/oo) ——;
pycnocline depth ----;
min. pycnocline depth — —;
twenty-five-hour stations ⊖.

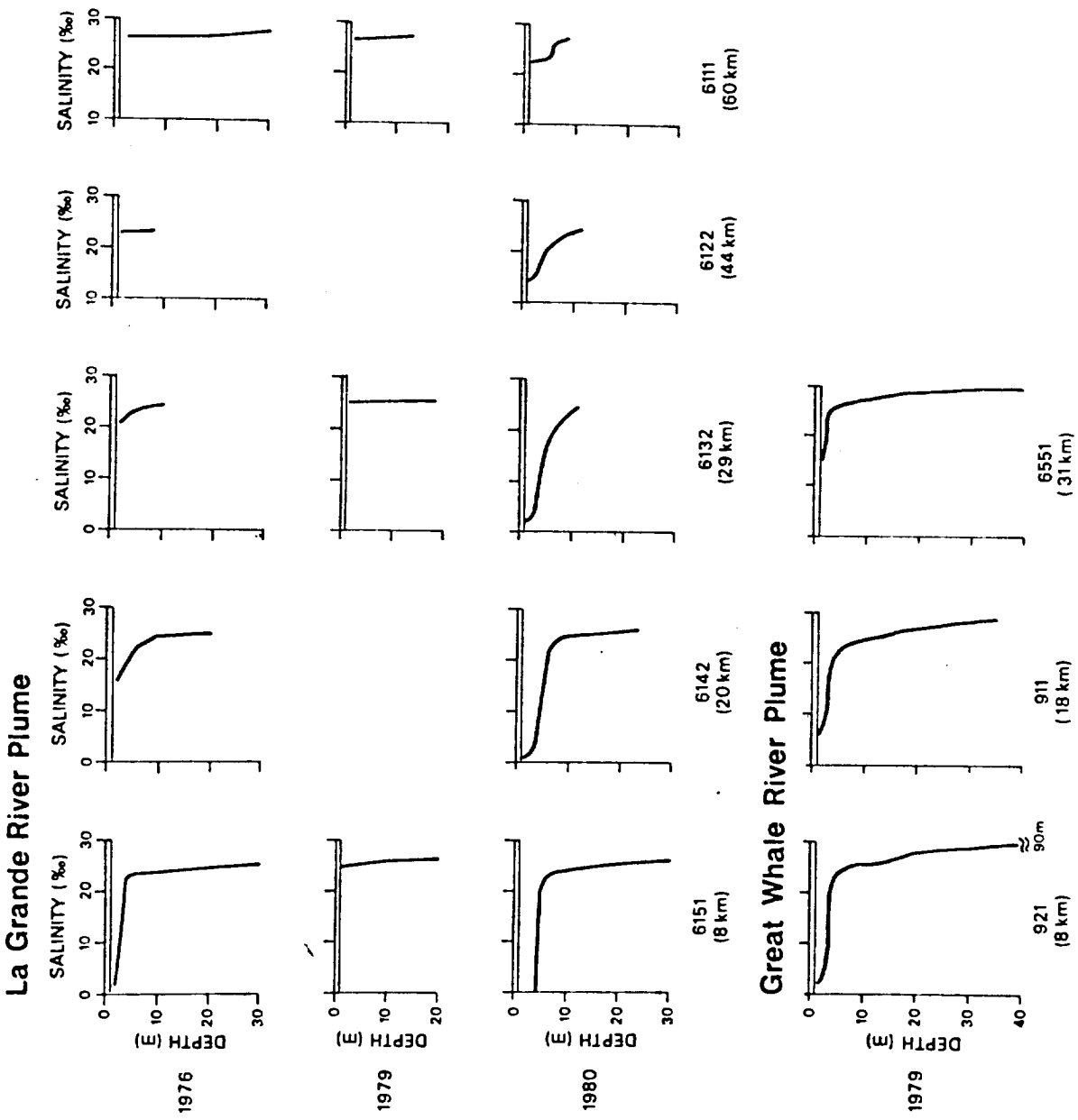

Fig. 20 Conductivity-Temperature-Depth (CTD) profiles for resurveyed stations at similar distances from the river mouth.

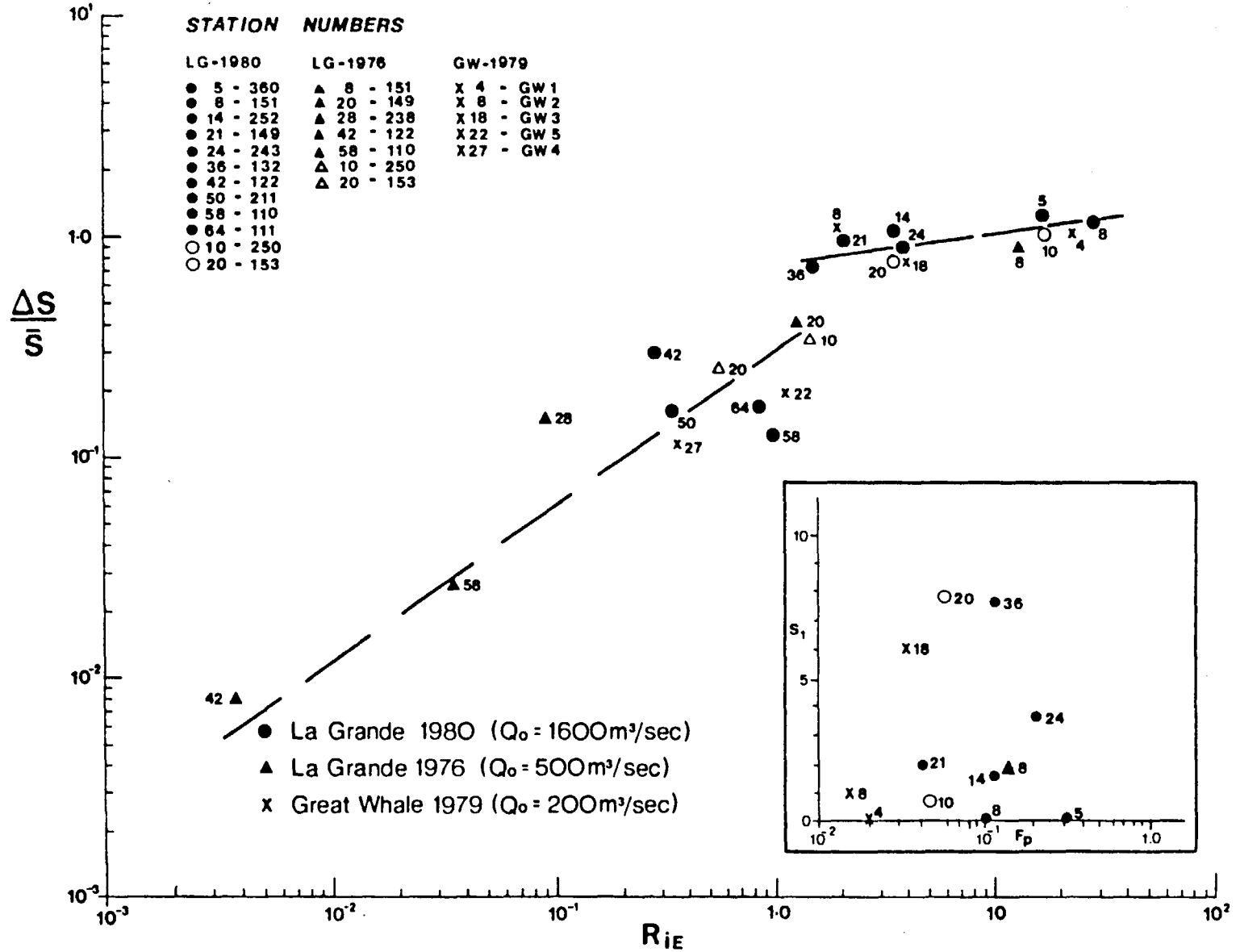

Fig.21 Inverse mixing parameter ($\Delta S/\bar{S}$) versus estuarine Richardson number (R_{iE}). The insert shows salinity (S) plotted against plume densimetric Froude number (F_p). Symbols: ● 5-360 represents a station location along the plume axis 5 km from the river mouth and designated number 360 in Fig. 8; ○ represents a cross plume station.

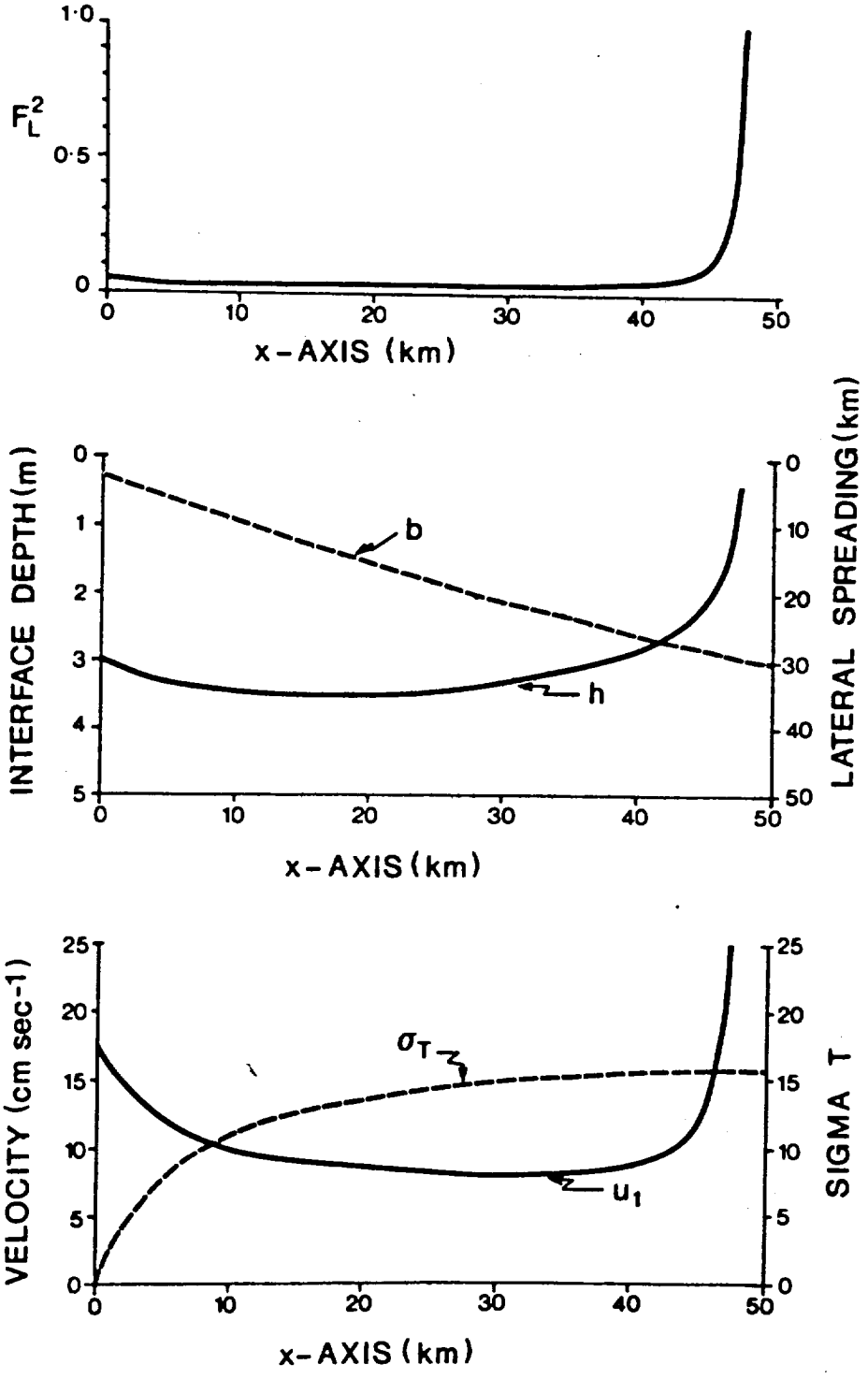

Fig. 22 Far-field integral model results for downward entrainment.

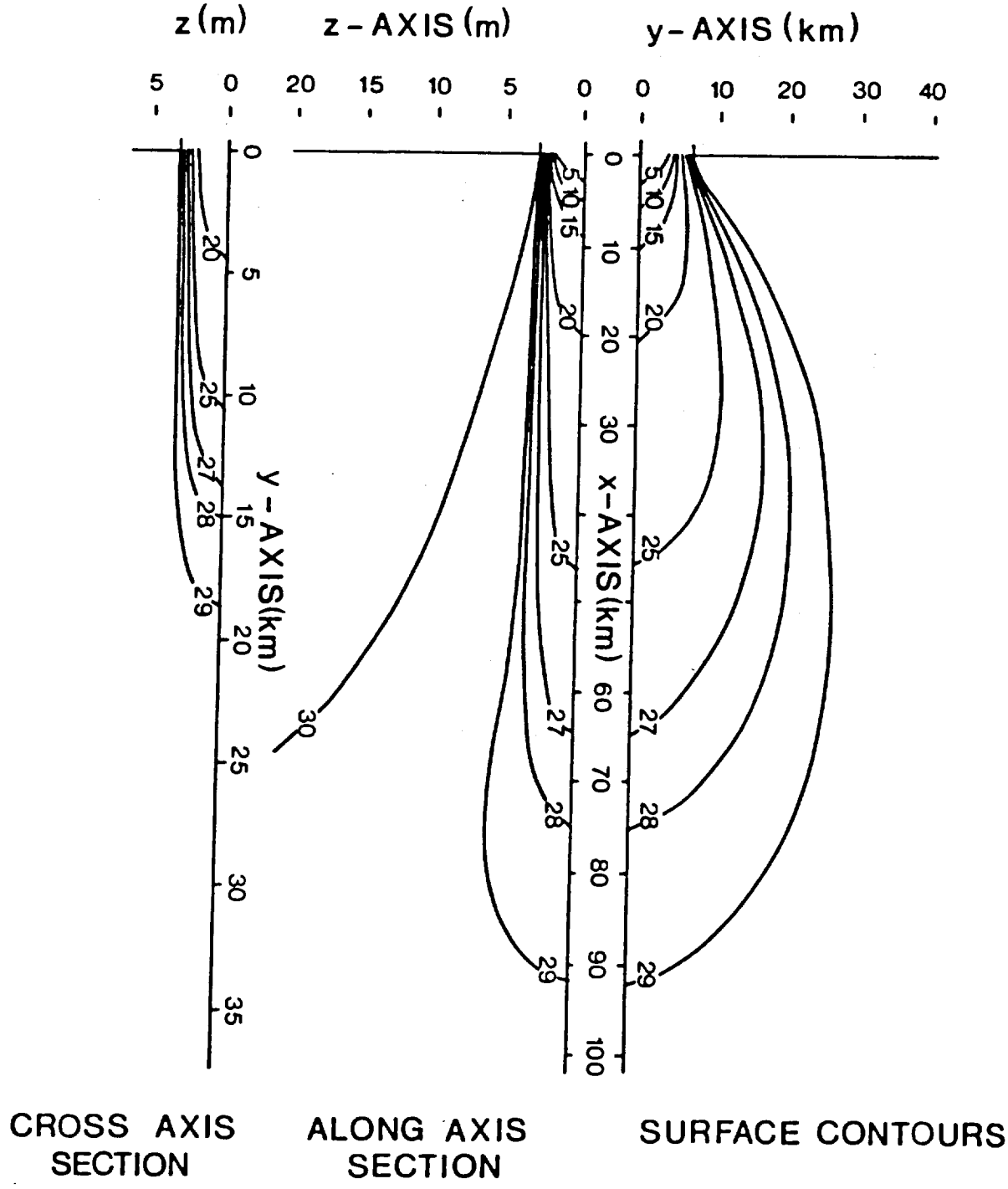

Fig.23 Far-field analytical model results with the Munk-Anderson Richardson number relationship for vertical diffusion. Salinity contours in °/oo. Note the cross plume scale expansion.

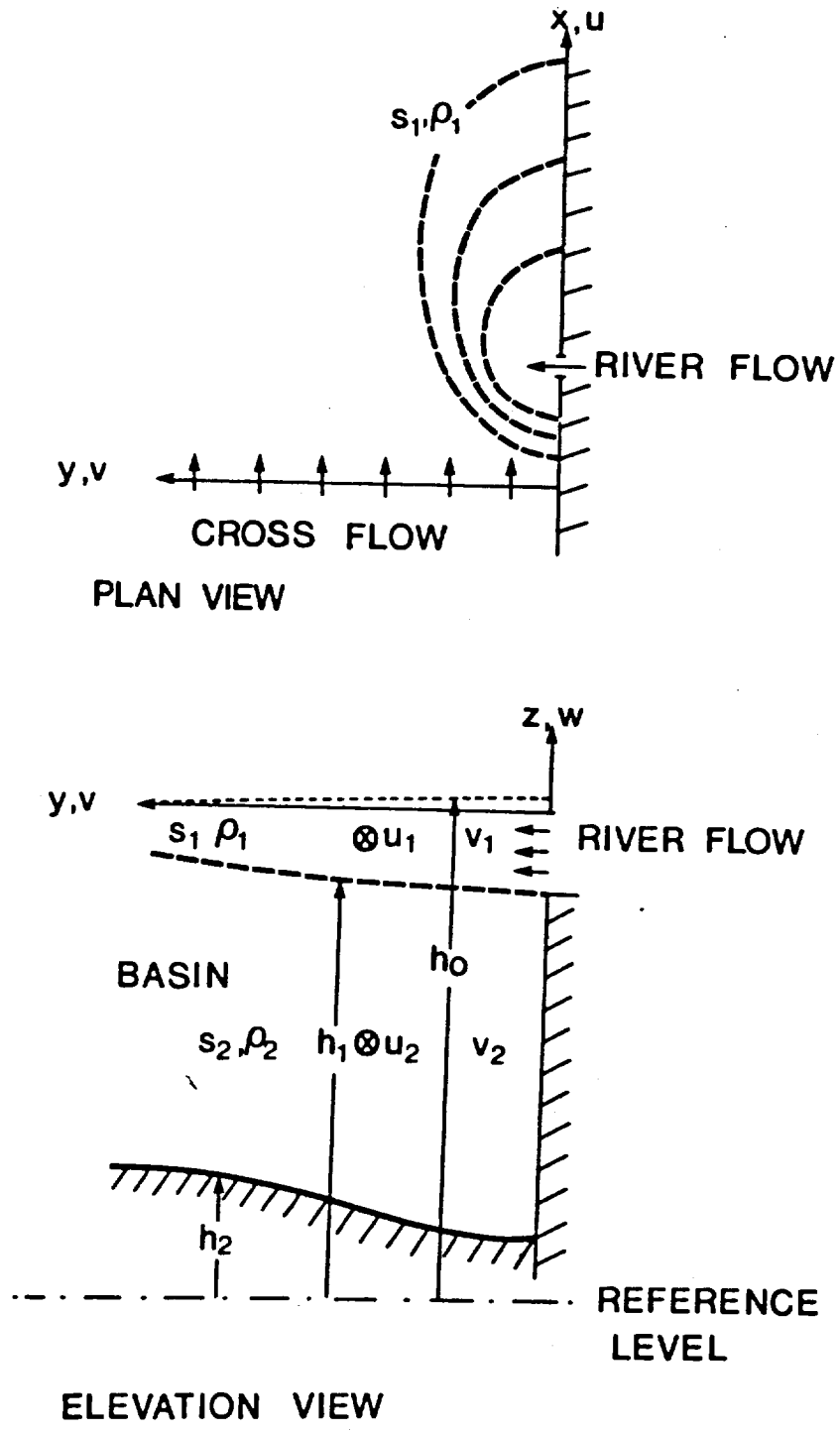

Fig.24 Two-layer numerical model definition diagram.

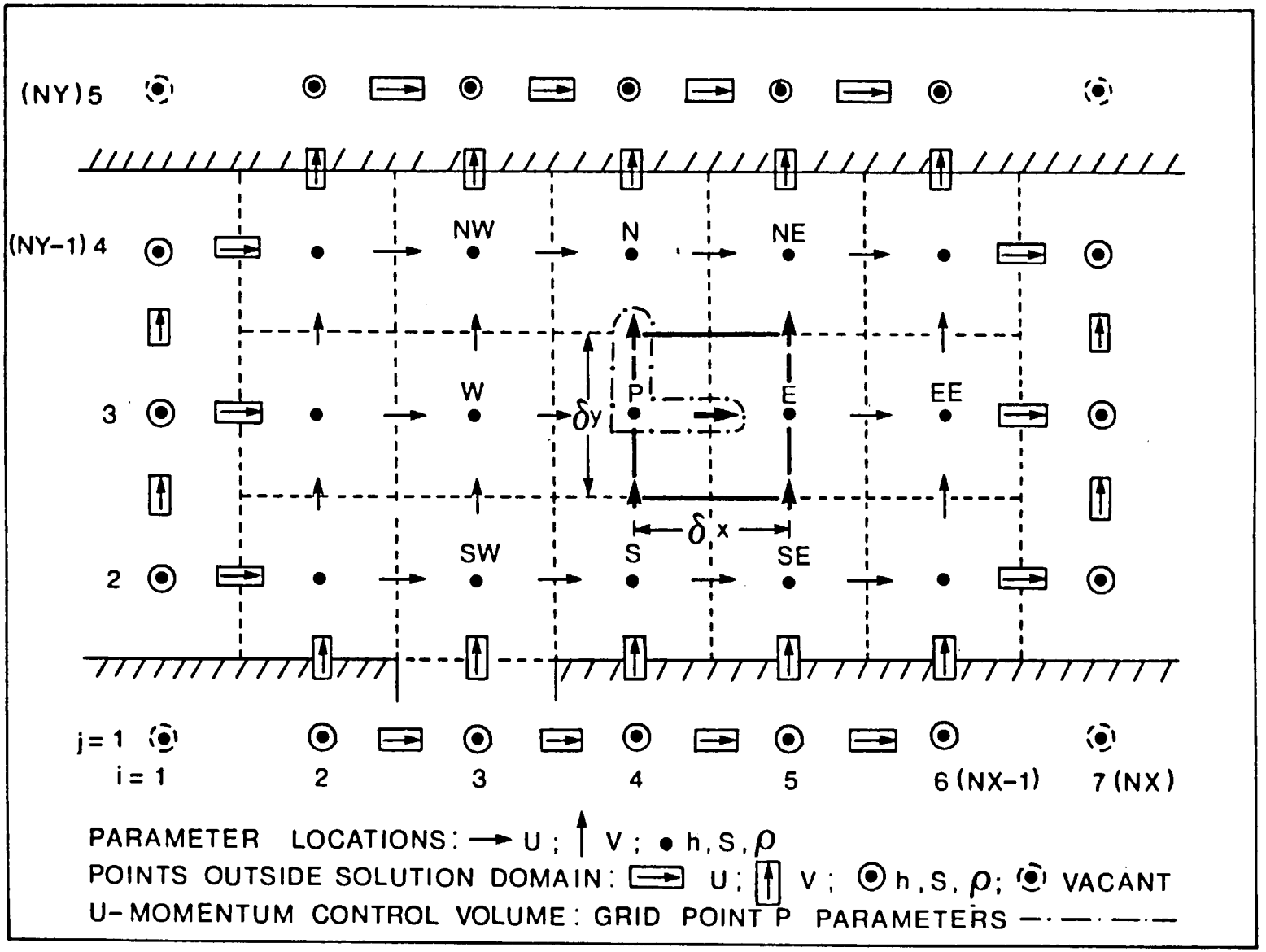

Fig.25 Finite-difference grid definition diagram.

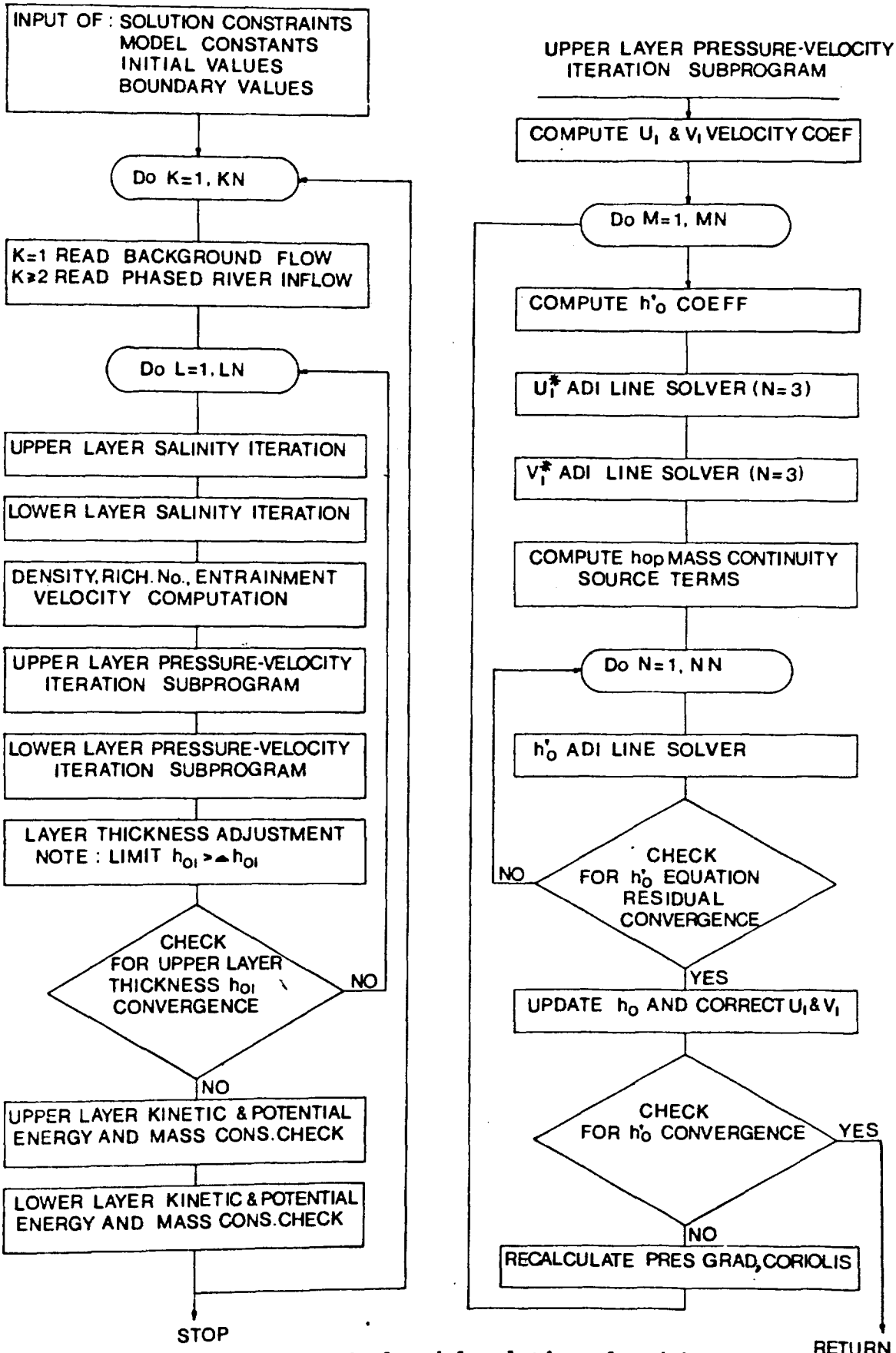

Fig.26 Numerical model solution algorithm.

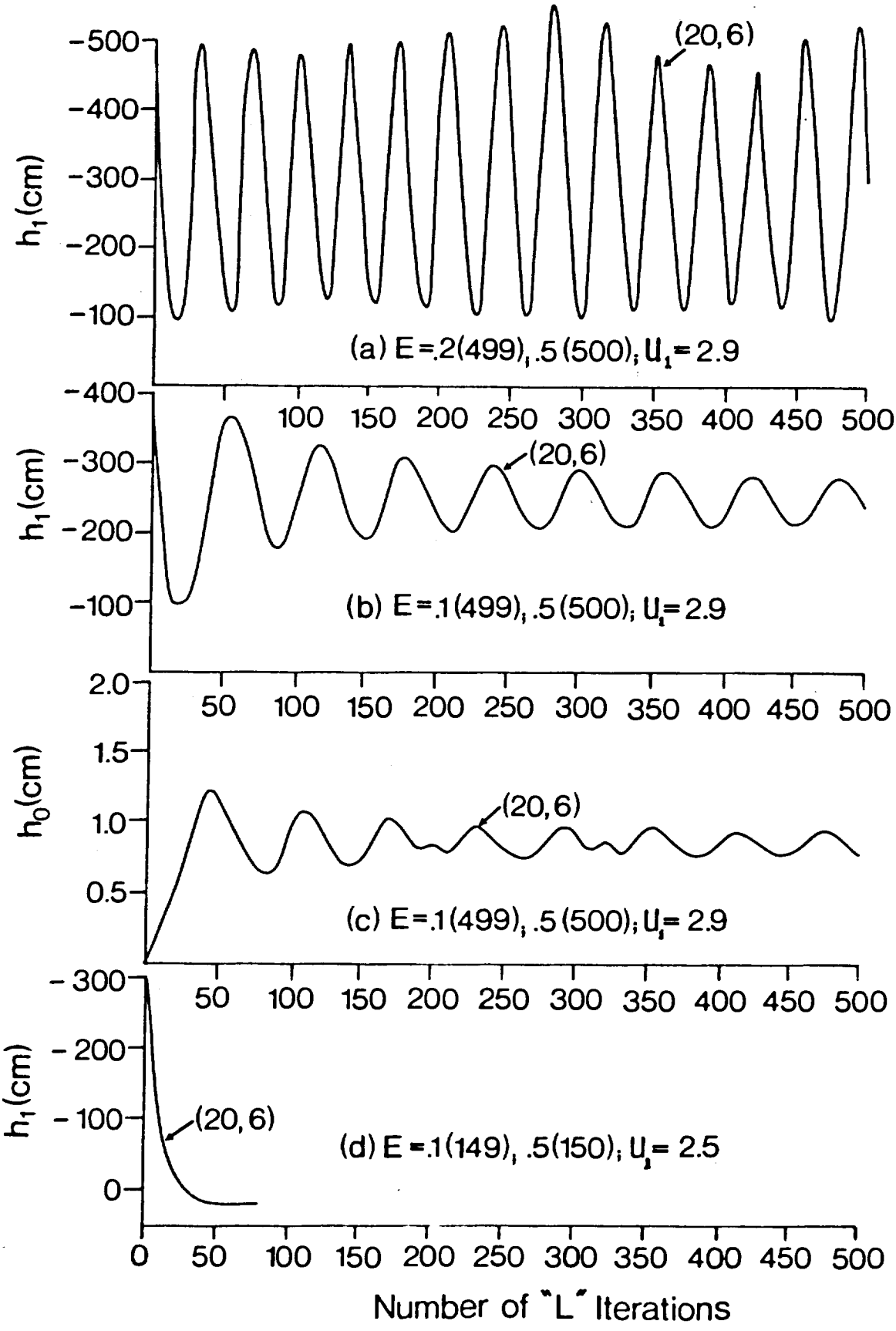

Fig. 27 Stability testing of channel flow problem: interface (h_1) and free-surface (h_0) elevations versus # of 'L' iterations for different E values and U_1 boundary values (e.g., (d) E is .1 for first 149 iterations and .5 for iterations past 150).

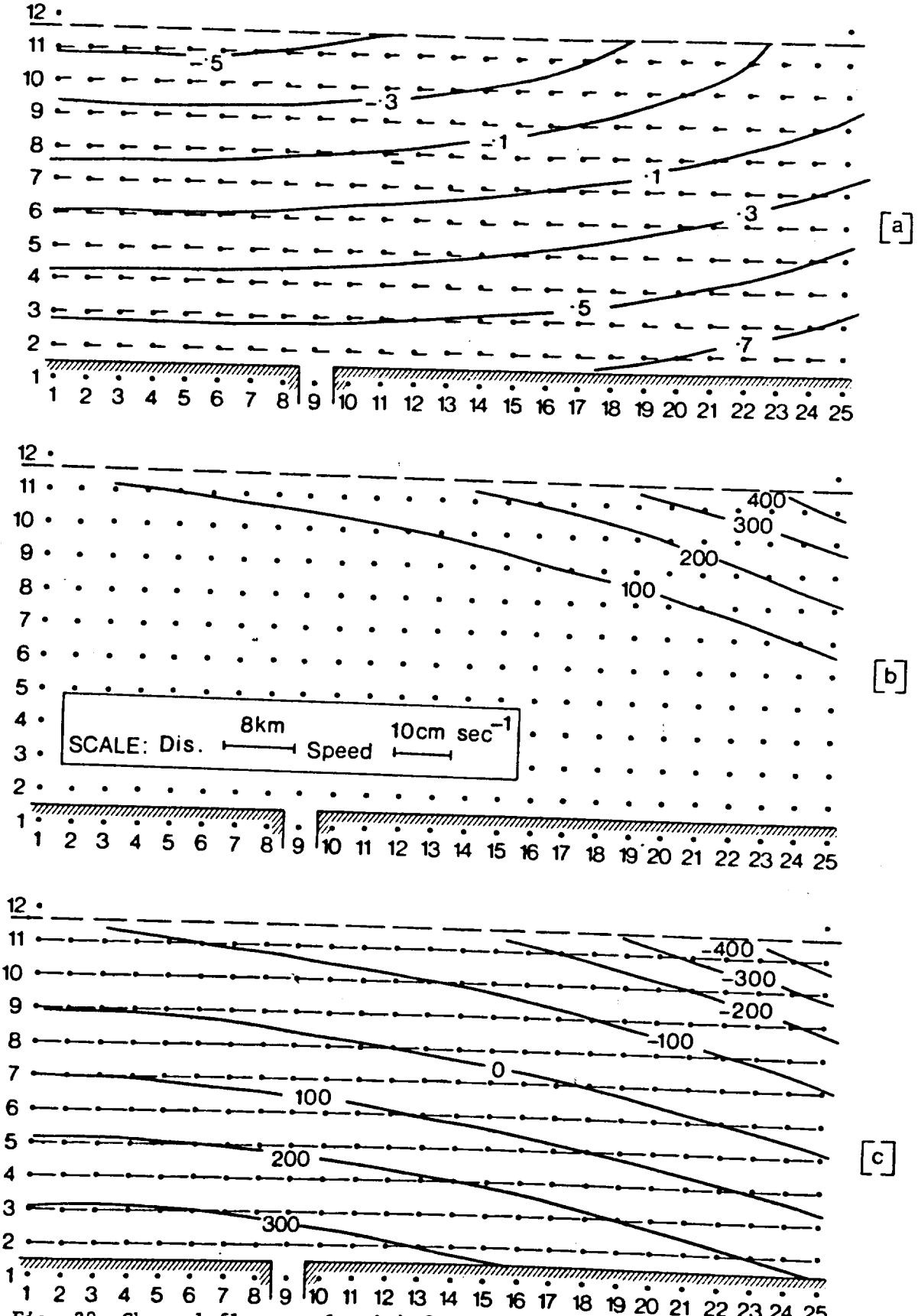

Fig. 28 Channel flow results: a) free-surface elevation (h_o) and upper layer velocity vectors, b) interface thickness (h_{o1}), c) interface elevation (h_1) and lower layer velocity vectors. Velocity vectors drawn from centre of mass conservation cell (dot).

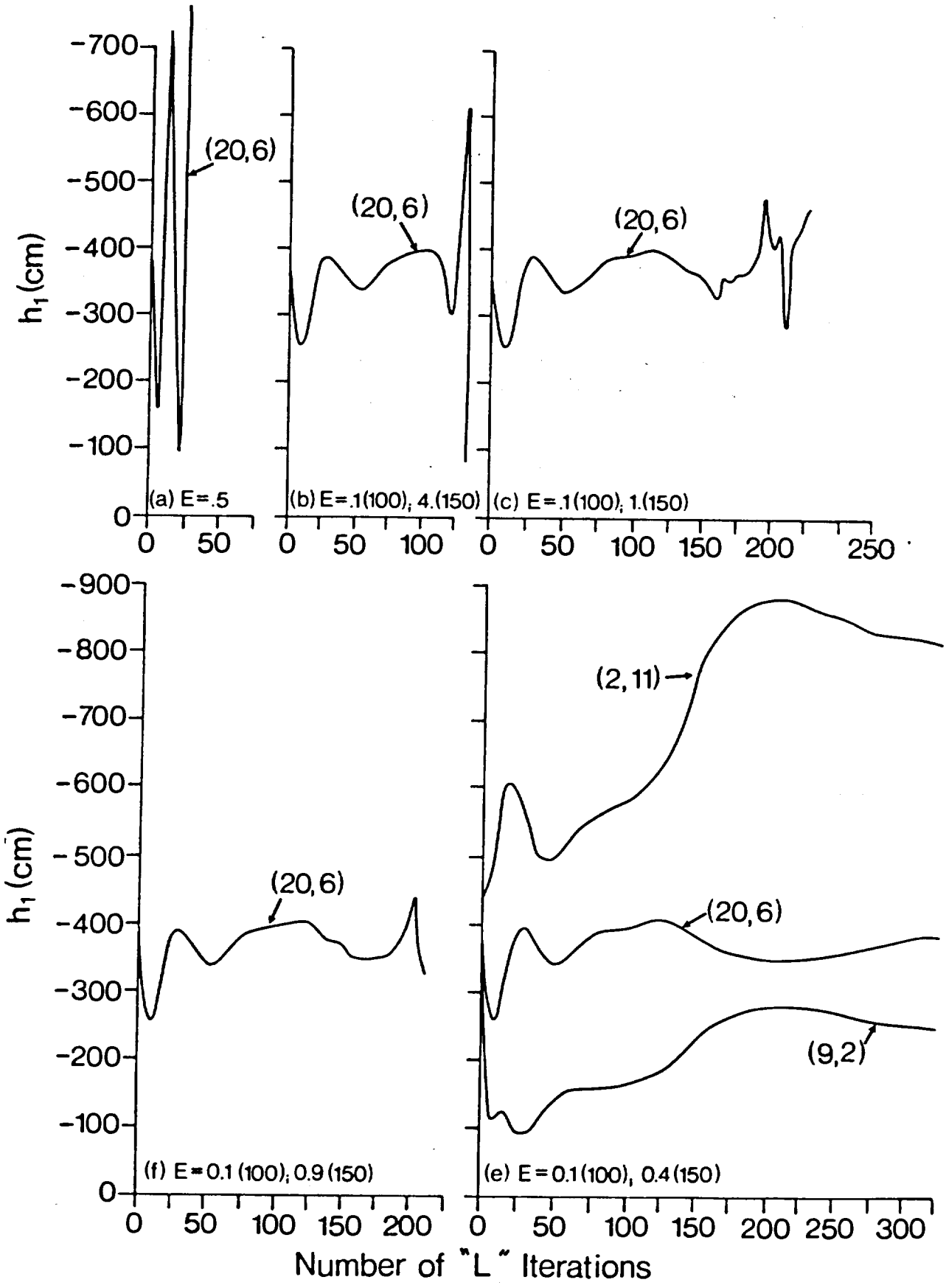

Fig. 29 Stability testing of river flow problem: interface elevations (h_1) versus number of 'L' iterations.

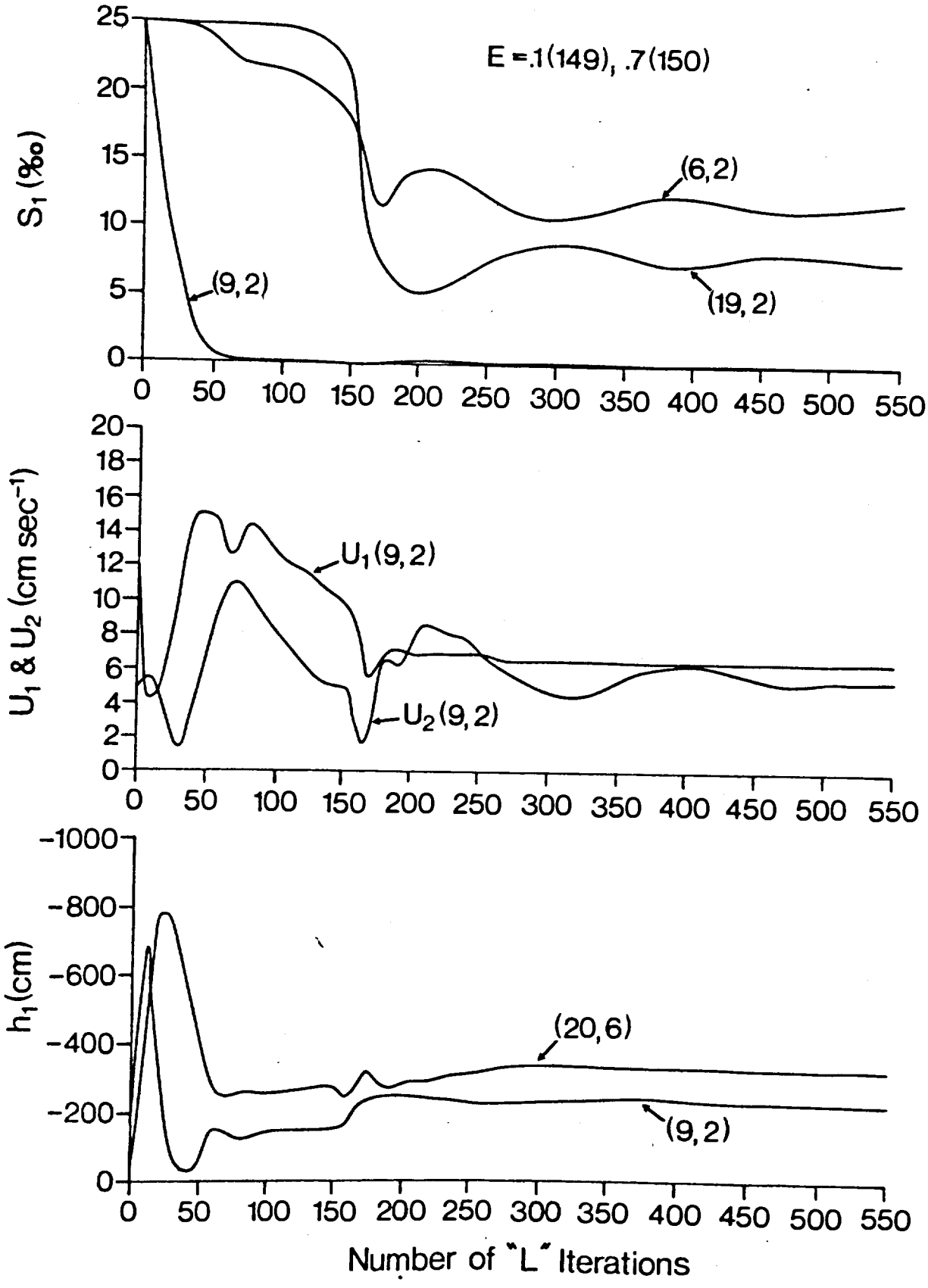

Fig. 30 Convergence testing of river flow problem: surface salinity (S_1), along channel velocity components for upper (U_1) and lower (U_2) layers, interface elevations (h_1) versus # of 'L' iterations.

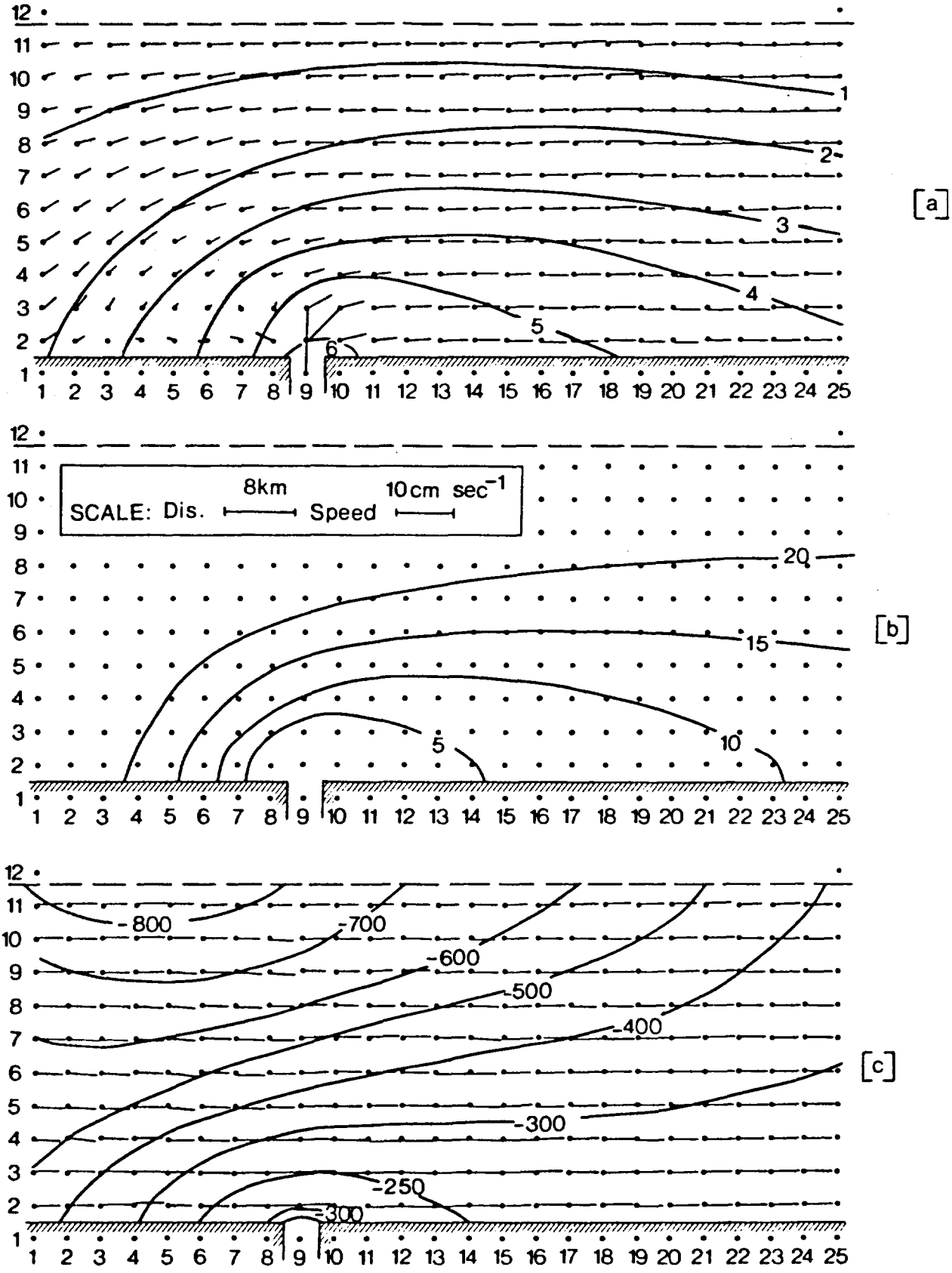

Fig. 31 River flow results without vertical salt diffusion: a) free-surface elevation (h_o) and upper layer velocity vectors, b) surface salinity (S_1), c) interface elevation (h_1) and lower layer velocity vectors.

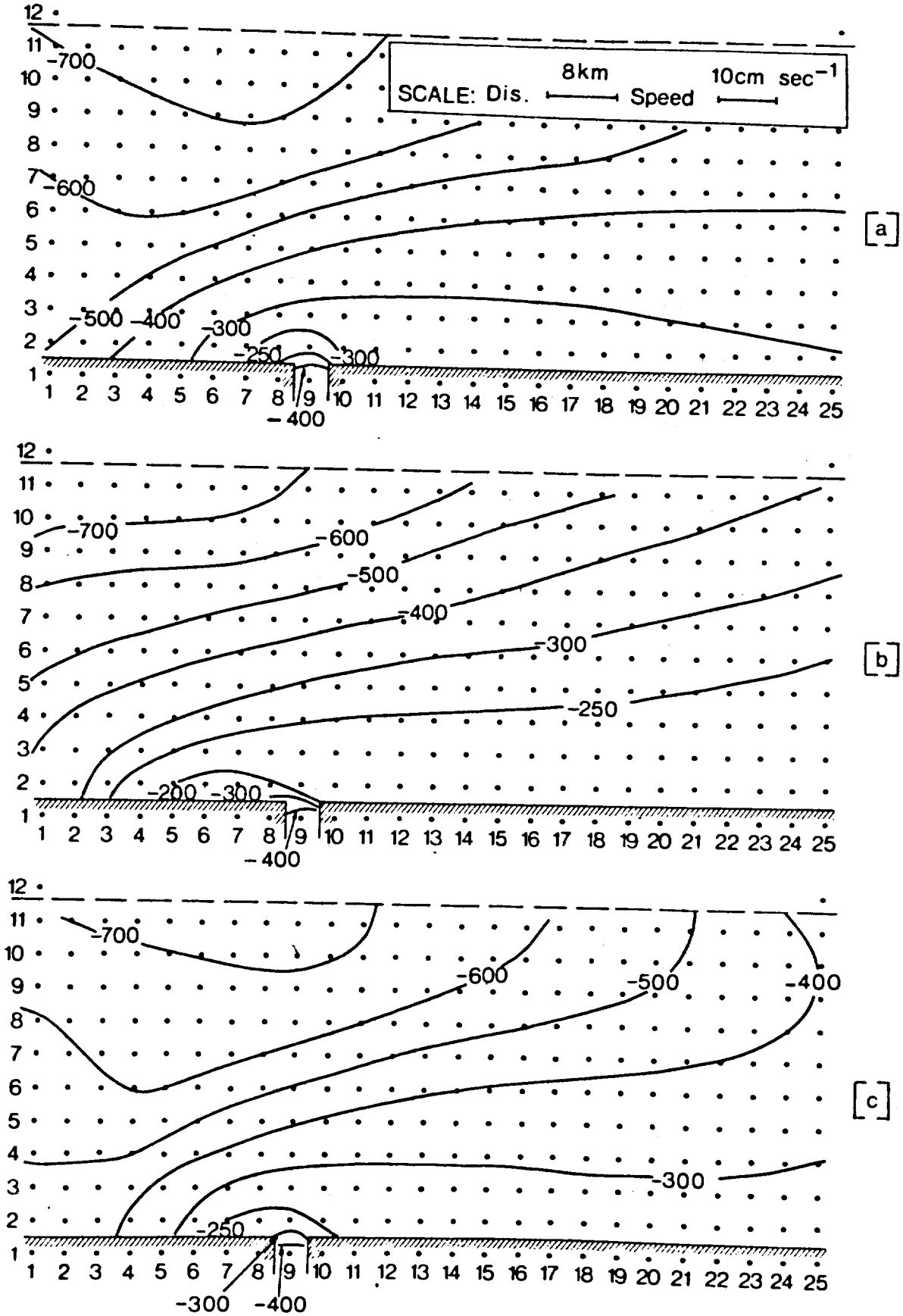

Fig. 32 Testing friction coefficients: a) reducing ice friction in half, b) reducing interface friction in half, c) increasing bottom friction by five times. Contours of interface elevation h_1 are plotted.

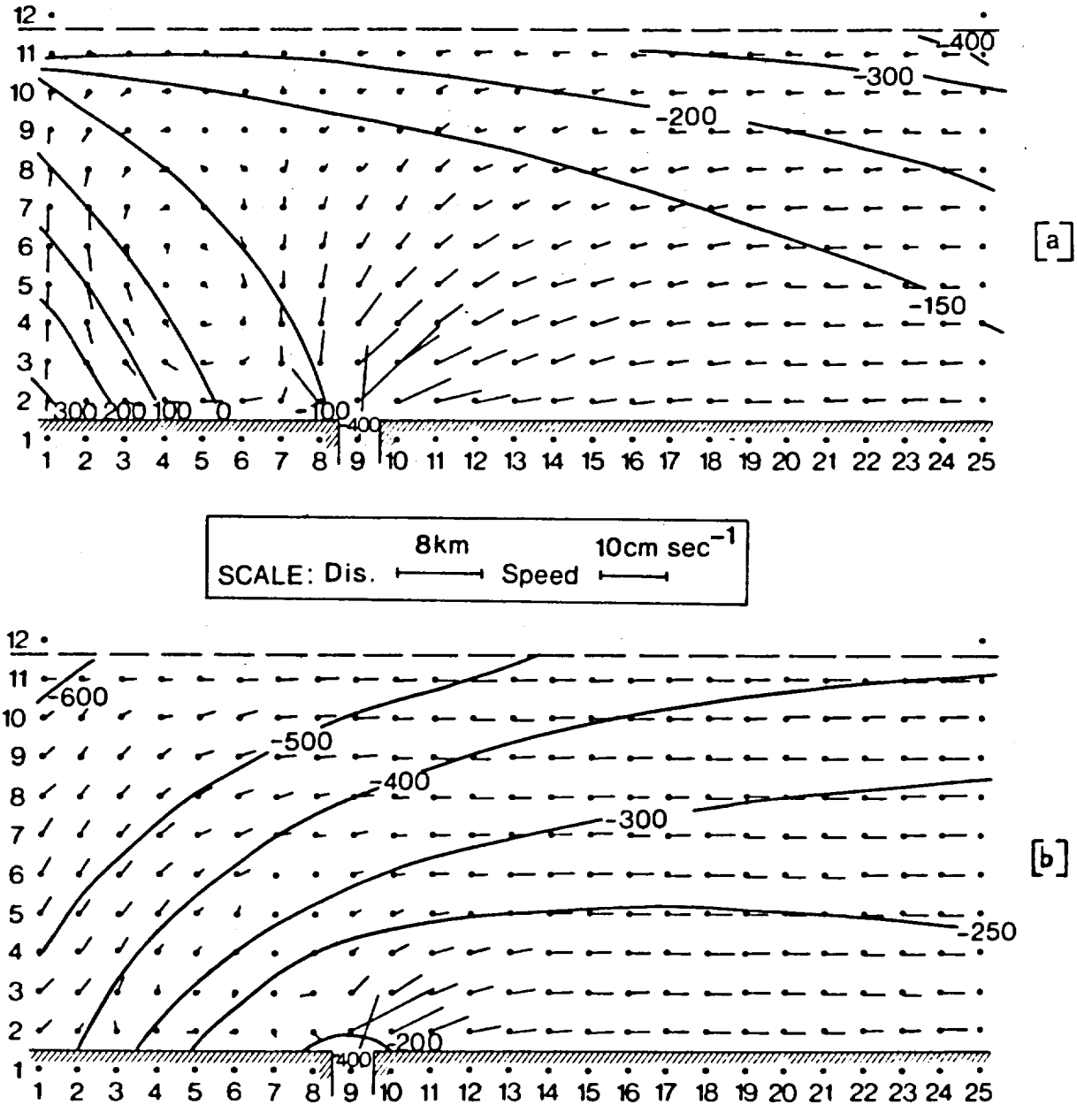

Fig. 33 Testing different background flows: a) zero flow specified at upstream boundary, b) linear flow specified for both U_1 and U_2 at upstream boundary.

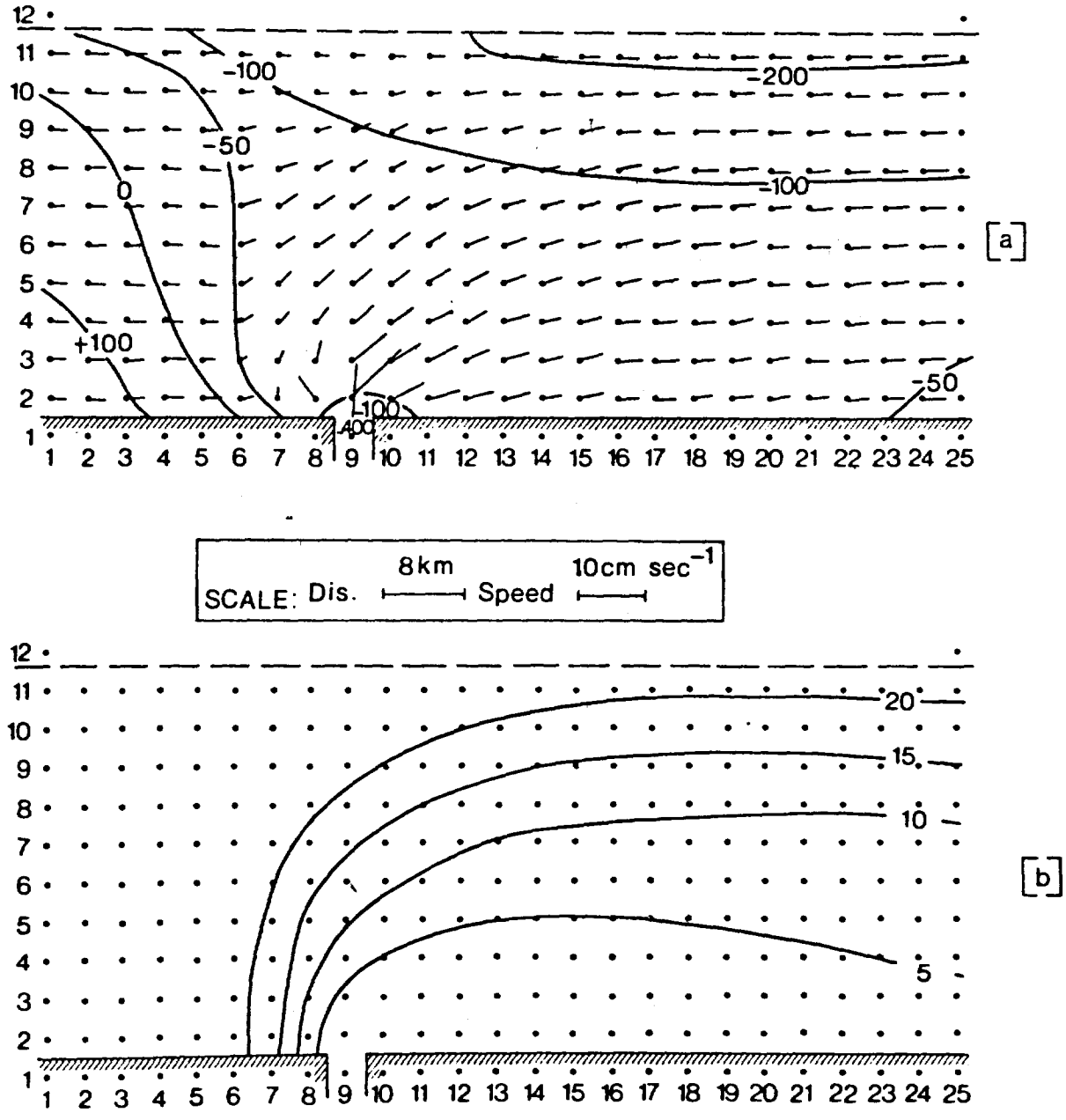

Fig. 34 Testing one half reduction in interface reference level: a) interface elevation (h_1) and upper layer velocity vectors, b) upper layer salinity (S_1).

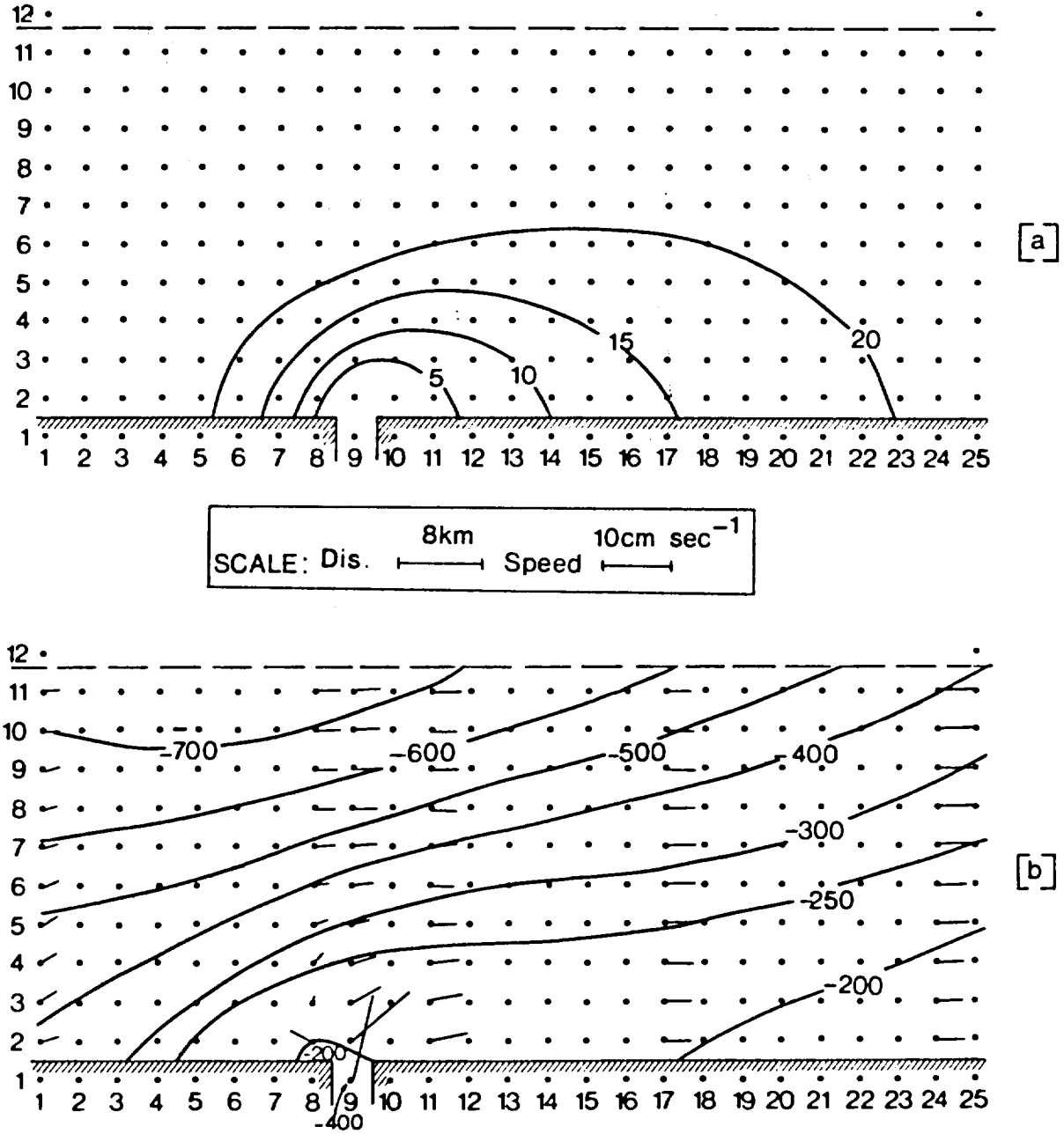

Fig. 35 Adding vertical salt fluxes: a) diffusion - salinity (S_1) contours plotted, b) downward entrainment - interface elevation (h_1) plotted.

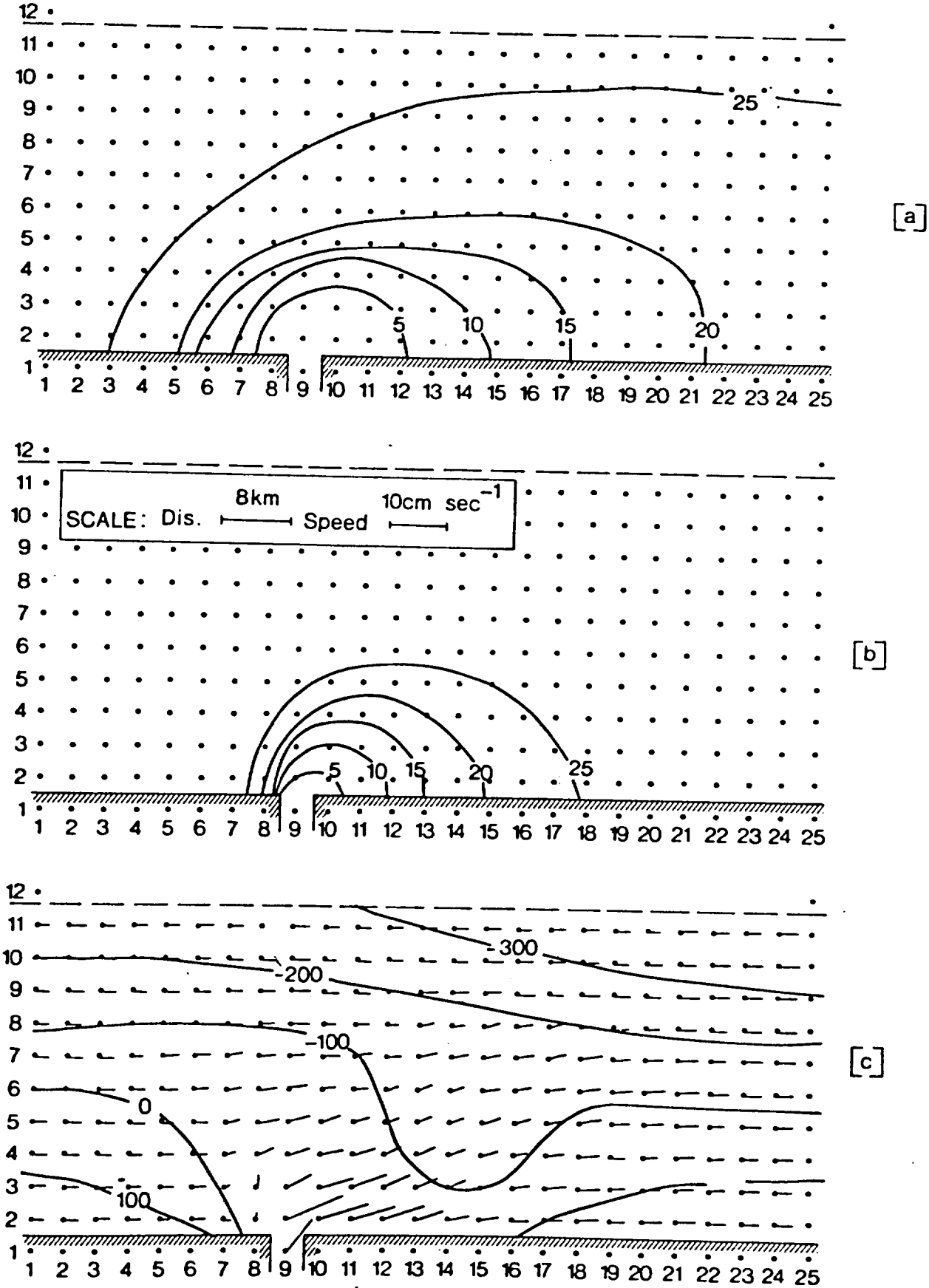

Fig. 36 La Grande plume predictions: a) 1980 discharge of 1600 m^3 sec^{-1} salinity (S_1) contours plotted. (Note: flow field similar to Fig. 31 (a)), b) 1976 discharge of 500 m^3 sec^{-1} - salinity (s_1) contours plotted, c) 1976 discharge - upper layer velocities and interface elevation plotted.